UTPP-80

# Study of the Top Quark Production Mechanism in 1.96-TeV Proton-Antiproton Collisions

**Naoki Kimura**

**February 2009**

**Study of the Top Quark Production Mechanism in 1.96-TeV Proton-Antiproton Collisions**

**Naoki Kimura**
**(Doctoral Program in Physics)**

**Submitted to the Graduate School of Pure and Applied Sciences in Partial FulFillment of the Requirements for the Degree of Doctor of Philosophy in Science**

**at the**
**University of Tsukuba**

# Abstract

We study the production of top-antitop quark pairs in proton-antiproton collisions at a center-of-mass energy of 1.96 TeV. We identify and reconstruct the signal using events which include two high-momentum leptons. First, we measure the production cross section of the top quark pairs. Second, we measure the relative fraction of the subprocess where the initial states are gluon-gluon pairs (gluon fusion) or quark-antiquark pairs ($q\bar{q}$ annihilation), by utilizing the correlated spin states of top and antitop quark. The analysis is based on 2.0 fb$^{-1}$ of data collected with the Collider Detector at Fermilab (CDF) at the Fermilab Tevatron between March 2002 and May 2007. We observe 145 $t\bar{t}$ candidate events with an expected background of 49.5 events. We measure the production cross section of the top quark pairs to be $\sigma(p\bar{p} \to t\bar{t}X) = 6.8 \pm 1.1$ pb, and find the fraction of the gluon fusion subprocess to be $\mathcal{F}_{gg} = 0.53\ ^{+0.36}_{-0.38}$. They are in agreement with the next-to-leading order calculations of $\sigma(p\bar{p} \to t\bar{t}X) = 6.7\ ^{+0.7}_{-0.9}$ pb and $\mathcal{F}_{gg} = 0.15 \pm 0.05$.

# Acknowledgments

This dissertation could not have been finished without the dedication and support of many people. First of all, I would like to express my sincere gratitude to my supervisor, Professor Fumihiko Ukegawa, for great suggestion and providing me this precious study opportunity as a Ph.D student in his laboratory. My deepest appreciation goes to Professor Shinhong Kim. He gave me a chance to go to Fermilab and also gave me a constructive advice when I was in difficulties on my studies. I also own a great debt to Yuji Takeuchi, for his support and advice.

I would like to thank Kazuhiko Hara, Takasumi Maruyama, Tomonobu Tomura, Koji Sato, Kohei Yorita, Masato Aoki, Hideki Miyake, Masakazu Kurata, Kenichi Hatakeyama and Junji Naganoma. Over the years, they have helped me keep my motivation, while also encouraging me to build up my experience in experimental particle physics. I would also like to thank academic colleague at Fermilab. Tatsuya Masubuchi, Taichi Kubo, Ai Nagano, Takayuki Wakisaka, Koji Nakamura, and so many others have helped make this an interesting, challenging, and always entertaining place to get a Ph.D.

At Fermilab, I had the opportunity to work with a group of really great people. My deepest appreciation goes to CDF physics group conveners, Robin Erbacher, Anyes Taffard, Kirsten Tollefson, Kevin Lannon, Charles Plager, Andrew Ivanov, Florencia Canelli, Veronica Sorin, whose comments and suggestions were of inestimable value to my study.

I thank Monnica Tecchio, Alexei Varganov, Andrew Beretvas, Tuula Maki, Victoria Giakoumopoulou and Chang-Seong Moon of the top dilepton group. I learned important lessons about what it means to be a good scientist.

I am also very grateful to all of the Fermilab staff, CDF collaborators, and all the people who were involved in building and maintaining the Tevatron and the CDF detector. Without your contribution this work would have been impossible.

Finally, my deep gratitude goes to my family. I can't thank you enough.

# Contents

# List of Figures

# List of Tables

# Chapter 1

# Introduction

One of the basic questions of the human beings is what the physical matter is made of. To answer this question, particle physics has been trying to determine the fundamental constituents of the universe and the nature of their interactions.

In the last sixty years, much progress has been made in discovering these constituent particles and the rules of their interactions. All observed phenomenaare described by what has come to be called the Standard Model of particle physics. Since the observation of the $W^{\pm}$ and $Z^{0}$ bosons predicted by the unified electroweak theory, experimental particle physics has focused on searches for the remaining particle predicted by the Standard Model and measurements of their interactions.

With the observation of the top quark in 1995 [1, 2] and the tau neutrino in 2000 [3], nearly the full catalog of Standard Model particles has been directly observed, with only the Higgs boson evading detection. Despite the great success of the Standard Model in describing the particles and interactions observed up to now, however there is a good theoretical motivation to believe that a new framework must come into play at approximately the TeV energy scale. Increasingly stringent measurements of the properties of particles and their interactions at the highest available energies, coupled with direct searches for phenomena not described by the Standard Model, are the main project of modern experimental particle physics. A significant part of the project is the elucidation of the properties of the top quark.

This thesis reports measurements of the production cross section of the top quark pairs and identification of the initial state of the subprocess, whether it is a gluon-gluon pair or a $q\bar{q}$ pair. A measurement of the production cross section is the most important parameter for all analysis using this process, and also serves as a good test of the Standard Model. A measurement of the gluon fusion fraction will give a knowledge of the gluon content of the proton at large values of $x$, as well as a test of the perturbative QCD calculations. As will be described later, the two subprocesses have different $t\bar{t}$ spin correlations, and they can be differentiated if we can access the $t\bar{t}$ spin information. Because the top quark decays before hadronization because of its short lifetime, the top quark spin information is preserved and transferred to its decay products. We utilize the fact and use the angular correlations among decay products to infer the initial state of the subprocess. This is the first measurements of the gluon fusion fraction using the $t\bar{t}$ spin correlation.

## 1.1 The Standard Model

The Standard Model of particle physics describes all known fundamental particles (quarks and leptons) and their interactions in the strong, electromagnetic and weak nuclear forces. The model itself is a combination of the theory of quantum chromodynamics (QCD) [4, 5] and the Glashow-Salam-Weinberg (GSW) theory of electroweak interactions [6, 7, 8]. The former describes the strong force and is represented by the $SU(3)_C$ gauge group, while the latter describes the weak and electromagnetic forces and is represented by the $SU(2)_L \times U(1)_Y$ gauge group. The Standard Model is locally invariant under transformations of the group,

$$G = SU(3)_C \times SU(2)_L \times U(1)_Y. \tag{1.1}$$

It is known that there exist three generations of fundamental fermions. Each generation consists of a pair of leptons,

$$\begin{pmatrix} e \\ \nu_e \end{pmatrix}, \begin{pmatrix} \mu \\ \nu_\mu \end{pmatrix}, \begin{pmatrix} \tau \\ \nu_\tau \end{pmatrix}, \tag{1.2}$$

whose interactions are mediated by the electroweak forces, and a pair of quarks,

$$\begin{pmatrix} u \\ d \end{pmatrix}, \begin{pmatrix} c \\ s \end{pmatrix}, \begin{pmatrix} t \\ b \end{pmatrix}, \tag{1.3}$$

whose interactions are mediated by both the electroweak and strong (QCD) forces.

The existence of three generations of quarks and leptons gives a natural explanation of CP violation. However, any theory cannot succeed in giving a natural explanation of the three generations. The vast majority of stable matter we observe is made up of particles entirely in the first generation. Gauge bosons mediate the forces described by the Standard Model: the photon ($\gamma$) for the electromagnetic force, the $W^\pm$ and $Z^0$ bosons for the weak force, and the gluon ($g$) for the strong force.

The Standard Model has been successful in describing interactions of the particles described above, all of which have been discovered experimentally. In addition, many of the predicted properties of these particles have been confirmed, some to a high degree of precision. However, in order for the symmetry described in Eq.(1.1) to be exact, the fermions and the $W$ and $Z$ bosons would have to be massless. In order for the Standard Model to be compatible with the large masses of the $W$ and $Z$ bosons and thus the large division between the effective weak coupling constant (the Fermi constant) and the electromagnetic coupling constant (the fine structure constant), spontaneous symmetry breaking must occur. This symmetry breaking would additionally be responsible for the mass hierarchy observed in the fermions. This Electroweak Symmetry Breaking (EWSB) is accomplished by the introduction of a scalar field known as the Higgs field [9]. The existence of a massive scalar particle, the Higgs boson, would be associated with the Higgs field.

The existence of the Higgs boson has yet to be confirmed experimentally, and remains one of the most important tasks for the field of high energy physics. Direct searches for the Standard Model Higgs boson at the CERN Large Electron Positron (LEP) collider have set a lower bound on its mass of $M_H > 114.4$ GeV/c$^2$ at the 95% confidence level [10]. In addition, indirect bounds on the mass of the Higgs boson can be set from precision measurements of the top quark and $W$ boson masses, as these quantities are sensitive to $\ln M_H$ through radiative corrections. Using measurements of the top quark mass and the precision electroweak measuments made at LEP [11], the constraints on the Standard Model Higgs bosons are

$$M_H = 76^{+33}_{-24} \text{ GeV}/c^2, \tag{1.4}$$
$$M_H < 144 \text{ GeV}/c^2 \text{ at } 95\% \text{ C.L..} \tag{1.5}$$

## 1.2 The Top Quark

Following the discovery of the bottom ($b$) quark in 1977, the existence of its doublet partner, the top ($t$) quark, could be inferred for several reasons. For one, the renormalizability of the Standard Model requires that the sum of electric charges of all left-handed fermions must equal zero. This condition

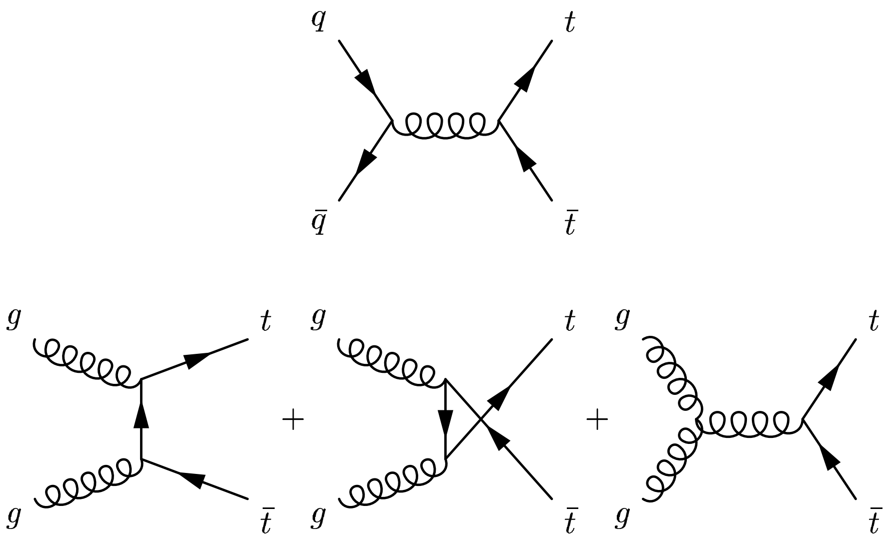


Figure 1.1: Top: Leading-order production diagram for $q\bar{q} \to t\bar{t}$. Bottom: Leading-order production diagrams for $gg \to t\bar{t}$.

is only satisfied with the existence of a sixth quark with an electric charge of $+2/3$. In addition, the precise measurements involving the isospin of the $b$-quark can be made at $e^+e^-$ colliders, which can be used to exclude the possibility of the $b$-quark being a member of a singlet [12]. The evidence of the top quark production was reported by the CDF collaboration in 1994. In the next year the discovery of the top quark was established with more statistics of the data by both the CDF and DØ collaborations [1, 2]. By the end of the 1992-1996 collider run (Run I), combined datasets from both experiments of $\sim$ 100 pb$^{-1}$ provided a measurement of the top quark mass of $M_t = 178.0 \pm 4.3$ GeV/$c^2$ [13].

## 1.3 Top Quark Production

Currently, only the Fermilab Tevatron has an energy sufficient to produce particles as massive as the top quark. At hadron colliders the top quarks are produced mainly in pairs via the strong interaction. The leading order Feynman diagrams are shown in Figure 1.1. In parton-level subprocesses the top pair production occurs via the quark-antiquark annihilation and gluon fusion. In Section 1.6, we discuss the detail of the top quark production mechanism.

The theoretical prediction of the $t\bar{t}$ production cross section at next-to-

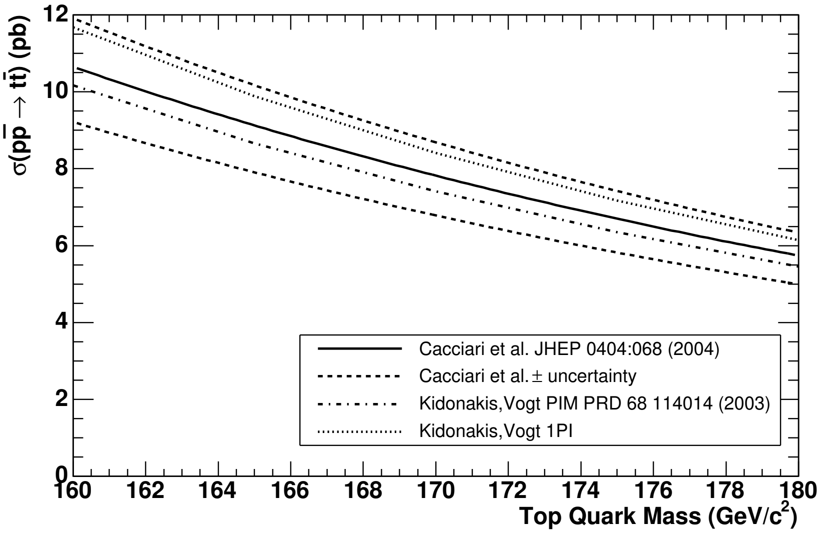


Figure 1.2: NLO calculations of $\sigma(p\bar{p} \to t\bar{t}X)$ [17] for $p\bar{p}$ collisions at $\sqrt{s}$=1.96 TeV as a function of the top quark mass.

leading order (NLO) is $\sigma^{NLO}(p\bar{p} \to t\bar{t}X) = 6.7^{+0.7}_{-0.9}$ pb at $M_t = 175$ GeV/$c^2$ [17]. Figure 1.2 shows the NLO calculation of $\sigma(p\bar{p} \to t\bar{t}X)$ for $p\bar{p}$ collisions at $\sqrt{s} = 1.96$ TeV as a function of the top quark mass.

We measure the $t\bar{t}$ production cross section to test the Standard Model prediction. At the same time, it give a basis for other analyses.

## 1.4 Top Quark Decay

The top quark is expected to decay via the channel $t \to Wb$ nearly 100 % of the time. Other decay channels are permitted in the Standard Model, but are heavily suppressed by factors of $|V_{ts}|^2/|V_{tb}|^2 \approx 10^{-3}$ and $|V_{td}|^2/|V_{tb}|^2 \approx 5\times10^{-4}$, where $V_{ij}$ is the element of the Cabibbo-Kobayashi-Maskawa (CKM) weak-mixing matrix [19]. The large mass of the top quark results in a very rapid decay with a mean lifetime of $\tau_t \sim 10^{-24}$ s. As this is shorter than the time scale required for quarks to form bound states (or "hadronize"), the top quark essentially decays as a "free" quark. The $b$-quark resulting from the decay will then proceed to hadronize and manifest itself in the detector as a jet, or a collimated stream of hadrons. The $W$ boson will decay rapidly into either a pair of quarks or a pair of charged lepton and a neutrino. Thus,

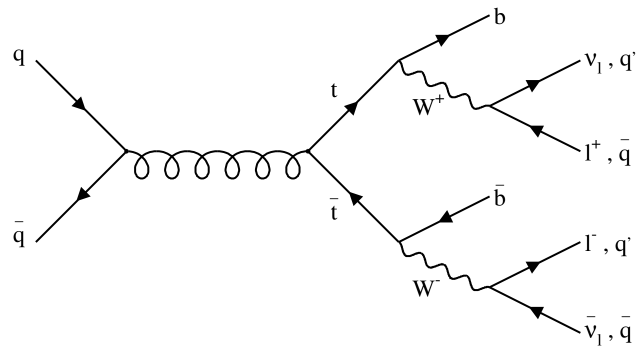


Figure 1.3: Tree level $q\bar{q} \rightarrow t\bar{t}$ production and decay.

for the case of a $t\bar{t}$ pair production and decay, there are six particles in the final state: two $b$-quarks and two decay products from each of the $W$ bosons. Figure 1.3 shows the tree level diagram of $t\bar{t}$ production and decay in the subprocess $q\bar{q} \rightarrow t\bar{t}$

It is the decay mode of the $W$ bosons that defines the decay channels of the $t\bar{t}$ system used in its experimental study. These decay channels are classified as:

**The all-hadronic channel,** where both $W$ bosons decay to quark-antiquark pairs, resulting in a final state having an experimental signature of six jets. This decay mode carries the largest branching ratio, of 46 %, but suffers from the largest amount of irreducible QCD background.

**The lepton+jets channel,** where one $W$ decays to a lepton-neutrino pair and the other to quarks, resulting in an experimental signature of a high momentum lepton, four jets, and a missing transverse energy associated with the neutrino. Due to the difficulty of identifying $\tau$ leptons at a hadron collider, only leptonic states with an electron or muon in the final state are considered. This channel carries a branching ratio of 30 %.

**The dilepton channel,** where both $W$ bosons decay to leptons, resulting in an experimental signature of two high momentum leptons, two jets, and large missing transverse energy associated with two neutrinos. As with the lepton+jets channel, only leptonic states with an electron or muon in the final state are considered. This channel carries a branching ratio of 4 %. The remaining 20 % of $t\bar{t}$ decays involve the production of a lepton that does not decay to an e or $\mu$. While measurements in this so-called "$\tau$ + $X$" channel are possible, they do not afford nearly the same precision that any of the

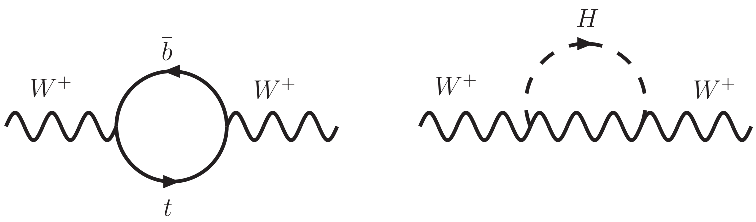


Figure 1.4: Loop diagrams generating corrections to the theoretical $W$ boson mass. On the left is a fermion loop with the top and $b$ quarks. On the right is a Higgs boson loop.

other three channels does.

## 1.5 Top Quark Mass

The top quark mass is a fundamental parameter in the Standard Model. Due to its large value, it has a critical influence on the Standard Model calculations than the other quarks. It contributes to higher order (radiative) corrections to electroweak processes, as illustrated in Figure 1.4. It also helps to constrain the mass of Higgs boson via the radiative correction to the mass of the $W$ boson. Figure 1.5 shows constraints on the Higgs boson mass using the current best measurements of the $W$ boson and the top quark masses, and a global fit of the Higgs boson mass to several electroweak parameters. As indicated in Fig. 1.5, the most likely value of the Higgs boson mass is ruled out by the direct searches at LEP. A failure of the Standard Model to properly describe these results may indicate new physics yet to be discovered.

## 1.6 Top Quark Production Mechanism and Spin Correlations

The proton is a collection of quarks, antiquarks, and gluons (collectively called partons), each carrying some fraction $x$ of the proton's four momentum. The probability densities of finding a parton with a given momentum fraction in a proton are called *parton distribution functions (PDF's).* The total production cross section $p\bar{p} \rightarrow t\bar{t}X$ is a convolution of the PDFs for the incoming protons and antiprotons and the cross section for the partonic processes:

$$\sigma(p\bar{p} \to t\bar{t}X) = \sum_{a,b} \int dx_a dx_b f_a^p(x_a, \mu^2) f_b^{\bar{p}}(x_b, \mu^2) \hat{\sigma}(ab \to t\bar{t}; \hat{s}, \mu^2, m_t), \quad (1.6)$$

where the summation indices $a$ and $b$ run over light quarks and gluons contained in the initial proton and antiproton and carrying momentum fractions of $x_a$ and $x_b$, respectively.

At Tevatron the total energy in the center-of-momentum frame of $p\bar{p}$ collisions is $\sqrt{s} = 1.96$ TeV. In order to produce a $t\bar{t}$ pair, the square of the total energy of the partonic subprocess $\hat{s} = x_a x_b s$ has to be larger than $4m_t^2$. Hence a typical value of $x$ for $t\bar{t}$ production at Tevatron is

$$x \simeq \frac{2m_t}{\sqrt{s}} \simeq 0.18. \quad (1.7)$$

Figure 1.6 shows the parton distribution functions of the proton for different parton species. One can see. That for $x \simeq 0.18$ the up quark distribution function is larger than that of the gluon, and the down quark distribution function is comparable to gluon. In $p\bar{p}$ collisions at $\sqrt{s} = 1.96$ TeV, it is predicted that $t\bar{t}$ pairs are produced dominantly through $q\bar{q}$ annihilation, while about 15% of $t\bar{t}$ pairs are produced via the gluon fusion subprocess [14].

Because of uncertainties in the large-$x$ gluon luminosity, the prediction of this fraction has a large ambiguity and will change by up to a factor of 2 (from 10% to 20%). Hence, a measurement of the relative fractions of the two subprocesses will give a knowledge of the gluon content of the proton at large values of $x$, as well as serve as a test of the perturbative QCD calculations.

The $t\bar{t}$ pair produced via the gluon fusion has a different spin state from that produced via $q\bar{q}$ annihilation. This difference results in a difference in azimuthal correlations of charged leptons when $t\bar{t}$ pairs are identified in the dilepton channel [15]. When $t\bar{t}$ pairs are produced near kinematic threshold, the pairs produced via the gluon fusion and $q\bar{q}$ annihilation subprocesses are in the following total angular momentum states, respectively [16]:

$$\begin{aligned} gg &: \quad J = 0, J_z = 0, \\ q\bar{q} &: \quad J = 1, J_z = \pm 1, \end{aligned}$$

where $z$ denotes the initial parton direction (i.e. nearly the beam direction).

Therefore, in the case of gluon fusion, the top quark and the anti-top quark have the opposite spin on any axis of quantization, while they have the aligned spin on the beam axis in the case of $q\bar{q}$ annihilation. Figure 1.7 shows the spin configurations of the gluon fusion and $q\bar{q}$ annihilation at a threshold production.

And because of the $V-A$ structure of the top quark decays, the flight direction of the lepton is strongly correlated with the spin direction of the top quark.

Thus we utilize the difference in azimuthal correlation of charged leptons in the $t\bar{t}$ dilepton channel to distinguish $t\bar{t}$ pair produced via the gluon fusion from $q\bar{q}$ annihilation.

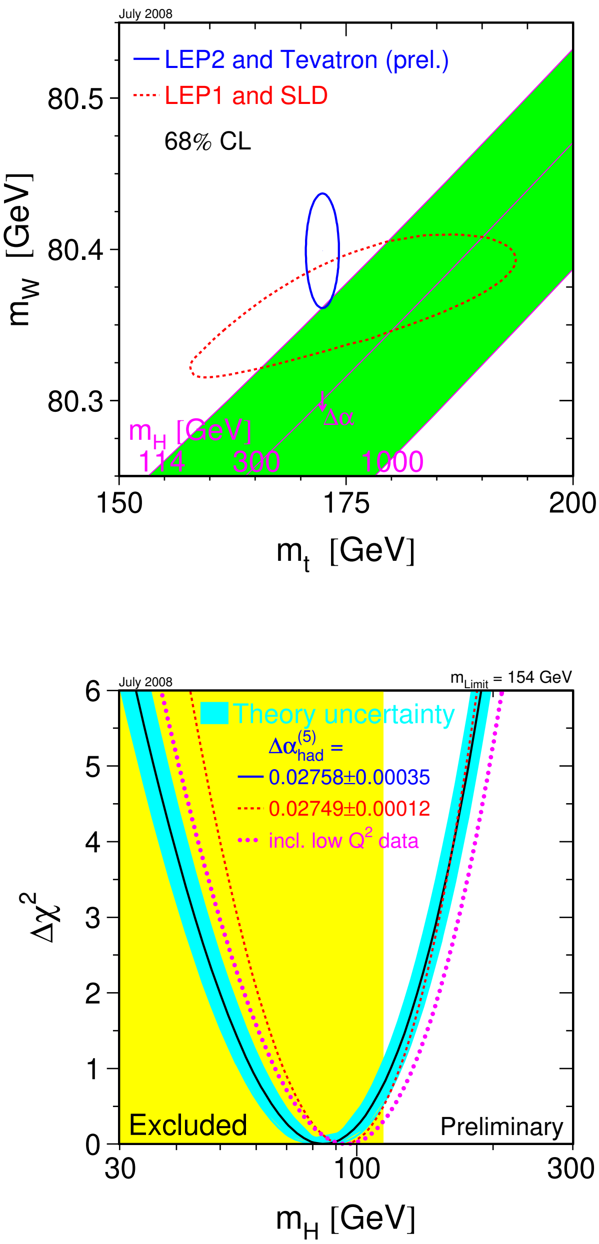


Figure 1.5: Electroweak constraints on the Higgs boson mass using the current best measurements of $W$ boson and top quark mass (top). Global fit of Higgs boson mass to several electroweak parameters (bottom).

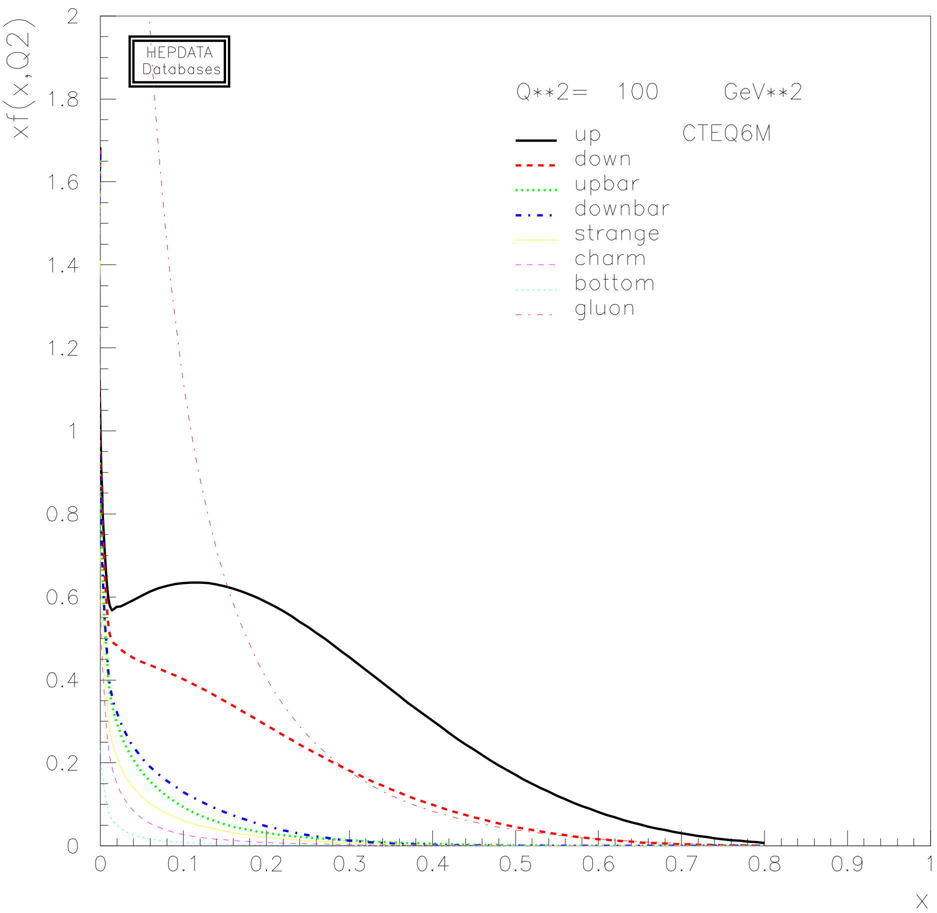


Figure 1.6: Parton distribution function in the proton for different parton species.

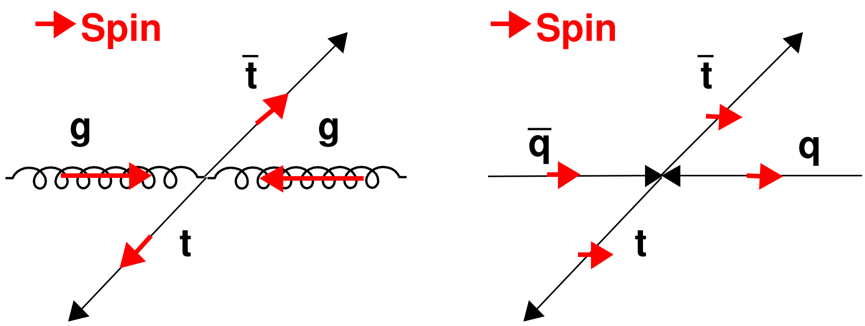


Figure 1.7: The spin configurations of the gluon fusion (left) and $q\bar{q}$ annihilation (right) subprocesses.

# Chapter 2

# Experimental Apparatus

The experimental apparatus consists of the accelerators and the CDF detector. They have been continuously upgraded since the first Tevatron collision in October 1985.

## 2.1 Fermilab's Accelerator Chain

The accelerator complex is described in detail in [20] and briefly summarized here. It consists of the pre-accelerator, the linear accelerators (linac) [21], the booster [22], the Main Injector [23], the antiproton source [24], the Recycler [25], and the Tevatron [26]. An overview of the accelerator complex is shown in Figure 2.1.

### 2.1.1 Pre-accelerator

The pre-accelerator produces the beam of 750 keV $H^-$ ions, which consists of a negative hydrogen ion source [27], a Cockcroft-Walton generator [28], an electrostatic accelerating column, and a transport line. Hydrogen gas is passed through a magnetron to produce $H^-$ ions at the dome with a potential of -750 kV. The potential is created by the 5-stage diode voltage multiplier, which converts 75 kV AC to the $-750$ kV DC. The extracted $H^-$ ions are accelerated to 750 keV by passing through the accelerating column. The amount of $H^-$ beam allowed to pass from the source to the Linac is controlled by the chopper. The transport line includes the focusing magnets and a single gap RF cavity which bunches the beam at the RF frequency of the Linac. A schematic view of the pre-accelerator is shown in Figure 2.2.

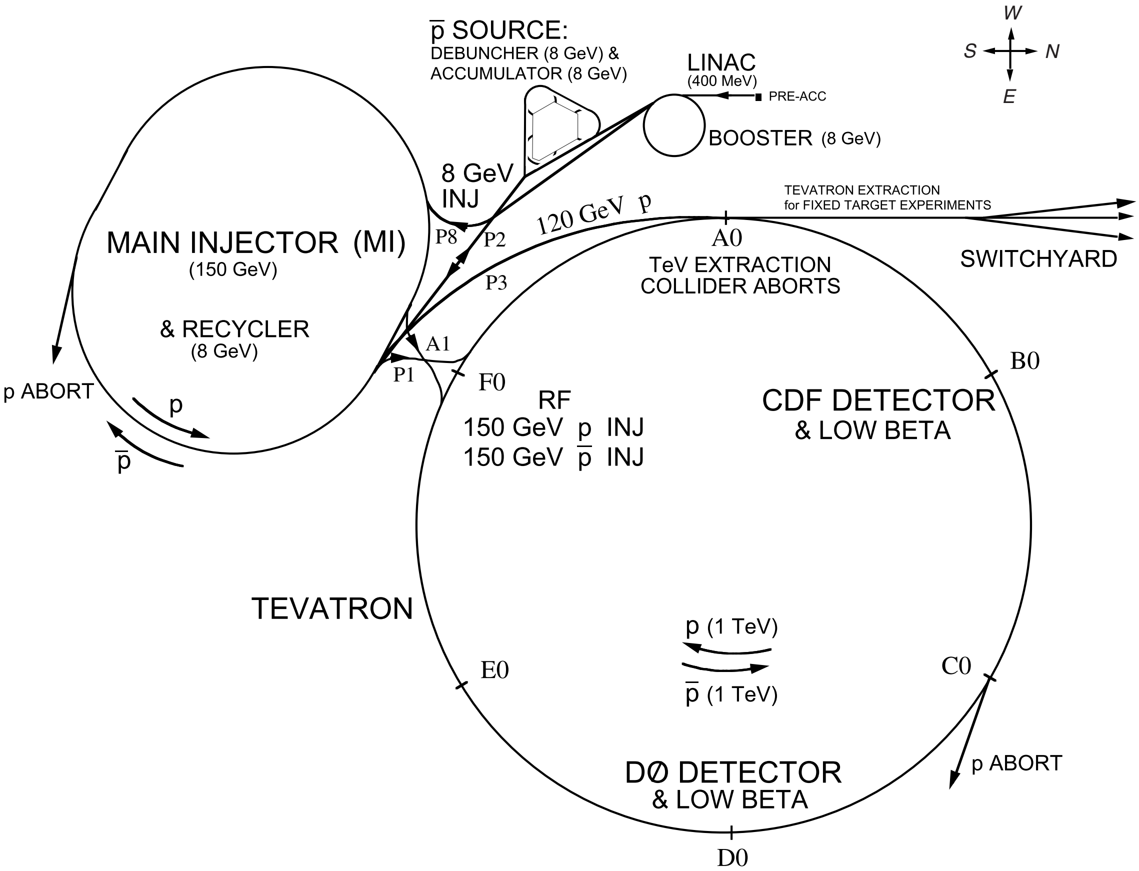


Figure 2.1: Overview of Fermilab accelerator complex. (All the accelerator figures and contents are courtesy of Fermilab Accelerator Division)

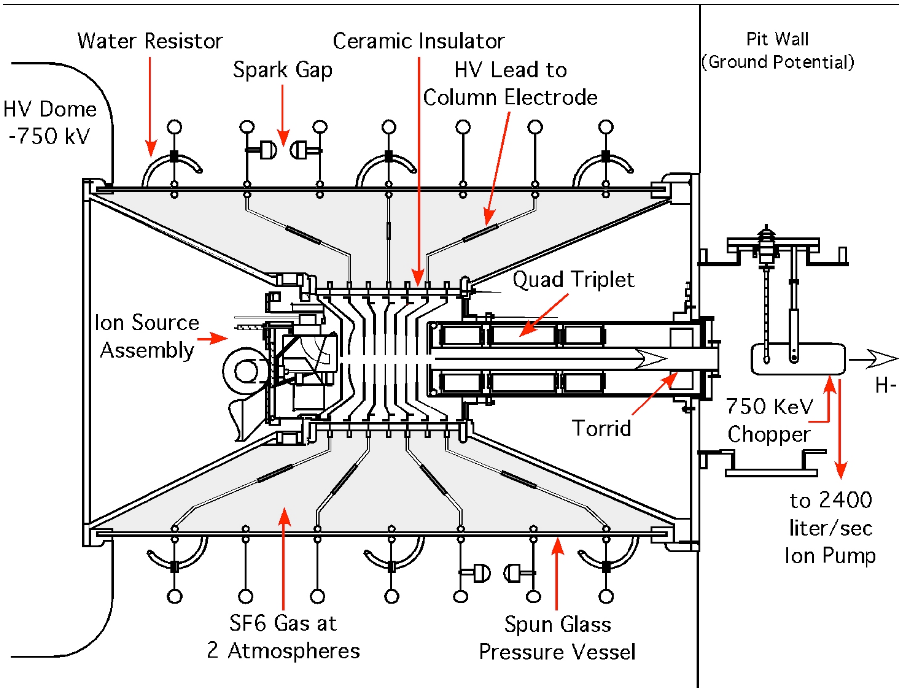


Figure 2.2: Ion source and the electrostatic accelerating column.

### 2.1.2 Linac

The Linac is a two-stage linear accelerator that produces a pulsed beam of 400 MeV $H^-$ ions for charge-exchange injection [29] into the Booster. The first stage is an Alvarez drift-tube accelerator [30], which accelerates the ions to 116 MeV. The second is a side-coupled linac, which accelerates the $H^-$ beam to 400 MeV. The accelerating gradient for each side-coupled cavity is about three times that of the drift-tube Linac. The $H^-$ beam is focused by the quadrupole magnets at both Linacs.

### 2.1.3 Booster

The booster [22] is an 8 GeV proton synchrotron used as an injector to the Main Ring. It accelerates 400 MeV protons obtained from the Linac by stripping the electrons off the negative hydrogen ions. $H^-$ ions are merged with protons circulating in the booster using dipole magnets, and the combined beam is passed through carbon foil to strip electrons, as shown in Figure 2.3. The opposite charge of the injecting $H^-$ and the circulating proton allows to merge the beam efficiently. The booster consists of a series of magnets

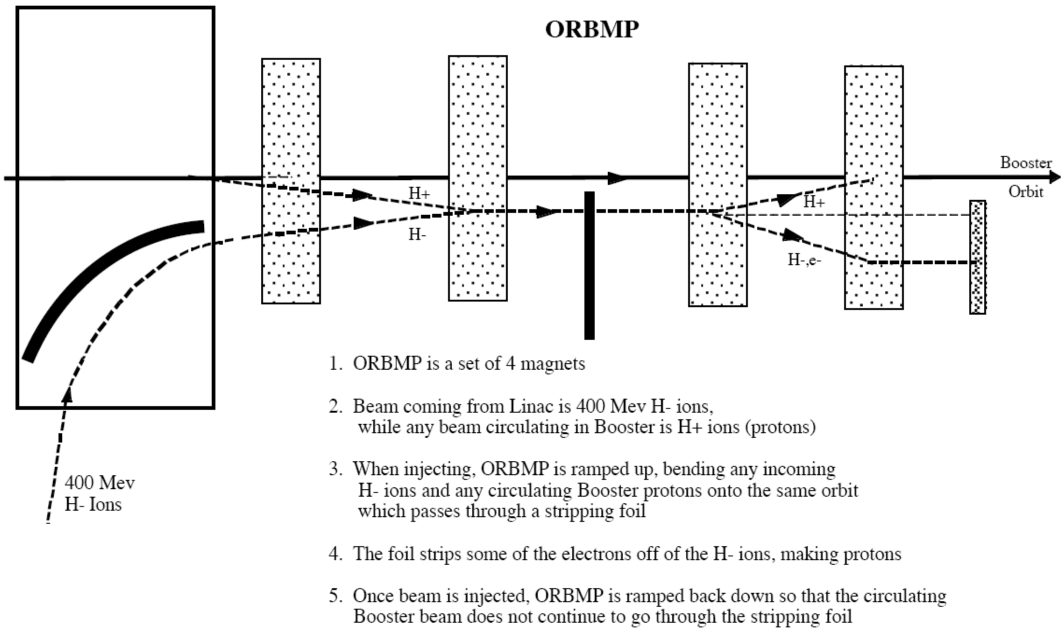


Figure 2.3: A schematic view of the Fermilab Booster injection area.

arranged around a 75-meter radius with 18 RF cavities.

### 2.1.4 Main Injector

The Main Injector is a synchrotron, which accelerates 8 GeV protons from the booster to either 120 GeV or 150 GeV. The Main Injector can accept both protons from the booster and antiprotons from the antiproton source. The Main Injector contains 20 RF cavities for particle acceleration and a series of dipole/quadrupole magnets for beam focusing and steering. When used to produce the antiprotons, the final energy is 120 GeV. When used to inject beams into the Tevatron, the final beam energy is 150 GeV.

### 2.1.5 Antiproton Source

The antiproton source [24] consists of a target station, a Debuncher ring, and an Accumulator ring. The 120 GeV proton beam from the Main Injector is delivered to a nickel target, producing the antiprotons in a shower of secondary particles. Antiprotons of 8 GeV energy are most effectively produced by a proton beam of about 120 GeV. About one antiproton is produced for every $10^5$ protons striking the target. The secondary particles are collected

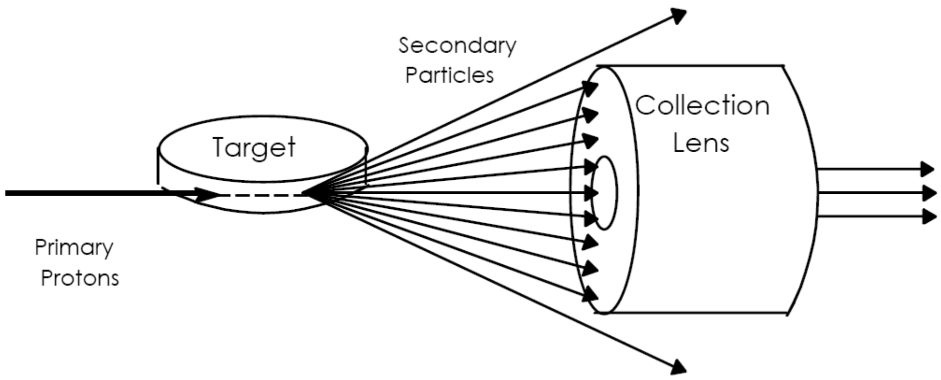


Figure 2.4: A simple view of the target station.

and focused by a cylindrical lithium lens, as shown in Fig. 2.4. Lithium is the least-dense solid conductor which reduces the antiproton absorption and multiple scattering. 8 GeV antiprotons are selected by a pulsed dipole magnet and delivered to the Debuncher.

The Debuncher is a rounded triangular-shaped synchrotron with a mean radius of 90 meters. It reduces the high momentum spread of antiprotons from the target station to improve the transfer the Debuncher the to Accumulator through bunch rotation and adiabatic debunching. Both (transverse) stochastic cooling [31] and (longitudinal) momentum cooling are applied to reduce the beam size and momentum spread. The Debuncher keeps the antiproton energy at 8 GeV.

The Accumulator is also a triangular-shaped synchrotron of radius 75 meters and is in the same tunnel as the Debuncher. Its purpose is to accumulate antiprotons extracted from the Debuncher. All of the antiprotons made are stored here at 8 GeV and cooled through the several different cooling systems. After several hours, enough antiprotons have been accumulated, antiprotons are transfered to the Main Injector and the Tevatron for a store (or to the Recycler via the Main Injector).

### 2.1.6 Recycler

The Recycler is an antiproton storage ring located along the ceiling of the Main Injector tunnel, which keeps the antiproton energy at 8 GeV. The originally proposed purpose of the Recycler was to recycle the antiprotons from Tevatron stores. The recycler now accepts the antiproton beam only from the antiproton source and cools further than the Accumulator is capable.

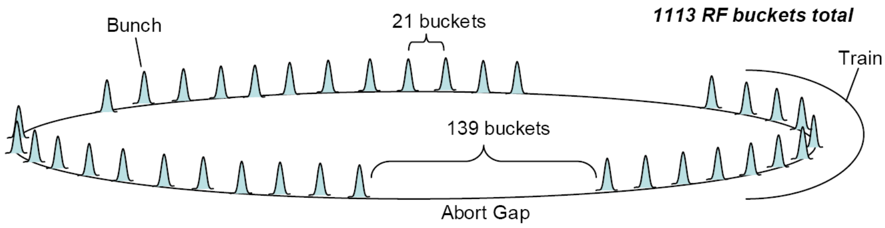


Figure 2.5: Bunch spacing in the Tevatron.

The Recycler uses both a stochastic cooling and an electron cooling system [32]. The recycler uses the stochastic cooling until the intensity reaches $2 \times 10^{12}$ particles per pulse. The electron cooling is used to cool the antiprotons further.

### 2.1.7 Tevatron

The Tevatron is a 1 km radius synchrotron which accelerates protons and antiprotons from 150 GeV to 980 GeV [26]. All dipole, quadrapole, and correction element magnets are superconducting magnets, cooled to about 4.6 K with liquid Helium. Proton and antiproton collide at the positions of CDF and DØ detectors. The separators around the ring separate the proton bunches from the antiprotons except at the collision regions. There are three trains of 12 bunches and an abort gap between the trains in the Tevatron, as shown in Figure 2.5.

In the collider mode the Tevatron can store beams for hours once they are injected. The collision rate of proton-antiproton interactions is given by

$$R = \sigma_{\mathrm{int}} \mathcal{L}, \tag{2.1}$$

where $\mathcal{L}$ is the instantaneous luminosity. It depends on the revolution frequency $f$ and the area $A$ that the beam occupies. If $N_p$ and $N_{\bar{p}}$ are the number of particles in each bunch and $n$ is the number of bunches in either beam, then the luminosity $\mathcal{L}$ can be expressed by

$$\mathcal{L} = \frac{f n N_p N_{\bar{p}}}{A}. \tag{2.2}$$

This stable situation of 1960 GeV proton-antiproton collisions is called a *store*. The typical luminosity at the beginning of the stores in 2007 was $\sim 2 \times 10^{32}$ cm$^{-2}$s$^{-1}$ as shown in Fig. 2.6. The store luminosity continually decreases from its initial value as protons and antiprotons are consumed

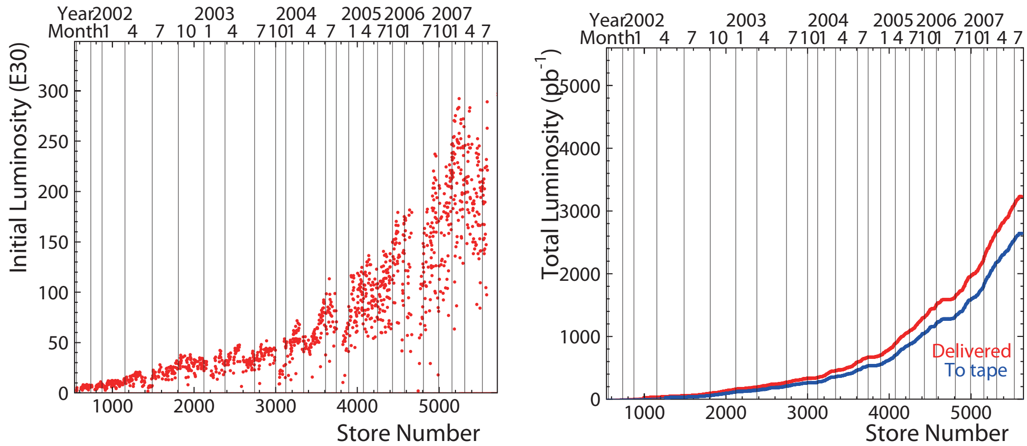


Figure 2.6: Tevatron Peck and integrated luminosity.

through interactions and as the bunch emittance increases with time. The effect at the beginning of a store is largely dominated by emittance growth due to intrabeam scattering, while after several hours of running the effect of antiproton loss becomes more important and the luminosity falls off exponentially. In about 20 hours the luminosity drops too low, then the store is ended and the Tevatron prepare for new beam. This sequence of the stores continues 24 hours a day except for some short periods of time allocated for maintenance.

The integrated luminosity $\int \mathcal{L}dt$ is the measure of the number of collisions during a time period. Figure 2.6 shows integrated luminosity of RunII data taking since 2001. The analysis corresponds to the integrated luminosity of 2 fb$^{-1}$ during December 2004 to May 2007.

## 2.2 The Collider Detector at Fermilab (CDF)

The Collider Detector at Fermilab (CDF) [33] is a multipurpose detector designed to observe a wide rage of physics processes produced in high-energy $p\bar{p}$ collisions. Figure 2.7 shows a cross-sectional view of the CDF detector.

It combines charged particle tracking with calorimetry and muon detection. The detector electronics has been significantly upgraded to accommodate high instantaneous luminosities and to improve the performance in momentum resolution, $b$-tagging, electron and muon identification. The CDF has both azimuthal and forward-backward symmetry about the transverse plane passing through the interaction point, which results in the naturally

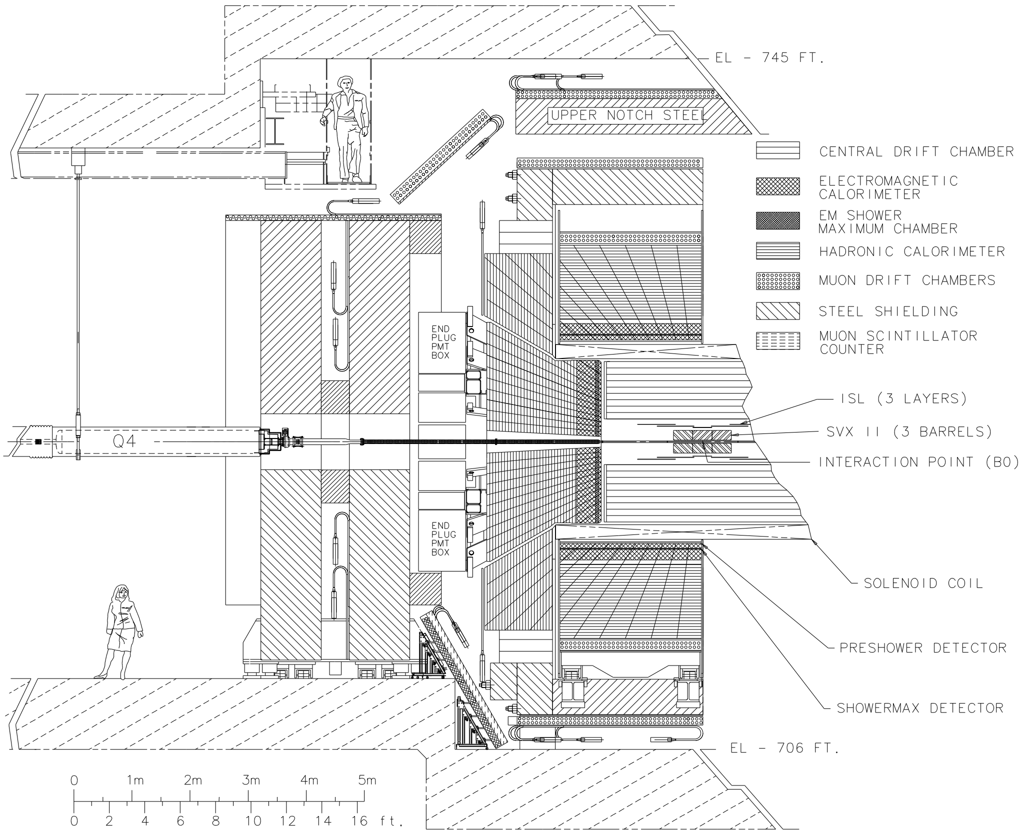


Figure 2.7: A cross-sectional view of the CDF detector [33].

arising cylindrical coordinate system. The coordinate system is right-handed with the $z$-axis pointing in the proton momentum direction and the $y$-axis in the upward vertical direction. It is more convenient to identify locations of the particles in $\phi$-$\eta$ space, where $\phi$ is the azimuthal angle and $\eta$ is the pseudorapidity expressed in terms of the polar angel $\theta$ as

$$\eta = -\ln\left(\tan\frac{\theta}{2}\right). \tag{2.3}$$

Since the pseudorapidity is

$$\eta = \frac{1}{2}\ln\left(\frac{E+p_z}{E-p_z}\right) + \mathcal{O}\left(\epsilon^2\right) \tag{2.4}$$

where $\epsilon = \frac{m}{p_T}$, a measure of the opening angle between two particles give by

$\Delta R$:

$$\Delta R = \sqrt{(\Delta\eta)^2 + (\Delta\phi)^2} \tag{2.5}$$

is Lorentz invariant.

The CDF Detector consists of the following three main functional sections going radially outwards from the beam line.

- The tracking system is used for particle charge and momentum measurements. It is immersed in a superconducting solenoid of 4.8 m in length and 1.5 m in radius, which produces a 1.4-T magnetic field coaxial to the $p\bar{p}$ beams.
- The solenoid is surrounded by the scintillator-based calorimeter system with separate electromagnetic and hadronic measurements, which covers the region $|\eta| \leq 3$.
- Outside of the calorimeters, layers of steel absorb the remaining hadrons leaving only muons, which are detected by the outermost muon detectors. In the next sections we discuss the functionality of the main CDF detector components.

## 2.3 Cherenkov Luminosity Monitor

The beam luminosity measurement is crucial part for the entire experiment. It is determined from the rate of inelastic $p\bar{p}$ interactions, called *minimum bias* events. The measurement is obtained with low pressure gaseous Cherenkov counter [34] placed in the forward and backward region at small angles $\theta \leq 3°$ relative to the beam direction, as shown schematically in Figure 2.8. The 48 thin, long, conical counters are located on each side of the detector. The counters are arranged around the beam pipe in three concentric layers with 16 counters, each oriented with their small end pointing to the center of the interaction region, and cover the pseudorapidity range $3.7 < |\eta| < 4.7$. The cones in the outer two layers (further away from the beam pipe) are about 180 cm long. The inner layer counters are shorter, about 110 cm, due to geometrical constraints. At the large aperture of the cones, furthest from the interaction region, the aluminum conical light collectors are attached. At the small end of the light collectors 2.5 cm diameter photomultiplier tubes (PMT) are placed. The completed structure in enclosed in a vessel filled with isobutane, which is used as radiator [1]

[1]Isobutane has one of the largest indices of refraction at atmospheric pressure for commonly available, $n$=1.00143, and good transparency for photons in the ultra-violet region where most Cherenkov light is emitted [35].

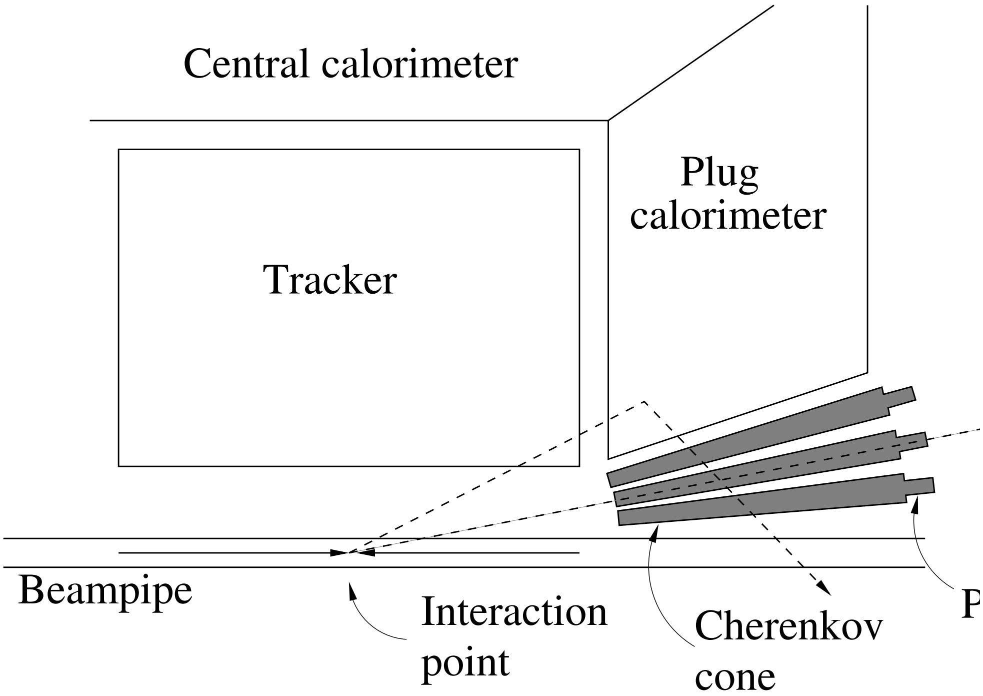


Figure 2.8: Schematic view of luminosity monitor inside a quadrant of the CDF detector.

The Cherenkov light emission angle $\theta_c$ is determined by the gas refraction index $n$ and the particle velocity $\beta$:

$$\cos\theta_c = \frac{1}{n\beta} \tag{2.6}$$

The number of photoelectron produced by a charged particle $N_{p.e.}$ in Cherenkov counters is proportional to the length of particle's path $L$ inside the counter and to $\sin^2\theta_c$ [36]:

$$N_{p.e.} = N_0 \cdot L \cdot \sin^2\theta_c, \tag{2.7}$$

where $N_0 \sim 200$ cm$^{-1}$ is the counter design specific parameter.

The prompt particles from $p\bar{p}$ interactions traverse the full length of the counter and generate a large amplitude PMT signal, $\sim$ 100 photoelectrons. While the signals from particles originating from beam-halo interaction or from secondary interactions in the detector material are significantly smaller because those particles have lower momenta and they traverse the counters at larger angles with shorter path lengths, hence their light experiences large losses due to the reflections.

The high precision of the luminosity monitor is provided by the fact that the counters effectively measure the actual number of primary particles. If two particles pass through a single counter the resulting signal is twice that of a single particle. Therefore the Cherenkov monitor does not saturate at high operational luminosities in the Tevatron.

## 2.4 Silicon Tracking System

The CDF tracking system consists of a series of concentric semiconductor and gaseous detectors. At large radii the charged particle tracking in the central pseudorapidity region ($|\eta| < 1.0$) is done with a large open cell cylindrical drift chamber, the Central Outer Tracker (COT). Inside the COT a silicon micro-vertex detector surrounding the beryllium beam pipe establishes the ultimate impact parameter resolution and provides stand-alone silicon tracking in the region of $|\eta| < 2.0$

The silicon detector is comprised of eight layers of microstrip silicon sensors arranged in cylinders spanning radii from 1.35 cm to 28 cm, and lengths from 90 cm to nearly two meters. It is divided into three sub-systems: L00, SVXII and ISL with a total of six square meter of silicon and 722,000 readout channels.

A schematic view of the principal active components of the CDF silicon system is given in Figure 2.9 and 2.10. The side view shown in Figure 2.9 is a cross section of one half of the silicon tracker. Figure 2.10 shows an end view of the CDF silicon system including the VSXII bulkheads and ISL support frame.

The L00 ("Layer Zero Zero") [37] detector is the innermost single-sided layer of low-mass silicon-microstrips mounted directly over the beam pipe at a radius of $sim$ 1.6 cm from the beamline with a total length of 80 cm. Due to its proximity to the beamline it substantially improves the impact parameter resolution. The L00 utilizes radiation tolerant axial strip sensors expected to last at least 7.4 fb$^{-1}$. Radiation resistance is achieved with a guard structure designed to minimize leakage currents. The sensors have an implant pitch of 25 $\mu$m and a readout pitch of 50 $\mu$m achieved by reading out alternate strips. The L00 is connected to electronics outside the tracking volume at $|z| > 40$ cm via fine-pitch kapton cables carrying the signals from the sensors to the readout chips.

The next five double-sided layers of the tracker positioned at radii from 2.34 to 10.6 cm comprise the Silicon Vertex Detector (SVXII) [38]. The

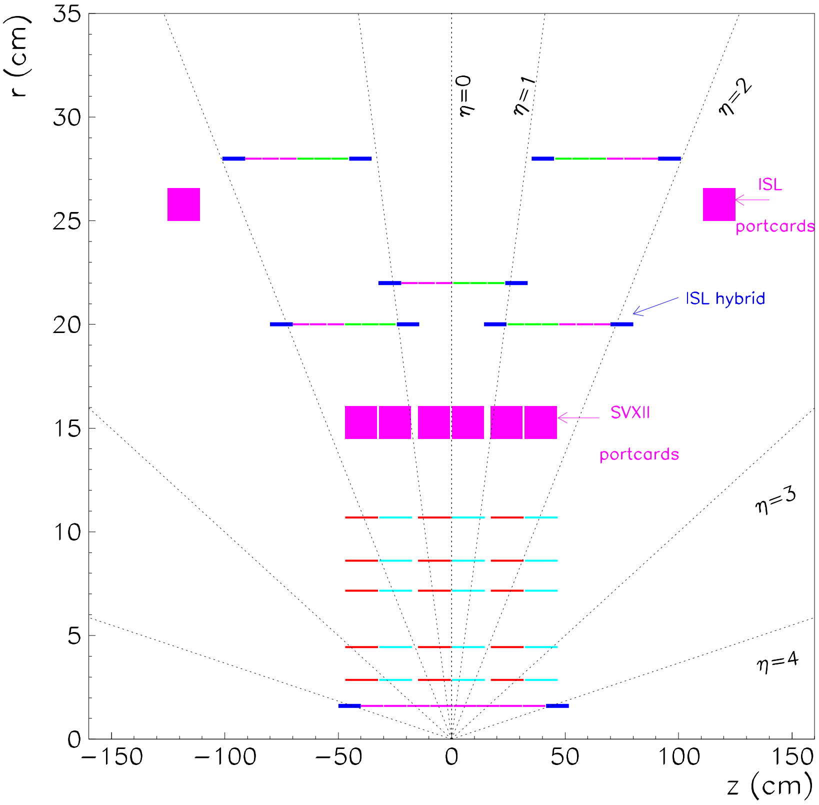


Figure 2.9: A side view of half of the CDF silicon system.

layers of the SVXII and L00 are arranged in twelve azimuthal wedges that alternated in radius within each layer (see Figure 2.11). The SVXII is 96 cm long and is assembled in three cylindrical barrels with beryllium bulkheads at each end. A printed circuit board, called the Port Card(PC), located around the periphery of the bulkheads interfaces the hybrids and frontend chips with the rest of the readout data acquisition system by translating the readout into optical format for transmission outside the tracking volume.

The basic structural unit of the SVXII detector is called a *ladder*, which consists of two readout units of silicon with an electrical hybrid at each end. The units are mounted directly atop the silicon surface to avoid gaps and to improve readout speed and capacitance limitations.

Both 90-degree and small-angle stereo sensors are used in the SVXII, in the pattern $(90°, 90°, -1.2°, 90°, +1.2°)$ for the n-strip from the innermost

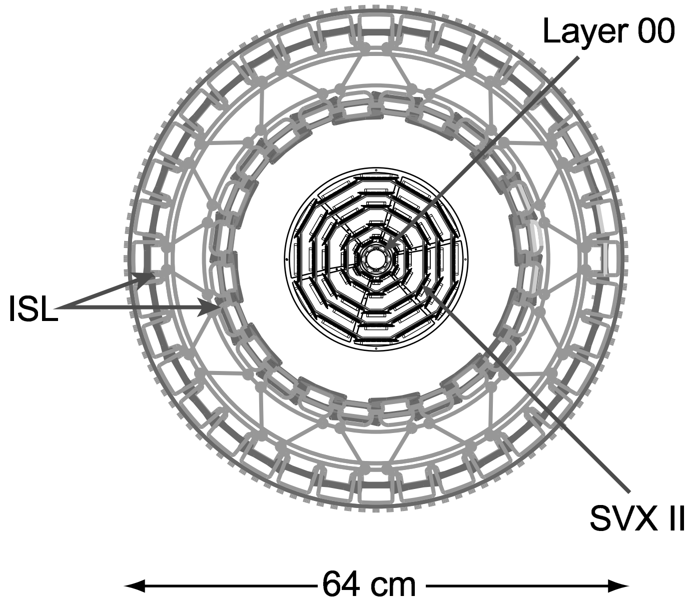


Figure 2.10: An end view of the CDF silicon system including the SVXII cooling bulkheads and ISL support structure.

to outermost SVXII layers, SVXII sensors are AC coupled, 300 $\mu$m thick, and made from n-type high resistivity bulk silicon. They are biased using polysilicon resistors. The p-strips on the non-stereo side run in the axial direction of the detector re used to measure the azimuthal angle $\phi$ of the track. These strips are spaced in $r\phi$ by 60-65 microns, depending on the ladder, and have implant widths of 14 to 15 microns. The stereo n-strips of the SVXII are spaced by (141, 125.5, 60, 141, 65) microns, and have implant width of 20 microns for the 90° strips and 15 microns for the small-angle stereo layers. The 90° layers have an additional layer of insulator and readout strips in the double-metal configuration; these strips carry the Z signals to the readout chips.

The Intermediate Silicon Layers (ISL) detector is placed outside of the SVXII. Its space frame also supports the SVXII and all associated readout and utility components. The ISL consists of two symmetric silicon layers in the forward and backward region ($|\eta| \geq 1.1$) located at radii of R $\simeq$ 20 cm and R $\simeq$ 29 cm respectively and one int he central region ($|\eta| < 1.1$) at R $\simeq$ 23 cm. It provides one space point in the central region which improves the linking between SVXII tracks and COT tracks and its fine granularity helps to resolve ambiguities in dense track environments. In the forward region, where the COT acceptance rapidly decreases, the ISL together with

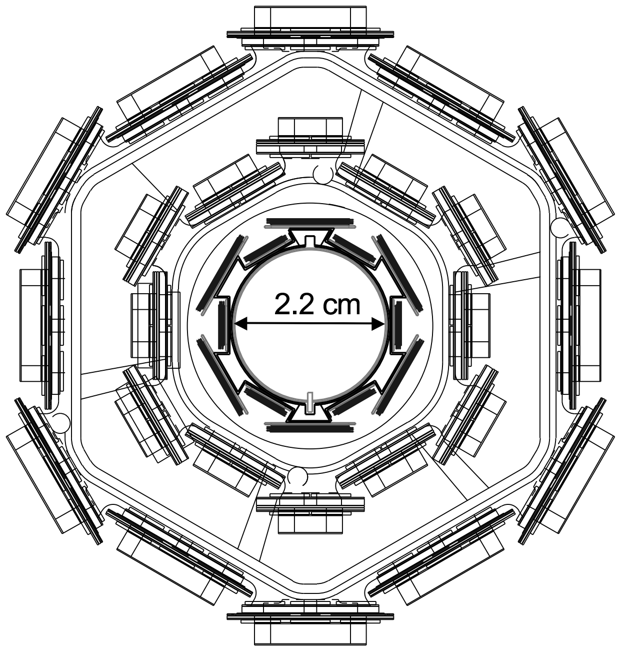


Figure 2.11: End view of the innermost three layers of the CDF silicon system, showing Layer00 along with the first two layers of the SVXII region. The Layer00 electronics (not shown) are mounted beyond the active volume for vertexing. The SVXII electronics are shown just outside and just inside of each of the layers drawn.

the SVXII constitutes a standalone 3D tracker out to $|\eta| \simeq 2.0$ (see Figure 2.12).

The ISL also utilized AC coupled double-sided sensors with polysilicon biasing and common p-stops. Due to its large radial position radiation damage occurs more slowly and the hit occupancy is lower, it is therefore possible to use longer strips and a large readout pitch to reduce the number of readout channels. A fixed strip pitch of 112 $\mu m$ is used on both the axial and 1.2-degree stereo sides. Pitch adapters are used to bring the signals from the strips to the more closely spaced inputs of the readout chips.

The ISL ladders are composed of six sensors, arranged as half-ladders of three sensors each. Silicon sensors are bonded together to form a single electrical unit and glued on a carbon fiber support. At each ladder end they are readout with double-sided hybrids that extend beyond the silicon.

All components of the silicon system achieve their data readout by the SVX3D [40] chip, a radiation-hard CMOS custom integrated circuit (IC) device. Each IC has 128 parallel analog inputs and 8-bit digital output

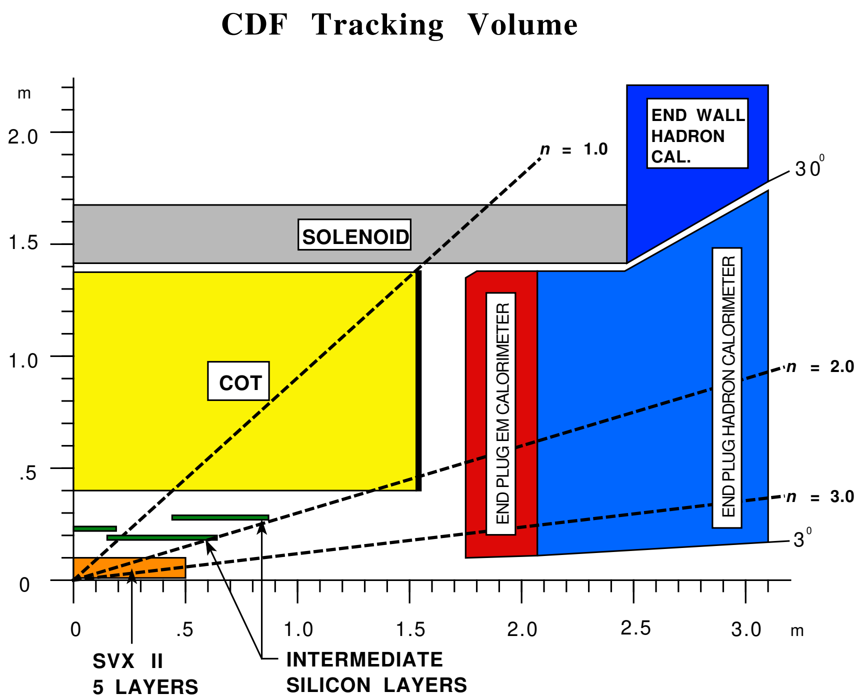


Figure 2.12: A cutaway view of one quadrant of the inner portion of the CDF detector showing the tracking region surrounded by the solenoid and endcap calorimeters.

bus. Each channel contains a preamplifier, an analog delay pipeline, ADC (8 bits), and data sparsification logic. In order to maximize the physics potentiality of the CDF silicon detectors, the SVX3D has been designed to work in continuous (dead timeless) mode, being capable of simultaneous acquisition, digitization and readout operation.

The silicon is actively cooled to remove heat due to SVX3D chip power as well as that due to leakage currents after irradiation. Water/ethylene glycol coolant mixture of - 5°C for the silicon and electronics flows within internal channels that are machined into the SVXII beryllium bulkheads at each barrel end, and in aluminum tubes attached to beryllium wedges mounted on the ISL space frame.

## 2.5 Central Outer Tracker (COT)

The Central Outer Tracker (COT) is located outside the silicon microstrip detectors within a 1.4-T solenoidal magnetic field [41]. It is designed to find

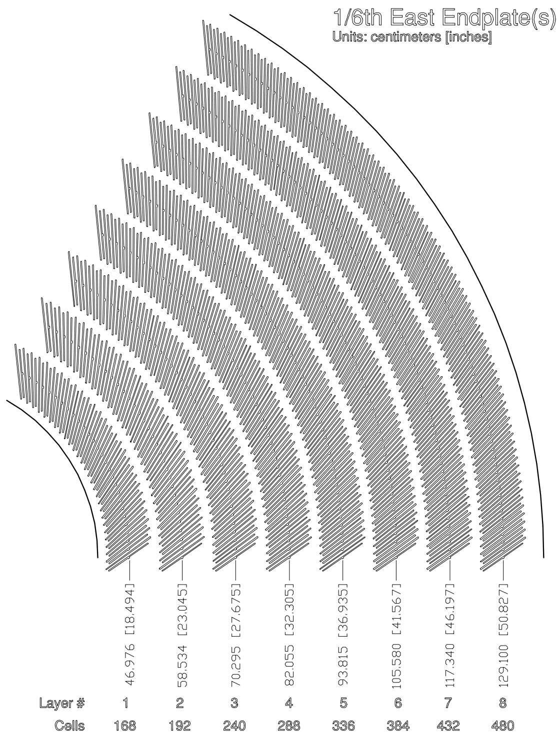


Figure 2.13: A view of a portion of one COT end plate. The slots define the radii of the 8 superlayers. Within a superlayer, wire-plane slots and sheet slots alternate.

charged tracks in the central region $|eta| < 1.0$ with transverse momentum $p_T$ as low as 400 MeV, and link tracks to hits in the inner silicon detectors.

The active volume of the COT spans 310 cm in the beam (axial) direction z, and between 44 cm and 132 cm in radius. It is filled with $Argon-Ethane-CF_4$ (50:35:15) mixture bubbled through isopropyl alcohol. This gas mixture provides a fast drift velocity $\sim$ 100 $\mu m/ns$ that is essential for lowering a maximum drift time. The maximum drift time is required to be less than the 396 ns bunch spacing, and with this gas it is about 100 ns in the drift field $\sim$ 2 kV/cm. This makes the COT immune to event pile-up, even at the highest collision rate of 1/(132ns).

The COT is comprised of 30,240 sense wires running the length of the chamber and strung between two precision-machined aluminum end plates. The sense wires are grouped into eight *superlayers*, shown in Figure 2.13, that alternate axial-stereo with a stereo angle of $\pm 2°$.

Axial superlayers provide accurate tracking information in the $r-\phi$ view. Stereo superlayers provide tracking information in the $r-z$ view, substan-

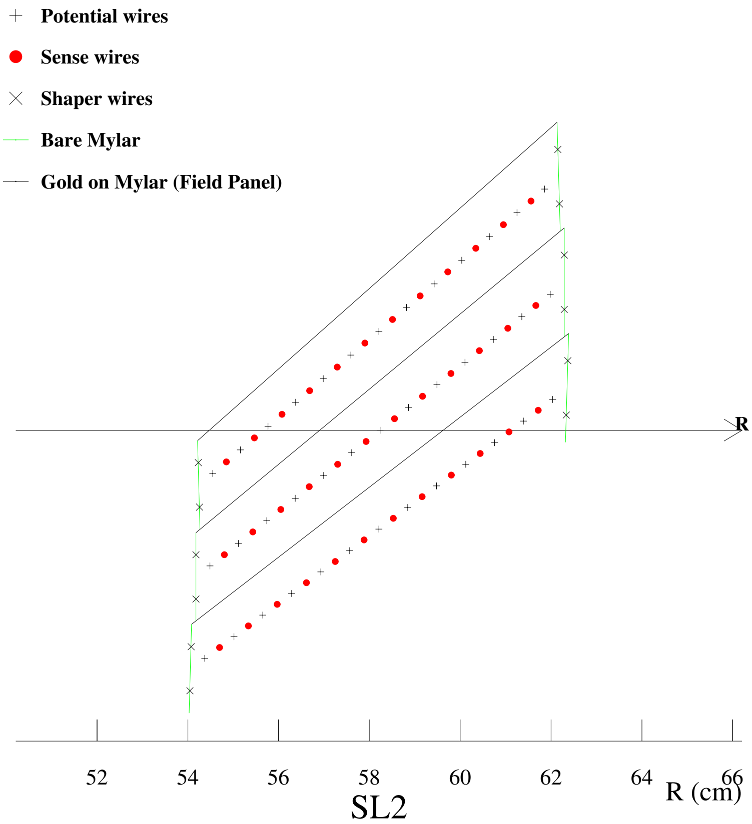


Figure 2.14: Three COT cells. Each cell has 12 sense wires, 13 potential wires, 4 shaper wires and a gold-mylar cathode field panel on both sides of the sense wire plane.

tially less accurate, and are designated to measure $\eta$ of the track. Each superlayer is divided in $\phi$ into *supercells* and each supercell has 12 sense wires yielding total 96 measurement layers. A maximum drift distance is established to be approximately the same for all superlayers by scaling the number of supercells in a given superlayer with the radius.

It consists of 12 sense wires and 13 potential wires that alternate. Potential wire are exposed and sense wires are placed at the midpoint between couple of successive potential wires. Four shaper wires serve to close the supercell electro statically. A field sheet (cathode) is placed on both sides. Each field sheet is shared with the neighboring supercell. The supercell is tilted by $35°$ with respect to the radial direction to compensate for the Lorentz angle of the drifting charged particles in the magnetic field.

The field sheet is maintained at ground potential. The potential wires are run at positive high voltage, $\sim 2$ kV, and the sense wires are run at $\sim 3$ kV. In order to maintain a uniform drift field actual voltages slightly differ (less than 400 V) with the variation across a cell for the sense and potential wire voltages.

Wire readout is performed via a custom-built ASD (amplifier, shaper, discriminator) radiation-hard 8-channel chip. ASD boards are placed directly on the chamber endcap. Pattern recognition logic allows multiple hits to be recorded within a single sense wire.

Particles of charge $q$ moving in a uniform magnetic field $\overrightarrow{B}$, inside of the CDF tracker, have a helicoidal trajectory with the radius of curvature

$$r = \left| \frac{p_T}{qB} \right| \tag{2.8}$$

One obtains the particle's transverse momentum $p_T$ by reconstructing COT hits that define the particle trajectory and measuring the radius of curvature of helix $r$.

The momentum resolution of the COT is

$$\sigma(1/p) = 0.11\% \tag{2.9}$$

In addition, the COT provides particle identification information based on the ionization less $dE/dx$ measurement. To enhance particle identification capabilities, the time-of-flight detector is placed at the outer edge of the COT. It consists of an array of scintillator bars about three meters long, matching the COT active volume. Photomultiplier tubes attached to the both ends of each par provide time and pulse height measurements.

Particle identification is performed by measuring the time of arrival of a particle at the scintillator with respect to the collision time. The particle mass $m$ can be then determined based on its momentum $p$, the path length $L$ and the time of flight $t$.

$$m = \frac{p}{c}\sqrt{\left(\frac{ct}{L}\right)^2 - 1} \tag{2.10}$$

The time of flight $t$ is measured with resolution $\sim 130$ ps which provides a capability to distinguish between light $K^{\pm}$ and $\pi^{\pm}$ hadrons and search for new stable massive particles up to 500 GeV.

## 2.6 Calorimeter

Charged particles of interest with transverse momenta grater than 350 MeV escape the magnetic field, and are detected by the calorimeters outside of solenoid.

The calorimeters are separated into two regions. The central calorimeter provides coverage over $|\eta| < 1.1$ and the plug calorimeter covers the pseudorapidity region $1.1 < |\eta| < 3.4$, corresponding to polar angles between $37°$ and $3°$. Each calorimeter consists of electromagnetic (EM) and hadronic (HAD) parts, both segmented into projective towers[42, 43]. A collision product meets first the EM part, and then traverses through the HAD part. The amounts of energy of a particle deposited in each part of the calorimeter are referred as an electromagnetic and hadronic energies respectively. The electrons and photons leave most of their energy in the EM part, while hadrons lose their energy predominantly in the HAD part of the calorimeter.

The central calorimeters are divided azimuthally into 24 wedges, each covering an azimuthal angel of $15°$ and extending about 250 cm along the beam axis on either side of $z = 0$. The central electromagnetic calorimeter (CEM) starts at a radius of 173 cm and is 35 cm thick, after that the hadronic calorimeter (CHA) begins. the segmentation in pseudorapidity forms calorimeter towers, which project back to the nominal interaction point. Each tower covers $\Delta\eta = 0.11$, with a CHA tower directly behind the matching tower in CEM. This allows one to measure the ratio of electromagnetic to hadronic energy for each individual tower. A schematic of a single central calorimeter wedge, showing both CEM and the CHA, and the tower geometry if shown in Figure 2.15.

The calorimeters are made of alternating layers of absorber material with a high nuclear number Z and the active readout material. In the electromagnetic section the absorber is lead, and in the hadronic section it is iron. The polystyrene scintillator serves as an active material. The CEM is composed of 5 mm thick layers of scintillator and 3 mm layers of lead, while for the CHA layers are thicker and arranged in 1.0 cm and 2.5 cm respectively.

As particles traverse through the absorber, they lose energy and produce cascades of secondary particles, showers, which then interact in the scintillators. The showers penetrate through many layers, and are sampled by the scintillators until they are completely absorbed. The scintillator's light is collected through acrylic light guides attached to photomultipliers, which are located at the rear end of each wedge, as shown in Figure 2.16.

The amount of light is a measurement of the incident particle's energy.

The CEM thickness corresponds to 18 radiation lengths $X_0$, and its energy resolution is [42]:

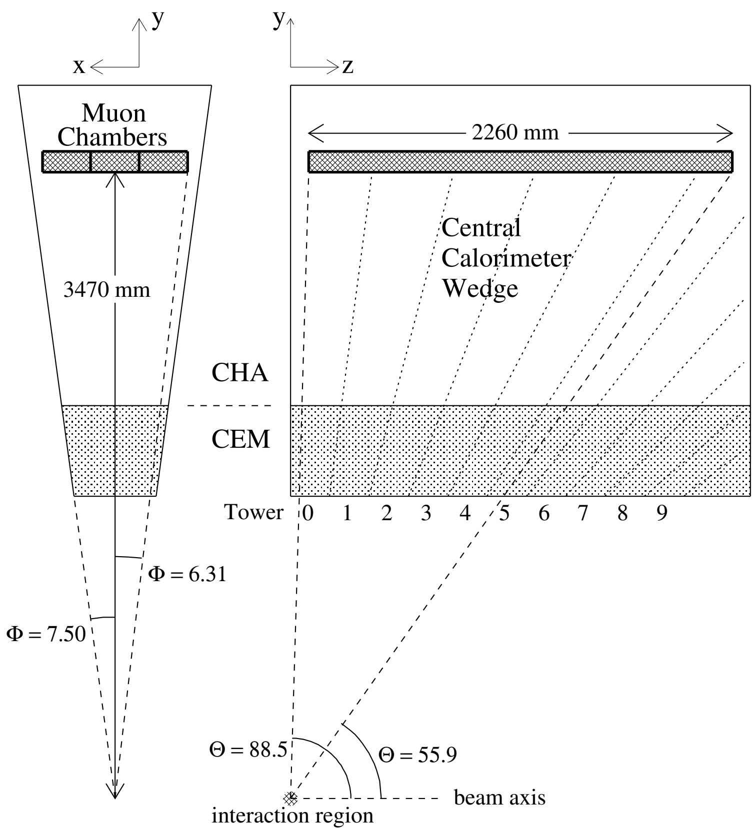


Figure 2.15: Geometry of a central calorimeter wedge and its towers.

$$\frac{\sigma_E}{E} = \frac{13.5\%}{\sqrt{E_T}} \oplus 2\% \tag{2.11}$$

where $\oplus$ means that the constant term is added in quadrature. The first term comes from sampling fluctuations and the photostatistics of PMTs, and the second term comes from nonuniform response of the calorimeter.

The CHA is about 4.5 attenuation lengths $\lambda_I$ thick, with the energy resolution give by [43]

$$\frac{\sigma_E}{E} = \frac{50\%}{\sqrt{E_T}} \oplus 3\% \tag{2.12}$$

Transverse development of the electromagnetic showers is different for electrons and hadrons. To enable a more precise measurement of the transverse profile a proportional strip and wire chamber, call the central electromagnetic shower counter (CES), is embedded in each tower of the central calorimeter at location where maximal average electromagnetic shower deposition occurs ($5.9X_0$). The CES has cathode strips running in the azimuthal direction, which provide $r - \phi$ information. In addition to the CES, the central preradiator detector (CPR) composed of scintillator and PMT are placed between the solenoid and the CEM. Both the CES and CPR help in distinguishing electrons from hadrons.

The plug calorimeter comprises towers with the same structure as in the central calorimeter. Figure 2.17 shows the plug calorimeter structure.

The electromagnetic section with shower position detection is followed by a hadronic section. The plug calorimeter is divided in 12 concentric $\eta$ regions, which are further segmented in 24 for $|\eta| < 2.11$, or 12 for $|\eta| > 2.11$ projective towers. Figure 2.18 shows the segmentation of plug calorimeter.

The EM section of the plug calorimeter (PEM) consists of 23 absorber-scintillator layers. A calcium-tin-lead alloy enclosed between steel plates serves as an absorber. The total PEM thickness corresponds to 21 $X_0$, radiation lengths, and its energy resolution is [44]

$$\frac{\sigma_E}{E} = \frac{14.4\%}{\sqrt{E_T}} \oplus 0.7\% \tag{2.13}$$

The first layer of the EM section is used as a preshower detector(PPR). Its structure is the same as the other EM layers except the first scintillator is thicker (10 mm instead of 4mm) and is readout separately from the rest of the calorimeter via multi-anode photomultiplier tubes (MAPMT). As in the central calorimeter, a shower maximum detector (PES) is also embedded in the plug EM section at a depth of $\sim 6X_0$, radiation lengths [45]. Within each region 5 mm wide scintillating strips are arranged in two layers in directions parallel to either edge of the sector. The two layers are denoted 'U' and 'V', and are being offset from the radial direction by $+22.5°$ and -22.5° respectively. This provides a two-dimensional measurement of the shower with a position resolution of $\sim$ 1 mm.

The PHA calorimeter is comprised of 23 unit layers composed of 5 cm iron and 6 mm scintillator. It is about 7 $\lambda_I$ thick with the energy resolution

$$\frac{\sigma_E}{E} = \frac{80\%}{\sqrt{E_T}} \oplus 5\% \tag{2.14}$$

## 2.7 Muon Detectors

After escaping the tracking system, muons interact minimal within the calorimeter and are detected with arrays of drift tubes in the outermost part of the detector. The CDF muon system has four separate detectors: CMU, CMP, CMX and IMU. The central muon chambers (CMU) and the central muon upgrade chambers (CMP) cover the pseudorapidity range $|\eta| < 0.6$. The central muon extension chamber (CMX) provide coverage at $0.6 < |\eta| < 1.0$. The intermediate muon detector (IMU) are capable to identify muons in the forward region up to $|\eta| \simeq 2.0$ [46]. The $\phi$ coverage is not complete. The CMU alone covers 84 % of the solid angle. The CMP cover 63%, and 53% is covered by both of these detectors. The CMX covers 71 % of the solid angle. The complete $\phi - \eta$ coverage layout is shown in Figure 2.19.

The CMU is housed within the central calorimeter wedges, directly behind the CHA (see Figure 2.16). Each CMU wedge covers azimuthally 12.6° with 2.4° gap between the wedges. Each wedge contains three muon towers and each muon tower consists of four radial layers of four rectangular drift cells. At the center of each drift cell a sense wire runs the length of the wedge (2260 mm). Pairs of sense wire are offset from each other by $\sim 2$ mm to provide unambiguous $\phi$ measurement by determining which sense wire was hit first. A track is measured with resolution of 250 $\mu m$ is the $r - \phi$ plane. The $z$-position of the track is obtained by comparing the pulse heights at each end of the sense wires. The resolution in the $r - z$ plane is 1.2 mm. Tracks measured in at least 3 of the 4 layers form a track segment, called a *stub*.

Beyond the CMU there is an additional 69 cm thick steel shielding to further reduce the number of "punch-through" hadrons escaping the hadronic calorimetry. Behind the steel there are four additional layer of drift chambers, which make up to central muon upgrade (CMP). The CMP operates very similarly to the CMU but contains only one anode wire per chamber, and the anode wires are not connected in couples, so that the CMP provides only the $r - \phi$ measurement of the track. Unlike the CMU chambers, which are arranged in towers, the CMP chambers are arranged in stacks positioned around the detector. The inner and outer surfaces of the CMP are lined with scintillator plates, called the CSP, used to provide timing information. The CMP partially compensate the CMU $\phi$ gaps but has gaps on its own in the region $80° < \phi < 100°$ and $260° < \phi < 280°$ due to the return yoke of the solenoid.

The muon coverage is extended by additional muon chambers, which constitute the central muon extension (CMX). The CMX is comprised of four conical arches of drift tubes with layers of scintillator, called the CSX, analogous to the CSP. The CSX sandwiches the CMX drift tubes and helps in the identification of real muons.

Detection of muons in the forward region is accomplished by the IMU, which consists of hour staggered layers of drift tubes and scintillator counters.

## 2.8 Data Acquisition System

Due to the high rate of the beam crossings, CDF employs a trigger system to reduce the event rate down to a manageable level while retaining data from small cross section interactions and maintaining high efficiency for the broad range of the physics processes. The reduction rate is determined by the speed at which data can be stored on tape.

The trigger system is comprised of three levels and is able to function with a 132 ns bunch separation while keeping dead time as short as possible. The trigger architecture is shown in Figure 2.20.

Each trigger level in fact consist of a number of separate triggers, each with certain selection criteria. Each successive level of the trigger processes fewer events than the preceding level, only those events which pass requirements of the preceding level, but it processes them with grater sophistication and requires more time per an event. Level 1 uses custom designed hardware to find physics objects based on part of the detector information and makes a decision by simply counting the number of objects. The Level-2 trigger makes use of hardware processors to do a limited event reconstruction. The Level-3 trigger is implemented in software, and it uses a processor farm running on the full data record of each event.

In the Level-1 trigger, the information from all detectors is buffered in a 42-event deep synchronous pipeline and stored for 5.5 $\mu sec$. During this time the received data is analyzed by three parallel synchronous streams. One stream finds calorimeter based objects (electrons, photons, jets), another finds stubs in the muon chambers, while the third one, the eXtremely Fast Tracker (XFT), reconstructs tracks on the transverse plane of the COT, and an extrapolation unit (XTRP) matches these tracks to the calorimeter and muon chambers.

The calorimeter triggers are formed by applying thresholds to energy depositions in calorimeter trigger towers with a segmentation of approximately $\delta\eta \times \delta\phi = 0.2 \times 15°$. The thresholds are applied to individual towers (object triggers) as well as to sum of energies from all towers (global triggers). Electron and photon triggers are formed by applying energy thresholds to the electromagnetic (EM) energy in a tower, while jet triggers are formed using the total (EM + HAD) energy in a tower. To identify electron/muon candidates the online track processor, the XTRP, links reconstructed XFT tracks with clusters in the EM calorimeter and pairs of hits in muon drift tubes. $p_T$ and $E_T$ thresholds are programmable for the various detector regions, and a flexible decision module can from up to 64 different triggers by setting requirements on the number and certain features of the objects from the Level-1 trigger streams. The decision module uses simple AND and OR gates, and each trigger rate can be prescaled to the desired value.

All elements of the Level-1 trigger are synchronized to the same clock and a decision is made every 132 nsec. The rejection factor is about 150, thus decreasing the event rate from 7.6 MHz to about 50 kHz.

Events satisfying the requirements of Level-1 trigger are downloaded into one of four asynchronous event buffers and processed via programmable Level-2 hardware processors. While Level-2 analyzes the events the buffer cannot be used for additional Level-1 accepts. If all four buffers are full then the experiment starts to incur deadtime. To keep the deadtime at an acceptable level of 10 % and maintain the 50 kHz Level-1 rate, the Level-2 latency is set to 20 $\mu$sec.

The first phase is an event building stage. Since jets usually affect more than one calorimeter tower, the cluster finder (L2CAL) combines the energies collected by single towers and forms clusters, thus providing a measurement of the total jet energy $E_T$ as well as average $\phi$ and $\eta$ of the jet. The shower maximum detectors (XCES) reduce the rate of fake electrons and photons by eliminating the background from single-phototube discharge and improving matching between XFT tracks and EM clusters. The Silicon Vertex Tracker (SVT) reconstructs tracks in the vertex detector and measure their impact parameter $d$.

On the second pipelined stage the results of the first phase are collected in the memory of the Level-2 processors, which examine the data if the criteria for any of the Level-2 triggers are satisfied. About one hundred different Level-2 triggers can be formed. The Level-2 accept rate is about 300 Hz with a rejection factor of about 150.

After being accepted by the Level-2 trigger, event fragments are collected in the data acquisition system (DAQ) buffers and then transferred via a network switch to Event Builder CPU nodes, called *converter nodes*, where events are assembled from their fragments to complete and with appropriate data structures for analysis. The events are then passed to the Level-3 farm of parallel processor nodes, which take advantage of the full detector information and improved resolution not available to the lower trigger levels. They analyze and classify each event and then make a decision by applying glittering mechanism. If the event is accepted, it is delivered to a permanent storage by the consumer-server logger system (CSL). In addition, a sample of events is sent to the online monitoring processes verifying that the detector, trigger and data acquisition system are functioning correctly. The rate of events trans erred to tape is around 75 Hz with an average event size of 2590 kB corresponding to up to 20 MB/s total output rate.

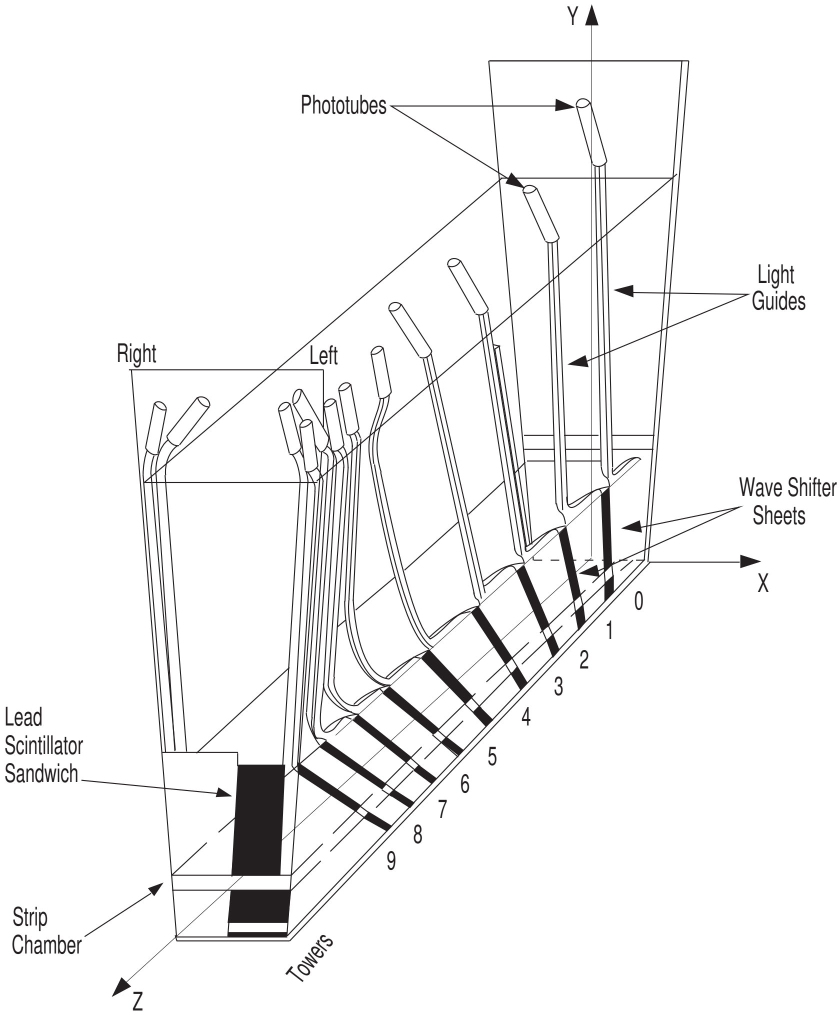


Figure 2.16: One of the wedge shaped modules of the central electromagnetic calorimeter. The ten $(\Delta\phi, \Delta\eta) = (15^\circ, 0.11)$ projective towers are shown.

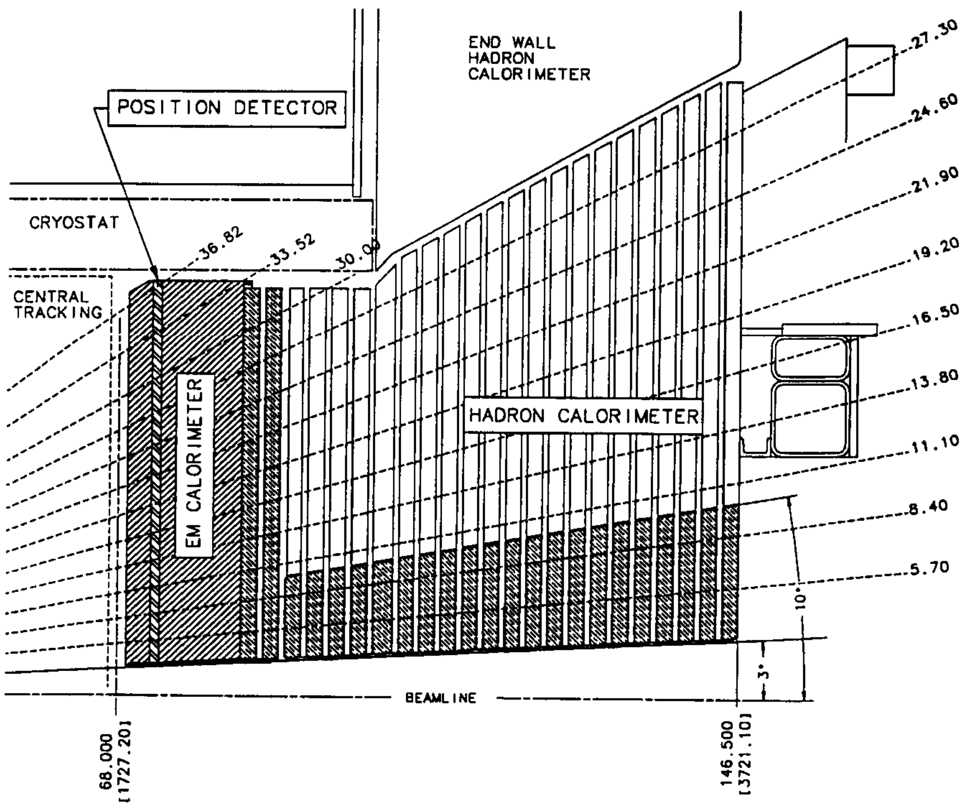


Figure 2.17: Cross section of an upper part of the plug calorimeter.

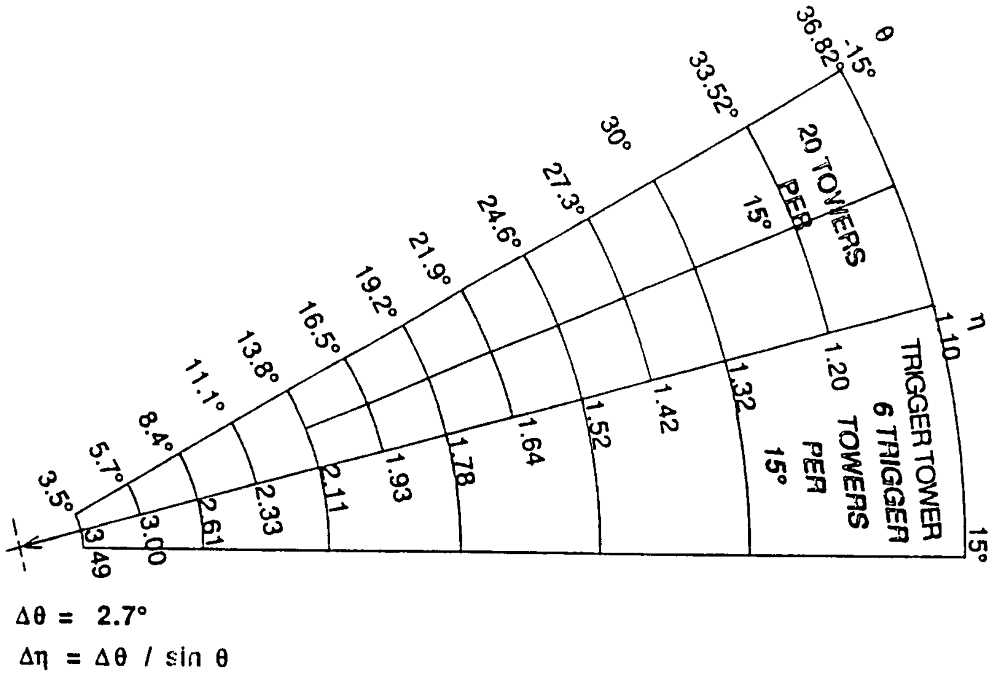


Figure 2.18: Tower segmentation of the plug calorimeter.

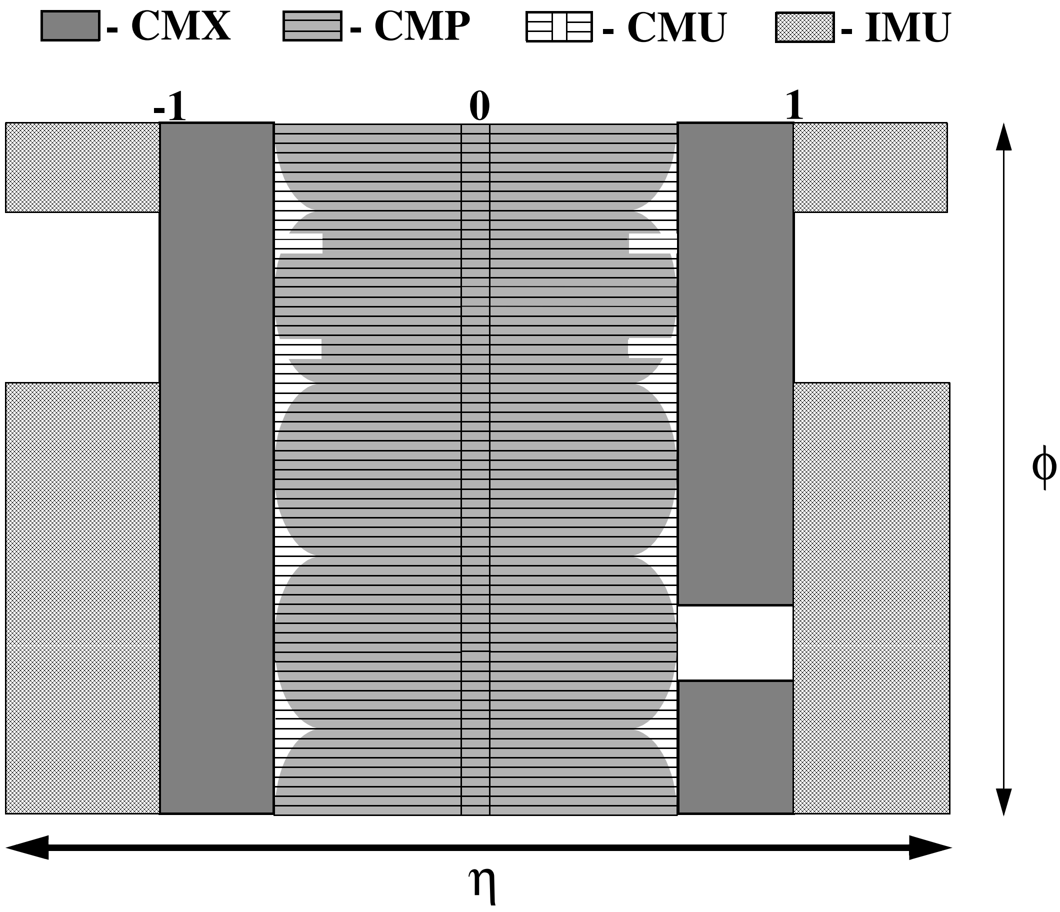


Figure 2.19: The $\eta - \phi$ coverage of the muon detector of CDF.

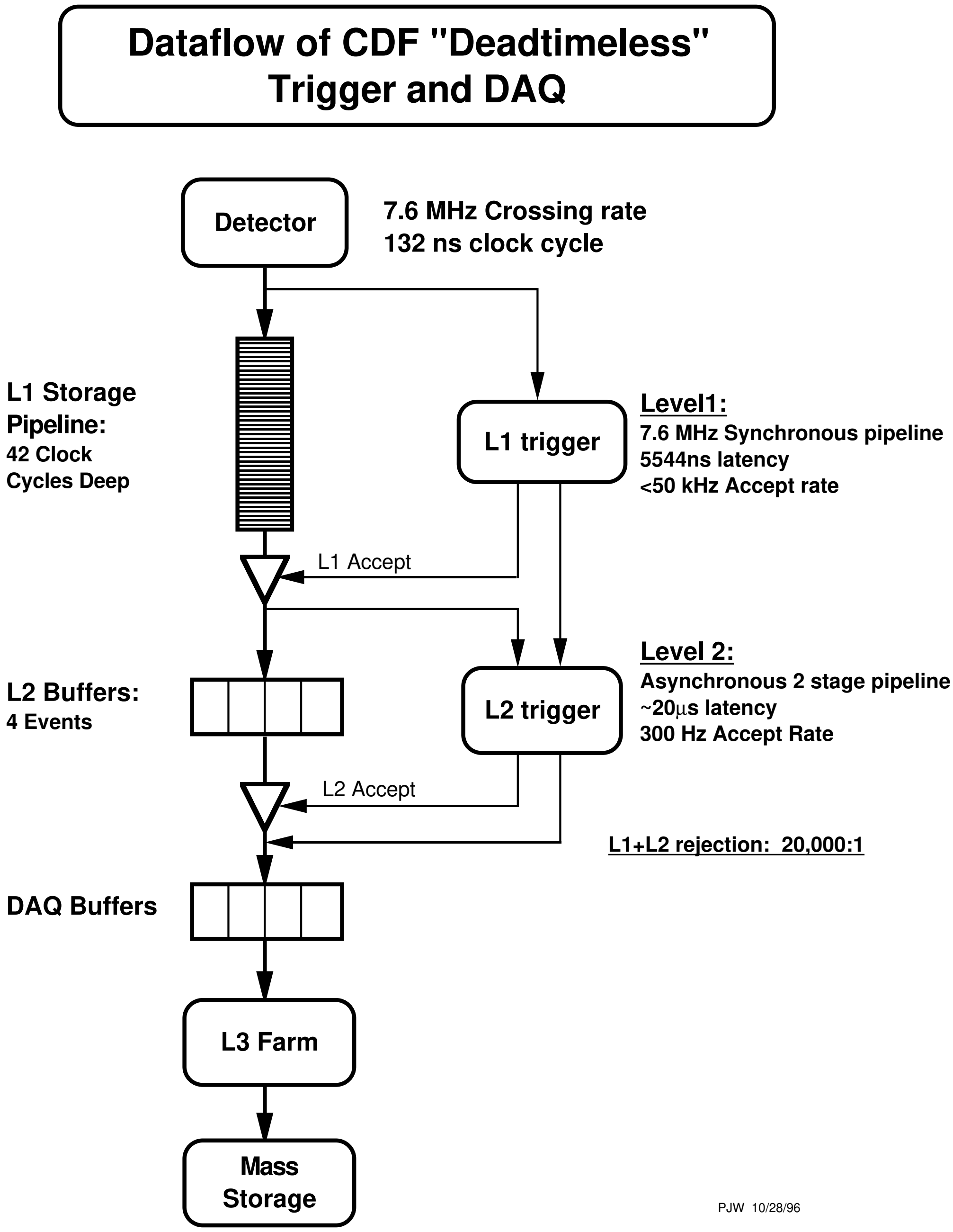


Figure 2.20: Functional block diagram of the CDF data flow.

# Chapter 3

# Reconstruction of Experimental Objects

As outlined in Chapter 1, the $t\bar{t}$ dilepton events ($p\bar{p} \to t\bar{t}X \to bW^+\bar{b}W^-X \to b\bar{b}l^+\nu l'^-\bar{\nu}X$) have a signature that is characterized by two high-$p_T$ leptons, electrons or muons, two high-$E_T$ jets and two neutrinos resulting in a large transverse energy imbalance, *missing transverse energy*, $\not\!\!E_T$.

This Chapter describes in detail the identification variables and criteria applied to identify final state objects in the event by the detector components. We start with the electron identification in the central and plug regions of the detector, discuss the requirements for muon candidates, describe the jet reconstruction algorithm and corrections to the jet energies, and the way we determine the energy of neutrinos escaping the detector. We describe the global event selection in the next chapter.

## 3.1 Electron Identification

Electrons resulting from the dilepton channel of the $t\bar{t}$ decay are highly energetic. They can be identified by a high-$p_T$ track in the drift chamber and large energy depositions in electromagnetic calorimeters. At energies of tens of GeV the dominant energy loss for electrons is bremsstrahlung. When electrons traverse the lead absorbers in the electromagnetic calorimeter, they interact with the nuclei of the material and emit photons which produce electron-positron pairs $e^+e^-$. The secondary particles are also very energetic and lead to production of an electromagnetic cascade, called a *shower*. The shape and position of the electromagnetic shower is measured by shower maximum detectors, and the shower characteristics are used in electron identification. A hadronic shower is longer and much broader. Electrons deposit most of their energy in a single electromagnetic calorimeter tower, while a hadronic shower continues into the hadronic section of the calorimeter and into the adjacent calorimeter towers. In addition to certain shower properties, for electrons the momentum of the track pointing to the shower should match the energy in the calorimeter.

### 3.1.1 Central Electrons

Central electron candidates traverse the central part of the detector, $|\eta| < 1.1$, leaving the track in the COT and depositing most of their energies in the CEM calorimeter. The following variables and criteria are used to identify high-$p_T$ electrons:

- $E_T = E\ \sin\theta > 20$ GeV

  The transverse electromagnetic energy $E_T$ deposited by the electron candidate in the CEM cluster. It is given by the total electromagnetic energy of the electron cluster $E$ multiplied by $sin\theta$ of the COT track pointing to the seed tower of the cluster. An electron cluster is formed of a seed EM tower, where are added to the seed tower until the maximum cluster size is reached. The cluster at maximum has two towers in pseudorapidity and one tower azimuth. The energy $E$ is corrected for differences due to non-linearities and time-dependent changes.

- $p_T > 10$ GeV

  The transverse momentum by the COT track measured by its curvature in the magnetic field. Raw COT resolution is substantially improved by constraining the track to originate from the beam line. The *beam constrained* tracking introduces a $p_T$ curvature bias in data, which is removed by correcting the signed curvature $Q/p_T$, where $Q$ is the charge of the track:

$$\frac{Q}{p_T^{\mathrm{corr}}} = \frac{Q}{p_T} - 0.00037 - 0.0011 \times \sin(\phi + 0.28) \tag{3.1}$$

  Later in the text we refer to the $p_T$ of the COT track when beam constrained, $p_T^{\mathrm{corr}}$. This correction is applied only to data and not to simulation of events.

- $E_{\mathrm{had}}/E_{\mathrm{em}} < 0.055 + 0.00045 \times E_{\mathrm{total}}$

The ratio of the hadronic calorimeter (CHA) energy of the cluster $E_{\text{had}}$ to its electromagnetic energy $E_{\text{em}}$ (CEM). The value $E_{\text{had}}/E_{\text{em}}$ is scaled by a factor of 0.00045 multiplied by the total energy of the cluster $E_{total}$ to compensate for inefficiency of the cut at very high energies, as higher energy electrons have more leakage into the hadronic calorimeter.

- $E/P < 2$ is applied for electrons with $E_T < 199$ GeV or $\mathrm{p_T} < 50$ GeV.

  The ratio of the electromagnetic calorimeter energy $E$ to the COT track momentum $P$. During the passage through the material inside the COT inner radius the electron might radiate a photon ("external bremsstrahlung"). The photon is collinear with the electron and it generally deposits its energy in the same calorimeter tower, thus not much affecting the value of $E_T$, however the momentum $p_T$ measured in the COT after bremsstrahlung will be smaller. This causes a long tail in the $E/P$ distribution above 1.0.

- $L_{\text{shr}} < 0.2$,

  The lateral shower profile $L_{shr}$ is a measure of how well the lateral shower development matches that expected from the electromagnetic shower. This variable compares the energies of CEM calorimeter towers adjacent to the seed tower of the EM cluster with energies expected from the test beam electrons. It is defined as a sum over towers:

$$L_{shr} = 0.14 \sum_i \frac{E_i^{\text{measured}} - E_i^{\text{expected}}}{\sqrt{(0.14\sqrt{E})^2 + \sigma^2_{E_i^{\text{expected}}}}} \tag{3.2}$$

  where *measured* $E_i$ is a measured energy in the CEM tower i; $E^{expected}{}_i$ is an energy deposit in the $i$-th tower expected from the test beam electrons and $E$ is the energy of the EM cluster. $0.14\sqrt{E}$ represents the error on the energy measurement and $\sigma^2_{E_i^{expected}}$ is the uncertainty on the energy estimate. For a typical EM cluster $L_{shr}$ is a two-tower sum. Any extra particles accompanying the one responsible for the main EM shower will tend to add to the energy in adjacent tower and make $L_{shr}$ a large positive number.

- $-3.0$ cm $<$ Q$\Delta$x $<$ 1.5 cm; $|\Delta$z$|$ $<$ 3 cm

  The distance $\Delta x$ / ($|\Delta z|$) in the $r$-$\phi/(r-z)$ plane between the COT track extrapolated to the CES and the best matching CES cluster. The cut on $\Delta x$ has been multiplied by the charge Q of the electron and it is asymmetric in $r-\phi$ to account for energy of the photon emitted in bremsstrahlung radiation. This requirement on a tight match between the track and shower position removes a large number of fake electron due to the coincidence of charged and neutral hadrons in the same tower, mainly due to $\pi^0$ and $\pi^\pm$ results in a reconstructed track that matches the electromagnetic cluster.

- $\chi^2_{\mathrm{strip}} < 10$

  The $\chi^2$ comparison of the CES shower profile in the $r-z$ view with the shower profile extracted form test beam electrons. The $\chi^2$-fit is performed on the distribution of energy deposited on each of the 11 strips in the CES shower.

- $|z_{\mathrm{vertex}}| < 60$ cm

  The interaction position in $z$, $z_{vertex}$, is taken from $z_0$, the $z$ intersection of the track with the beam axis in the $r-z$ plane. The longitudinal spread of the event vertex about the nominal interaction pint $z=0$ is a Gaussian with $\sigma = 26$ cm. The vertex position is required to be within 2 $\sigma$.

- Track quality cuts

  To insure that the track associated with electron is well reconstructed, it must pass through two axial and three stereo superlayers (SL) of COT with at least 7 hits out of 12 in each SL.

- Fiduciality

  This variable insures that the electron is reconstructed in a region of the detector that is well instrumented. The electron position in the CEM is determined by the CES shower position and it must satisfy the following requirement.

  - the electron must lie with 21 cm of the tower center in the $r-\phi$ view, so that the shower is fully contained in the active region, this corresponds to the cut $|x_{CES}| < 21\ cm$, where the $x_{CES}$ is the local coordinate of the calorimeter tower.
  - the region $|x_{CES}| < 9$ cm, where the two halves of the central calorimeter meet is excluded, as well as the region $|z_{CES}| > 230\ /rmcm$, which corresponds to the outer half of the CEM tower (tower9), as it is more subjected to the leakage into the hadronic part of the calorimeter.

– the region immediately close to the point of penetration of the cryogenic connections to the solenoidal magnet, the chimney, is un-instrumented and therefore excluded. It corresponds to $0.77 < \eta < 1.0$, $75^\circ < \phi < 90^\circ$ and $|z_{CES}| > 193$ cm.
– the region $1.05 < |\eta| < 1.10$ is excluded due to the smaller depth of the electromagnetic calorimeter.

- Not a conversion

  Photons produced either directly in the hard scattering or from hadron decays interact with the material in the detector and convert to electron-positron paris. These photon conversion can be identified by the presence of another track of the opposite sign near the electron candidate. If the two tracks exhibit small $r - \phi$ separation in the pint of conversion $|\Delta XY| < 0.2$ cm, and the difference in their polar angle $|\Delta \cot \phi| < 0.04$, the electron candidate is flagged as a conversion and the whole event is rejected.

- Isolation $= E_T^{\text{iso}}/E_T^{\text{cluster}} < 0.1$.

  where $E_T^{\text{iso}} = E_T^{0.4} - E_T^{\text{cluster}}$ is the transverse energy $E_T^{0.4}$ in a cone of radius $\Delta R = \sqrt{(\Delta\eta)^2 + (\Delta\phi)^2} \leq 0.4$ around the electron cluster (hadronic + electromagnetic) excluding the electron cluster energy $E_T^{\text{cluster}}$. This cut in fact is not an electron identification requirement. It rejects the electrons that are not isolated from extra hadronic activity and could be the products of quark semi-leptonic decays, while electrons from W and Z decays are expected to be isolated. We therefore consider both categories of isolated and non-isolated electrons in the event selection.

  The isolation is corrected for leakage energy into the neighboring $\phi$ wedge outside of the cone, which increases towards the edges of the $\phi$ wedges. The respective correction factor is determined form Monte Carlo data comparison and parametrized the form:

$$E_{\text{leak}} = E_T^{\text{cluster}} \cdot P_0 \cdot \exp P_1 \cdot (|x_{CES}| - 21) \tag{3.3}$$

where $P_0 = 0.0511 \pm 0.0075$ and $P_1 = 0.33 \pm 0.061$. If additional interactions occur in the same bunch crossing the energy in a cone is increased. Therefore isolation is also corrected for the number of interactions par bunch-crossing, the efficiency of the cut then becomes independent of the instantaneous luminosity. This correction factor is determined similarly to jet multiple interaction energy correction.

The corrected isolation energy is then

$$E_T^{\text{corr}} = E_T^{\text{iso}} - E_{\text{leak}} - E_{\text{MI}} \tag{3.4}$$

and corrected isolation is given by

$$Iso_{\text{corr}} = E_T^{\text{corr}} / E_T^{\text{cluster}} \tag{3.5}$$

Central electron ID efficiency was determined from the $Z \rightarrow e^+e^-$ events were selected as dilepton events of opposite charge falling into Z mass window, 75 GeV $<$ $\mathrm{M_{ee}}$ $<$ 105 GeV. The number of observed same-sign dielectron event's is the same Z mass range served as an estimate of QCD background contamination. At least one electron was required to be tight, i.e. passing all identification cut.

### 3.1.2 Plug Electrons

Electron candidates deposition their energies in the PEM calorimeter are referred to as *plug electrons*. We impose the following identification criteria to define plug electron candidates:

- $1.2 < |\eta| < 2.0$

  Although plug electron can be identified up to $|\eta| < 2.5$, this analysis considers only those with $|\eta| < 2.0$, primarily due to large charge misidentification rate at high pseudorapidities $\eta$. This cut has a small effect on the $t\bar{t}$ acceptance, as final products of $t\bar{t}$ decay events are mostly central and the acceptance falls rapidly at large $\eta$, while backgrounds considerably increase. The low $\eta$-region $|\eta| < 1.2$ is excluded due to geometrical reasons since the PES detector does not provide usable coverage there. The track information from the COT is unavailable in the forward region of the detector, as plug electrons do not traverse the active volume of the COT. Plug electron candidates identified based only on the presence of an EM cluster in the PEM calorimeter, i.e. with no track requirements, are called *PEM electrons*. PEM electron candidates do not provide charge sign information and are subject to a large fake rate.

  To reduce the misidentification rate the track reconstruction for plug electrons is performed by utilizing the silicon layer (ISL) residing in the forward part of the detector and providing usable coverage in $1.2 < |\eta| < 1.8$ rage. The silicon pattern recognition code extrapolates the hits in the outer layers to the inner layers of silicon and determines the location of the primary vertex. The tracking efficiency for tracks pointing to the plug region is considerably lower than for the central part of the detector. It is improved by a special algorithm, called *phoenix algorithm.* the Phoenix algorithm makes use of the information of the PES position of an EM shower. It constraints the track at two endpoints, one is fixed at the interaction vertex and the other is at the PES position of an EM shower. Adoption the corresponding PEM cluster energy as the momentum of the electron, a helix of the track can be determined. This defines two possible track trajectories, one is for negative and the other is for positive charge. The silicon pattern recognition code further attempts to reconstruct those tracks by matching hits in the layers of silicon. If one of these tracks is reconstructed, it is appended to the event record as being associated with the respective electron candidate. If both tracks are reconstructed then the algorithm performs the $\chi^2$-fit of a possible electron trajectory and adopts the track best matching the activity in the silicon detector. Such a track is call a *Phoenix plug electron*, abbreviated as PHX.

The Phoenix algorithm establishes charge identification for plug electron candidates beyond the coverage of the forward silicon layers up to $|\eta| < 2.0$.

- $E_T > 20$ GeV

  Unlike the CEM clusters, the PEM clusters are limited to $2\times2$-two towers in pseudorapidity by two towers in azimuth.

- $E_{\rm had}/E_{\rm em} < 0.05$

  Similar to the central electrons, the ratio of the hadronic calorimeter (PHA) energy of the cluster $E_{\rm had}$ to its electromagnetic energy $E_{\rm em}$ (PEM).

- $U_{5\times9} \geq 0.65$ and $V_{5\times9} \geq 0.6$ The quantities $U_{5\times9}$ and $V_{5\times9}$ are essentially isolation variables for the shower maximum detector independently applied to both the U and V layers.The PES clustering is performed by ordering PES strips in decreasing energy with the highest-energy strips used as seeds. Then a fixed-width nine-strip cluster is formed from each seed. This is done separately for 1D U- and V- layer clusters. The quantities $U_{5\times9}$ and $V_{5\times9}$ represent the ratios of energy sum in the central 5 strips of a PES cluster to the total energy of the PES cluster (in all 9 strips).

- $\chi^2_{3\times3} < 10$

This variable represents the goodness of $\chi^2 - fit$ measure of the energy distribution in 3×3 towers around the seed tower to energy distributions from test beam electrons.

- $|\Delta R_{PES}| < 3$ cm

  The $\chi^2 - fit$ also determines the position for the center of the shower. $\Delta R_{PES} = \sqrt{(\Delta\eta)^2 + (\Delta\phi)^2}$ is the distance between the $\chi^2)3 \times 3$ best fit position and the intersection of the centroids in the U- and V-layer PES clusters. $\Delta R$ matching requirement is also enforced between the PES coordinates and the extrapolated Phoenix track.

- $N_{\text{hits}}^{\text{Si}} \geq 3$

  Number of Silicon hits $N_{\text{hits}}^{\text{Si}}$. This requirement is enforced to improve the quality of the silicon tracks at the cost of some efficiency.

- $|z_0| < 60$

  This cut is identical to the CEM electrons.

- Isolation $= E_T^{\text{iso}}/E_T^{\text{cluster}} < 0.1$

  This variable is defined identically to the CEM electrons. The corrections to $E_T^{\text{iso}}$ are done differently, however, as the clustering algorithm in the plug region differs from the one in the central region. The leakage energy is parametrized depending on the distance of the tower form the center of the electron shower in $\theta$ and $\phi$.

Plug electron ID efficiency was determined from the $Z \to e^+e^-$ data sample, similar to how it was done for central electrons. $Z \to e^+e^-$ events were selected as central-plug dielectron events in the Z mass range. The central electron was required to be a good electron, i.e. pass all tight identification criteria, and the other leg was required to be an EM object fiducial to the plug region. Plug electron ID efficiency was determined as the ratio of tight-tight (central-plug) candidates over tight-loose candidates.

## 3.2 Muon Identification

Muons are minimum-ionizing particles which penetrate matter very easily. Muons resulting from the dilepton channel of the $t\bar{t}$ decay, as well as electrons, are very energetic. They are identified by the high-$p_T$ track in COT, very little energy deposition in the calorimeters, and matching hits in the muon chambers. A muon candidate is required to have aligned hits in both $r - \phi$

and $r - z$ planes on at least 3 separate layers. These hits form a muon stub which is then matched to the COT tracks extrapolated to the muon chambers.

Muons are categorized by the detector region through which they pass. Muons reconstructed in both the CMU and CMP chambers are called CMUP muons. Due to the gaps in the muon chambers coverage there are also muon that are reconstructed only in the CMU or the CMP muon chambers. These muons are called CMU, CMP respectively. Muons with stubs in the CMX chamber are called CMX muons. The COT tracks with no muon stubs are also considered as muon candidates. Such muons are required to have minimum energy depositions in the calorimeter. These muon candidates are called CMIO's (central minimum ionizing objects). The following criteria are applied for muon candidates:

- $p_T > 20$ GeV

  The transverse momentum of the COT track. The track is beam constrained and $p_T$ corrections are applied identically as it is done for electrons.

- $|z_0| < 60$ cm

  As for electrons, the $z$-position of the muon track is associated with the event vertex and required to be within 60 cm from the geometrical center of the detector.

- $d_0 < 0.2$ cm for tracks with no silicon hits.; $d_0 < 0.02$ cm for tracks with silicon hits.

  The impact parameter $d_0$ is the distance between the reconstructed muon track and the beam axis in the $r - \phi$ plane. Unlike others this selection variable is based on the default muon track, not beam-constrained, and a trigger cut is applied if the track contains silicon hits. This cut forces the muon to originate from the nominal interaction region and substantially reduces the cosmic muon background. It also helps to remove muons from kaons and pions that decay in flight.

- Track quality cuts

  Track quality cuts are identical to electron track quality cuts. The track is required to have at least 7 COT hits on at least 2 axial and 3 stereo superlayers.

- $E_{\rm em} \leq 2 + max(0, 0.0115(P - 100))$ GeV

The energy deposited in the electromagnetic calorimeter. High $p_T$ muons are not expected to deposit substantial amount of energy in the electromagnetic calorimeter. the sliding cut is introduced for muons with $P < 100 GeV$ to increase efficiency of the cut.

- $E_{\rm had} \leq 6 + \max(0, 0.0280(P - 100))$ GeV

  The energy deposited in the hadronic calorimeter is higher, but still quite small in comparison to strongly interacting jets.

- $E_{\rm em} + E_{\rm had} > 0.1\ /rm GeV$ for stubless muon only.

  Stubless muons are required to have a non-zero energy deposition in the calorimeter to limit backgrounds from electrons escaping the detector through cracks in the calorimeter.

- $|\Delta x|_{\rm CMU} \leq 7$ cm

  The distance in the $r-\phi$ plane between the extrapolated COT track and the stub segment in the relevant muon chamber. The muon candidate passing this requirement falls into CMUP or CMU category.

- $|\Delta x|_{\rm CMP} \leq 5$ cm

  Muons in the CMP and CMX detector traverse more material than in the CMU and experience grater deflections due to multiple scattering. Therefore, the track-to-stub matching cut are looser. This muon candidate falls into CMUP or CMP category.

- $|\Delta x|_{\rm CMX} \leq 6$ cm

  CMX muon category requirement.

- $\rho_{\rm COT} > 140$ cm

  The COT exit radius

  $$\rho_{\rm COT} = \frac{\mathrm{sign}(\eta) \cdot z_{\rm COT} - z_0}{\cot(\theta)} \tag{3.6}$$

  is based on pseudorapidity $\eta$ and $z_0$ of the track, where $z_{COT} = 155$ cm is the length of the COT and $\theta$ is the polar angle.

  This cut is enforced only for CMX muons to eliminate the data bias due to the XFT trigger requirement that a track must leave hits in at least four COT superlayers.

- Isolation $= E_T^{\mathrm{iso}}/p_T < 0.1$

  where $E_T^{\mathrm{iso}} = E_T^{\mathrm{cone}} - E_T^{\mathrm{tower}}$ is the difference between energy in the cone of $\Delta R = 0.4$ around the muon track $E_T^{\mathrm{cone}}$ and the amount of energy in the tower associated with the muon track $E_T^{\mathrm{tower}}$.

- not-cosmic

  Cosmic ray can be identified in the CDF detector as dimuon events leaving a nearly straight track and therefore mimickintg a very energetic $\mu^+\mu^-$ pair. Since cosmic rays do not originate from a *ppbar* collision and enter the detector at random locations, this background is reduced by a cut on the track impact parameter $d_0$. In addition, cosmic rays appear randomly in time and can be distinguished by substantial time delay between the hits of the two muons in the hadronic calorimeter, measured by Time to Digital Converter (TDC), and by using timing information from the Time of Flight detector (TOF). All of this information is analyzed by the software code, named Cosmic Ray Tagger, which makes a decision on flagging an event as a cosmic. Events with muon identified as cosmics are rejected.

The muon ID efficiencies are measured using Z boson decays $Z \to \mu\mu$ similarly to electrons. Both legs are linked to a CMUP or CMX muon stub, where one leg is required to pass tight identification criteria and is matched to Level-1 trigger information, while the second leg is chosen to be fiducial to the tested detector region (e.g. CMUP, CMX), or non-fiducial to any (for stubless CMIO muons) and examined if it passed muon ID cuts thus being independent of a trigger requirement.

## 3.3 Jet Reconstruction

At high energies, as those achieved in Tevatron, jets are the dominant feature of hadron production. They result from point-like collisions of a quark or gluon from the proton with a quark or gluon from the antiproton. A jet is formed from a scattered initiating parton, which experiences fragmentation leading to the creation of a stream of energetic colorless particles emitted spatially collimated along the original parton direction.

The jets are observed as cluster of energy located in adjacent detector towers. Typically a jet contains neutral or charged pions to a lesser extent of kaons, and about 10 % of light baryons such as protons and neutrons. Pions mostly deposit their energies in electromagnetic calorimeter, while kaon and baryons leave most of their energies in the hadronic section of the calorimeter. The energy of the initial parton can be approximated by summing the tower energies within a cone of specified size. This procedure is called *jetclustering*. The cone size is chosen to encompass most of the jet energy without allowing a significant contribution from other event activity. It is defined in $\eta - \phi$ space by its radius, $R = \sqrt{\Delta\eta^2 + \Delta\phi^2}$ and is centered at the largest calorimeter energy tower serving as a seed tower of the jet cluster. This analysis is using a cone size of $\Delta R = 0.4$.

After the jet cluster is thus formed, the $E_T$ weighted centroid of the cluster is determined, as follows

$$\eta_{\text{centroid}} = \frac{\sum_{i=1}^{N} E_T^i \eta^i}{\sum_{i=1}^{N} E_T^i} \tag{3.7}$$

$$\phi_{\text{centroid}} = \frac{\sum_{i=1}^{N} E_T^i \phi^i}{\sum_{i=1}^{N} E_T^i} \tag{3.8}$$

where the sums are carried out over all calorimeter towers in the cluster. It defined the centroid tower and a new cone drawn around this position. This process is iterated until the cluster remains unchanged in two consecutive paths. In some cases two clusters can overlap and then they are either merged into one, if the sum of the energies in shared towers exceed 75 % of the energy of the smaller cluster, or left intact.

The jet four-momentum $(E^{\text{raw}}, p_x^{\text{raw}}, p_y^{\text{raw}}, p_z^{\text{raw}})$ is then determined by the following sums over the cluster towers:

$$E^{\text{raw}} = \sum_{i=0}^{N} E_i \tag{3.9}$$

$$p_x^{\text{raw}} = \sum_{i=0}^{N} E_i \sin\theta_i \cos\phi_i \tag{3.10}$$

$$p_y^{\text{raw}} = \sum_{i=0}^{N} E_i \sin\theta_i \sin\phi_i \tag{3.11}$$

$$p_z^{\text{raw}} = \sum_{i=0}^{N} E_i \cos\phi_i \tag{3.12}$$

These quantities are referred to as raw, since they are affected by mismeasurements for a variety of reasons due to both to physics and to detector effects and are different from the true energies of the partons which initiated jets. Therefore proper corrections need to be applied to reconstruct true momentums of partons.

### 3.3.1 Jet Energy Corrections

The measured four-vector of jets generally differs from the energies of the initial partons. This is the result from both instrumental and physical effects such as low energy non-linearities, $\eta$ crack energy losses, underlying events, and clustering. Some of the corrections are decided by the measurable quantities independent of the theory, while some of them rely on the theory prediction. Thus the row jet energies measured in the calorimeter must be corrected for detector effects at first before they can be compared to physics predictions/models. The correction strategy is the followings:

- Relative Corrections

  The first step in jet energy corrections is to correct the jets for any variation in the response with detector $\eta$. For this correction, dijet event samples are used. Since the transverse energy of the two jets in a $2 \rightarrow 2$ process should be equal, the energies of jets in the plug and forward calorimeters are scaled to give the energy of an equivalent jet in the central calorimeter. One well-measured central jet ($0.2 < |\eta| < 0.6$) is required and a scale factor is derived from the dijet balance to the second jet. The central calorimeters CEM/CHA are the best understood calorimeters in CDF and the selected region is far away from the cracks. The gain variation depending on the time (run range) in the plug calorimeters is also taken into account. The corrections for the Monte Carlo and data are determined separately since some discrepancy between data and simulation can be seen due to a lack of the materials in the detector simulation.

- Multiple Interaction Corrections

  The multiple interaction affects the measured jet energy when the energy from these minimum bias events falls into the jet clustering cone. The transverse energy in a random cone is measured in minimum bias data and parameterized as a function of the number of vertices in the event. This transverse energy is subtracted from each jet to account for multiple interaction in the same bunch crossing as a function of the number of vertices in the event. This correction factor is a linear function of the number of reconstructed vertices in the event. Only vertices associated with at least 2 COT tracks in minimum bias events are used to decide this correction factor.

- Absolute Corrections

  The jet energy measured by the calorimeters must be corrected for any non-linearity and energy loss in the un-instrumented regions of each calorimeter. The absolute jet corrections account for the response to particle-level energy in the central calorimeter. This correction depends on the jet fragmentation properties. The calibration point is derived using a 50 GeV pion from test beam data. For the non-linearity response, the tuned Monte Carlo events are used for the charged and neutral particles. After fragmentation, the events are processed with a full CDF detector simulation. Each simulated event is compared to the total $p_T$ of all generated particles lying in a cone centered about the measured jet axis. A quadratic spline fit is used to parameterize the mean jet response as a function of $E_T$ for the each cone size.

- Underlying Event Corrections

  The underlying event contains all the soft interactions except the hard one. The underlying event energies must be subtracted from the measured jet energy when these particles fall into the clustering cone. The correction procedure is the same as the multiple interaction correction. Events with only one vertex are used to determine the underlying event correction.

- Out-of-Cone Corrections

  The jet clustering may not include all the energy from the initiating parton. Some of the partons generated during fragmentation may fall outside the cone chosen for clustering algorithm. Out-of-cone corrections are applied in order to correct the particle-level jet energy to the parton energy (as much as theoretically allowed). These corrections are completely independent of detector/calorimeter performance and depend on the parton fragmentation functions. The correction factor is parameterized as a function of jet $p_T$. Jet tends to become narrower at large energies, and the fractional energy deposited outside the cone decreases.

Thus, the jet energy is corrected by

$$p_T(R) = [p_T^{\text{raw}}(R) \times f_{\text{rel}} - \text{UEM}(R)] \times f_{\text{abs}}(R) - \text{UE}(R) + \text{OC}(R), \quad (3.13)$$

where $R$ denotes the clustering cone size, $p_T$ and $p_T^{\text{raw}}$ are the corrected and row transverse momenta of jet, $f_{\text{rel}}$ is the relative jet energy correction, UEM$(R)$ is the multiple interactions correction, $f_{\text{abs}}(R)$ is the absolute jet energy correction, UE$(R)$ is the underlying event correction, and OC$(R)$ is the out-of-cone correction.

### 3.3.2 Jet Energy Scale Uncertainties

The differences between the data and CDF simulations of the jet responses are treated as the systematic uncertainties of the jet energy scale (JES) [47]. The uncertainties are estimated for each type of jet energy corrections. The uncertainties due to the absolute scale and the jet shape (out-of-cone) are dominant. The main systematic uncertainties on the absolute scale are obtained by propagating the uncertainties on the single particle response ($E/p$) and the fragmentation. Smaller contributions are from the calorimeter response close to tower boundaries in azimuth, and from the stability of the calorimeter calibration with time. The uncertainties from the jet shape are estimated by measuring the energy flow between cones of size 0.4 and 1.3 in both data and MC simulations. The total JES uncertainties in the central region are shown in Figure 3.1.

## 3.4 Missing Energy

Neutrinos interact only through weak interactions and therefore cannot be directly detected as they traverse the detector material. Production of neutrinos in an event can be spotted by the existence of the large imbalance in the calorimeter energy. The longitudinal component of the colliding partons is not known, but the transverse component is subject to conservation, and the sum of the transverse components of the neutrino momenta can be measured. This quantity is called missing transverse energy $\vec{\not\!\!E}_T$. The missing transverse energy is two-component vector $(\not\!\!E_{T_x} \not\!\!E_{T_y})$. The raw value of $\vec{\not\!\!E}_T$ is defined by the negative vector sum of the transverse energy of all calorimeter towers:

$$\vec{\not\!\!E}_T^{\text{raw}} = -\sum_{\text{tower}} (E_i \sin\theta_i)\vec{n}_i \quad (3.14)$$

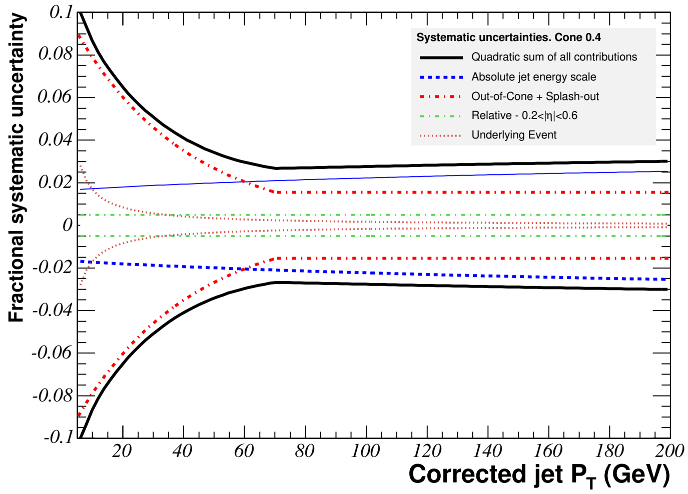


Figure 3.1: The total uncertainties of JES as a function of corrected jet $p_T$ in the central calorimeter ($0.2 < |\eta| < 0.6$).

where $E_i$ is the energy of the $i$-th tower, $\vec{n}_i$ is a transverse unit vector pointing to the center of the tower and $\theta_i$ is the polar angle of the line pointing from $z_0$, $z$-coordinate of the event vertex, to the $i$-th tower. This sum extends to $|\eta_{detector}| < 3.6$.

The value of $\vec{\not\!\!E}_T^{\text{raw}}$ should be further corrected for escaping muons and jet energy mismeasurements. Muons do not deposit substantial energy in the calorimeter, but may carry out significant amount of the energy. The sum of transverse momenta of escaping muons $\sum \vec{P}_{T,\mu}$ measured in the COT has to be added to the $\vec{\not\!\!E}_T^{\text{raw}}$ with a negative sign and the energy deposited by muons in the calorimeters $\sum \vec{E}_{T,\mu}$ has to be subtracted from that sum, as it has been already counted in the $\vec{\not\!\!E}_T^{\text{raw}}$.

Only raw values of jet energies contribute to the $\vec{\not\!\!E}_T^{\text{raw}}$ and these values have to be replaced in the sum by the corrected ones. The corrected value of $\vec{\not\!\!E}_T^{\text{corr}}$ is therefore given by the following relation:

$$\vec{\not\!\!E}_T^{\text{corr}} = \vec{\not\!\!E}_T^{\text{corr}} - \left( \sum_{\text{muons}} \vec{P}_{T,\mu} - \sum_{\text{muons}} \vec{E}_{T,\mu} \right) - \left( \sum_{\text{jet}} \vec{E}_{T,jet}^{\text{corr}} - \sum_{\text{jet}} \vec{E}_{T,\text{jet}}^{\text{raw}} \right) \quad (3.15)$$

Uncertainties in $\vec{\not\!\!E}_T^{\text{corr}}$ are dominated by uncertainties in jet energies. Mismeasurements of $\not\!\!E_T$ result from jets traversing through poorly instrumented regions of detectors, e.g. cracks, dead zones, and beam halo effects. They may also result from cosmic rays, muon misidentification and mismeasurements in muon track momenta.

The resolution of the $\not{E}_T$ generally depends on the response of the calorimeter to the total energy deposited in the event. It is parameterized in terms of the total scalar transverse energy $\sum \not{E}_T$, which is defined as

$$\sum \not{E}_T = \sum_{\text{towers}} E_i \sin\theta_i \tag{3.16}$$

The $\not{E}_T$ resolution in the data is measured with minimum bias events, dominated by inelastic $p\bar{p}$ collisions. In minimum bias events the $x$ and $y$ components of $\vec{\not{E}_T}$ are distributed as Gaussian around zero with $\sigma_x = \sigma_y = \sigma$:

$$\frac{dN}{d\not{E}_{T_x,y}} \simeq \exp\left(-\frac{\not{E}^2_{T_x,y}}{2\sigma^2}\right) \tag{3.17}$$

The $\not{E}_T$ resolution $\Delta = \sqrt{\langle \not{E}^2_T \rangle}$ is then given by $\Delta = \sqrt{2}\sigma_{x,y}$. It is expected to scale as a square root of the total transverse energy in the event, $\sum E_T$, is determined to be $\Delta \simeq 0.64\sqrt{\sum E_T}$ from minimum bias studies.

# Chapter 4

# Measurement of the Top-quark Pair Production Cross Section

In this chapter, the measurements of the top quark pair production cross section ($\sigma(p\bar{p} \to t\bar{t}X)$) in the dilepton channel are described. The production cross section is calculated from the following formula:

$$\sigma(p\bar{p} \to t\bar{t}X) = \frac{N_{\text{obs}} - N_{\text{bkg}}}{\mathcal{A} \times \mathcal{L}}, \tag{4.1}$$

where $N_{\text{obs}}$ is the number of events in data passing event selection, $N_{\text{bkg}}$ is the number of non-$t\bar{t}$ events expected to pass event selection, $\mathcal{A}$ is $t\bar{t}$ acceptance (geometric acceptance and event selection efficiency), and $\mathcal{L}$ is the integrated luminosity of the data.

## 4.1 Samples

The results presented are obtained by using the data collected with the CDF detector from December 2004 to May 2007 (2 $\text{fb}^{-1}$).

The data are collected either via the central high $\text{p}_T$ electron or muon trigger paths. For this analysis we ignore events triggered by a plug electron plus missing energy as they contributed only a small percentage of the total acceptance ($\sim 4.5\%$) and required an ad-hoc treatment of the trigger efficiency.

The cross sections for SM processes that we consider as backgrounds and which can be simulated in a MC are given in Table 4.1. The main $t\bar{t}$ signal MC sample is the 4.8 M events of inclusive `Pythia`[48] sample generated at $\text{M}_{\text{top}} = 175$ GeV. To model the main sources of Standard Model backgrounds to the top dilepton channel we use:

Table 4.1: Cross Sections for different Standard Model processes considered as background to the top dilepton selection. The final NLO cross section are either already quote here as $\sigma$ or obtained multiplying the $\sigma$ in the first column by the K-factor in the second column.

| Process | Cross Section $\sigma$ (pb) | K-factor |
|---|---|---|
| Z$\rightarrow$ $ee/\mu\mu$ | 355$\pm$3 | 1.4 |
| Z$\rightarrow$ $\tau\tau$ | 238$\pm$3 | 1.4 |
| WW | 12.4$\pm$0.8 | NA |
| WZ | 3.7$\pm$0.1 | NA |
| ZZ | 3.8$\pm$0.8 | NA |
| W$\gamma$ | 32$\pm$3.2 | 1.36 |

- `Alpgen` $Z(ee)$ `sample` for Z $\rightarrow ee$
- `Alpgen` $Z(\mu\mu)$ `sample` for $Z \rightarrow \mu\mu$
- `Alpgen` $Z(\tau\tau)$ `sample` for $Z \rightarrow \tau\tau$
- `PYTHIA diboson sample` for $WW/WZ/ZZ$ diboson events
- `Baur` W$\gamma$ `sample` for $W\gamma$, $W \rightarrow e\nu/W \rightarrow \mu\nu$ events

Diboson backgrounds are generated with PYTHIA, The W$\gamma$ samples are generated with the Baur Monte Carlo. To keep good statistics, the Z sample are generated with the Alpgen [49] Monte Carlo. The matrix element generator Alpgen can generate Z+parton sample. Thus Alpgen generator is efficient for especially these rare events, our background from Z have at least two jet. The ZZ events are generated with M$_{\ell\ell}$ > 2 GeV. Their cross section is obtained by multiplying a NLO MCFM calculation for M$_{\ell\ell}$ > 15 GeV of 2.1 pb by the fraction of events found with M$_{\ell\ell}$ < 15 GeV over the total. A 20% uncertainty is assumed for $\sigma(ZZ)$ given the uncertainty of the extrapolation method. Table 4.1 summarizes the NLO cross sections assumed for each MC sample.

The calculation of events with one jet/track faking a lepton uses fake lepton identification rates extracted from the JET50 inclusive jet samples that is triggered by 50 GeV jet. Fake rates from the JET20, JET70 and JET100 samples, each jet sample triggered by 20, 70, 100 GeV jet respectively, are used to access the systematic uncertainty on the fake estimates.

## 4.2 Top dilepton (DIL) event selection

DIL selection aims at reconstructing $t\bar{t}$ events with both W's from top decaying leptonically. It requires two fully identified electrons or muons with transverse energy above 20 GeV, $\not\!\!E_T > 25$ GeV and at least two tight jets of $E_T > 15$ GeV. The first, or trigger lepton can be one of three types: CEM electron, CMUP or CMX muon. The second, or loose lepton, can be also non-isolated or an isolated PHX electron or one of the non-trigger muon types: CMU-only, CMP-only and CMIO. Details on the cuts used to identify each lepton category are contained in Section 3. Non isolated counterpart of the trigger leptons (i.e. NICEM electrons and NICMUP/NICMX muons) are allowed to trigger the event when they come together with a PHX electron to recover most of the acceptance lost by dropping the plug electron dataset.

The jets are corrected up to hadron level (i.e. we don't apply Underlying Events and Out-of-Cone Correction, jet is called parton level after these correction). We should mention here that for the purpose of correcting $\not\!\!E_T$ (which is calculated starting from the raw transverse energy deposited in each tower of the calorimeter), we used the jet energy scale calculated ignoring the Multiple Interaction correction order to avoid over-correcting $\not\!\!E_T$ for the presence of energy due to extra interactions.

Extra event topology cuts are imposed to improve the purity of the selection:

- Z-veto for $ee$ and $\mu\mu$ events with reconstructed dilepton invariant mass in the 76-106 GeV window. See details below.
- L-cut in the ($\not\!\!E_T$ , $\delta\phi_{min}$) plane to reject Z$\rightarrow \tau\tau$ events and events with mis-measured $\not\!\!E_T$ from jets pointing to cracks in the calorimeter: this cut requires the event $\not\!\!E_T$ to be above 50 GeV is there is any lepton or jet inside 20° of the $\not\!\!E_T$ direction.
- $H_T > 200$ GeV cut to suppress events from an initial state lighter that $t\bar{t}$
- opposite charge for the two leptons.

We defined MET Significance as:

$$\text{MetSig} = \frac{\not\!\!E_T}{\sqrt{E_T^{sum}}} \tag{4.2}$$

where $E_T^{sum}$ is the sum of transverse raw energies deposited in all calorimeter towers, corrected for any muon $p_T$ and for the difference between the raw and the corrected energy of tight jets in the event. We find that a cut on $MetSig > 4\sqrt{\mathrm{GeV}}$ reduce the background by $\sim 25\%$, mostly in the Drell-Yan channel.

## 4.3 Cross Section Denominator

The denominator of the cross section calculation can be written as an acceptance times the luminosity (see Eq. (4.1)). The acceptance itself is the convolution of the MC acceptance and of different correction factors estimated from comparing the efficiency predicted by MC and data in independent control samples. For the DIL selection we choose to compute the denominator as:

$$\begin{aligned} \mathcal{A} \times \mathcal{L} &= \sum_i \mathcal{A}_i \times \mathcal{L}_i \\ \mathcal{A}_i &= \mathcal{A}_{\ell_1\ell_2} \times C_{\ell_1\ell_2} \end{aligned} \tag{4.3}$$

where the index $i$ run over all of the DIL selection categories, each made of a pair of leptons, $\ell_1\ell_2$. The PYTHIA $t\bar{t}$ MC raw efficiencies efficiencies $A_{\ell_1\ell_2}$, calculated as the ratio of the number of dilepton events passing the DIL selection in the $t\bar{t}$ MC sample, are multiplied by the dilepton correction factors $C_{\ell_1\ell_2}$ and by the luminosities $\mathcal{L}_i$ appropriate for each lepton pair.

The dilepton correction factors $C_{\ell_1\ell_2}$ are calculated using the following factorization.

$$C_{\ell_1\ell_2} = \epsilon_{z_0} \times (\epsilon_{trg_1} + \epsilon_{trg_2} - \epsilon_{trg_1}\epsilon_{trg_2}) \times SF_1 SF_2 \tag{4.4}$$

where $\epsilon_{z_0}$ is efficiency of the cut imposed on all MC events to have the event vertex reconstructed inside a $\pm 60$ cm region from the nominal z=0; $\epsilon_{trg_i}$ are the trigger efficiencies for the two leptons; $SF_i$ are the identification scale factor, measured as the ratios of the data over the MC lepton identification and muon reconstruction efficiencies.

The trigger efficiencies and identification scale factors for each single lepton in the dilepton pair are reported in Table 4.2. The efficiency of the event for the primary vertex $|z_{VTX}| < 60$ cm cut is also reported in Table 4.2.

Table 4.3 details all of the inputs to equation 4.3. Summing over all of the DIL categories, we obtain a denominator for the 2.0 fb$^{-1}$DIL cross section of $14.131 \pm 0.076$ pb$^{-1}$, where the uncertainty comes solely from the propagation of the uncertainties of each term in equation 4.4.

Table 4.2: List by lepton type of vertex reconstruction efficiency $\epsilon_{z_0}$, trigger efficiency $\epsilon_{trg}$, and lepton identification scale factors $SF$. The electron trigger efficiency uncertainties have a 0.3% systematic error added in quadrature. For lepton types labeled with a (NI), we don't distinguish between isolated and non isolated leptons.

| Lepton type | Vertex Reconstruction efficiency $\epsilon_{z_0}$ (2fb$^{-1}$) |
|---|---|
| | 0.9637 ±0.0007 |
| **Lepton type** | **Trigger efficiency $\epsilon_{trg}$ (2fb$^{-1}$)** |
| CEM | 0.9670±0.0019 |
| CMUP | 0.9171±0.0020 |
| CMX | 0.8664±0.0045 |
| **Lepton type** | **Lepton Identification Scale Factor $SF$ (2fb$^{-1}$)** |
| CEM | 0.9789 ±0.0018 |
| (NI)CEM | 0.9854 ±0.0015 |
| PHX | 0.9318 ±0.0028 |
| CMUP | 0.9272±0.0027 |
| (NI)CMUP | 0.9325±0.0025 |
| CMX | 0.9747±0.0089 |
| (NI)CMX | 0.9782±0.0026 |
| CMU | 0.9281±0.0052 |
| (NI)CMU | 0.9348±0.0049 |
| CMP | 0.9486±0.0038 |
| (NI)CMP | 0.9515±0.0034 |
| CMIO | 1.0339±0.0041 |

### 4.3.1 Check of Acceptance Corrections

As a cross-check of our lepton selection, as well as the quoted luminosities, trigger efficiencies and scale factors used in final calculation of $t\bar{t}$ cross section, we measure the cross section of on-shell $Z$ production.

We select the events which have $ee$ or $\mu\mu$ pair in the final state. Cosmic events and events with an identifies conversions are removed. We required the two leptons to have opposite charges and invariant mass in the range 76 GeV/$c^2$ to 106 GeV/$c^2$.

The acceptance is calculated using Z $\rightarrow$ ee and $\mu\mu$ Monte Carlo samples. The MC acceptance is defined by the number of events which pass the selection described above, divided by the number of events in which invariant

Table 4.3: List, by dilepton category, of raw acceptance $\mathcal{A}_{\ell_1\ell_2}$, correction factor $C_{\ell_1\ell_2}$ and luminosity $\mathcal{L}_i$ used to calculate the denominator for the 2 fb$^{-1}$DIL cross section measurement. The raw acceptance uncertainty comes purely from the MC statistics. The error in the $C_{\ell_1\ell_2}$ comes from the propagation of the single lepton efficiency uncertainties reported in Table 4.1.

| Category | $\mathcal{A}_{\ell_1\ell_2}(\%)$ | $C_{\ell_1\ell_2}$ | $\mathcal{L}_i(\mathrm{pb}^{-1})$ |
|---|---|---|---|
| CEM-CEM | 0.1027 ± 0.0015 | 0.9225 ± 0.0035 | 2033.6 |
| CEM-NICEM | 0.0198 ± 0.0007 | 0.9286 ± 0.0023 | 2033.6 |
| PHX-CEM | 0.0430 ± 0.0010 | 0.8576 ± 0.0040 | 1916.0 |
| PHX-NICEM | 0.0041 ± 0.0003 | 0.8632 ± 0.0039 | 1916.0 |
| CMUP-CMUP | 0.0412 ± 0.0010 | 0.8228 ± 0.0048 | 2033.6 |
| CMUP-NICMUP | 0.0085 ± 0.0004 | 0.8275 ± 0.0033 | 2033.6 |
| CMUP-CMU | 0.0175 ± 0.0006 | 0.7606 ± 0.0052 | 2033.6 |
| CMUP-NICMU | 0.0016 ± 0.0002 | 0.7660 ± 0.0050 | 2033.6 |
| CMUP-CMP | 0.0236 ± 0.0007 | 0.7773 ± 0.0043 | 2033.6 |
| CMUP-NICMP | 0.0031 ± 0.0003 | 0.7797 ± 0.0040 | 2033.6 |
| CMUP-CMX | 0.0403 ± 0.0010 | 0.8613 ± 0.0036 | 1992.5 |
| CMUP-NICMX | 0.0038 ± 0.0003 | 0.8640 ± 0.0027 | 1992.5 |
| CMX-NICMUP | 0.0033 ± 0.0003 | 0.8761 ± 0.0019 | 1992.5 |
| CMUP-CMIO | 0.0231 ± 0.0007 | 0.8471 ± 0.0047 | 2033.6 |
| CMX-CMX | 0.0092 ± 0.0005 | 0.8992 ± 0.0054 | 1992.5 |
| CMX-NICMX | 0.0014 ± 0.0002 | 0.9024 ± 0.0038 | 1992.5 |
| CMX-CMU | 0.0067 ± 0.0004 | 0.7554 ± 0.0062 | 1992.5 |
| CMX-NICMU | 0.0009 ± 0.0001 | 0.7607 ± 0.0061 | 1992.5 |
| CMX-CMP | 0.0102 ± 0.0005 | 0.7720 ± 0.0056 | 1992.5 |
| CMX-NICMP | 0.0013 ± 0.0002 | 0.7743 ± 0.0054 | 1992.5 |
| CMX-CMIO | 0.0100 ± 0.0005 | 0.8413 ± 0.0061 | 1992.5 |
| CEM-CMUP | 0.1450 ± 0.0018 | 0.8723 ± 0.0031 | 2033.6 |
| CEM-NICMUP | 0.0183 ± 0.0006 | 0.8759 ± 0.0023 | 2033.6 |
| CMUP-NICEM | 0.0136 ± 0.0006 | 0.8823 ± 0.0026 | 2033.6 |
| CEM-CMU | 0.0312 ± 0.0008 | 0.8467 ± 0.0053 | 2033.6 |
| CEM-NICMU | 0.0037 ± 0.0003 | 0.8527 ± 0.0051 | 2033.6 |
| CEM-CMP | 0.0424 ± 0.0010 | 0.8653 ± 0.0042 | 2033.6 |
| CEM-NICMP | 0.0051 ± 0.0003 | 0.8679 ± 0.0040 | 2033.6 |
| CEM-CMX | 0.0712 ± 0.0013 | 0.9155 ± 0.0033 | 1992.5 |
| CEM-NICMX | 0.0076 ± 0.0004 | 0.9186 ± 0.0024 | 1992.5 |
| CMX-NICEM | 0.0057 ± 0.0004 | 0.9295 ± 0.0020 | 1992.5 |
| CEM-CMIO | 0.0407 ± 0.0010 | 0.9430 ± 0.0046 | 2033.6 |
| PHX-CMUP | 0.0298 ± 0.0008 | 0.7704 ± 0.0040 | 1916.0 |
| PHX-NICMUP | 0.0029 ± 0.0003 | 0.7748 ± 0.0039 | 1916.0 |
| PHX-CMX | 0.0134 ± 0.0006 | 0.7651 ± 0.0054 | 1883.8 |
| PHX-NICMX | 0.0013 ± 0.0002 | 0.7678 ± 0.0053 | 1883.8 |

Table 4.4: Z cross section in 2.0 fb$^{-1}$for the different $ee$ and $\mu\mu$ dilepton categories with dilepton invariant mass in the range 76 GeV/c$^2$ to 106 GeV/c$^2$.

| Category | Z Cross Section (pb) |
|---|---|
| CEM-CEM | 248.8 ± 8.1 |
| CEM-NICEM | 248.7 ± 5.5 |
| PHX-CEM | 249.8 ± 31.0 |
| PHX-NICEM | 248.6 ± 30.8 |
| CMUP-CMUP | 247.2 ± 11.4 |
| CMUP-NICMUP | 249.0 ± 7.9 |
| CMUP-CMU | 265.7 ± 16.1 |
| CMUP-NICMU | 265.1 ± 15.0 |
| CMUP-CMP | 249.9 ± 13.5 |
| CMUP-NICMP | 250.1 ± 12.7 |
| CMUP-CMX | 255.0 ± 8.8 |
| CMUP-NICMX | 254.8 ± 8.4 |
| CMUP-CMIO | 216.7 ± 11.1 |
| CMX-NICMUP | 256.3 ± 8.4 |
| CMX-CMX | 222.7 ± 11.1 |
| CMX-NICMX | 226.0 ± 8.2 |
| CMX-CMU | 297.4 ± 17.5 |
| CMX-NICMU | 298.8 ± 16.5 |
| CMX-CMP | 273.8 ± 14.3 |
| CMX-NICMP | 275.4 ± 13.6 |
| CMX-CMIO | 265.1 ± 12.8 |

mass of two leptons satisfies 76 GeV/$c^2$ $< M_{\ell\ell} <$ 106 GeV/$c^2$.

The measured on-shell Z cross sections over the whole 2.0 fb$^{-1}$data sample are shown in Table 4.4 and Figure 4.1. The Z cross section are consistent with the theoretical prediction of (∼252±9pb) within the uncertainties.theoretical prediction. The error bar in the figures reflects uncertainties of data statistics, MC statistics and overall scale factors.

## 4.4 Cross Section Numerator

The numerator of the top dilepton DIL cross section is calculated as the difference between the total number of events found passing the DIL selec-

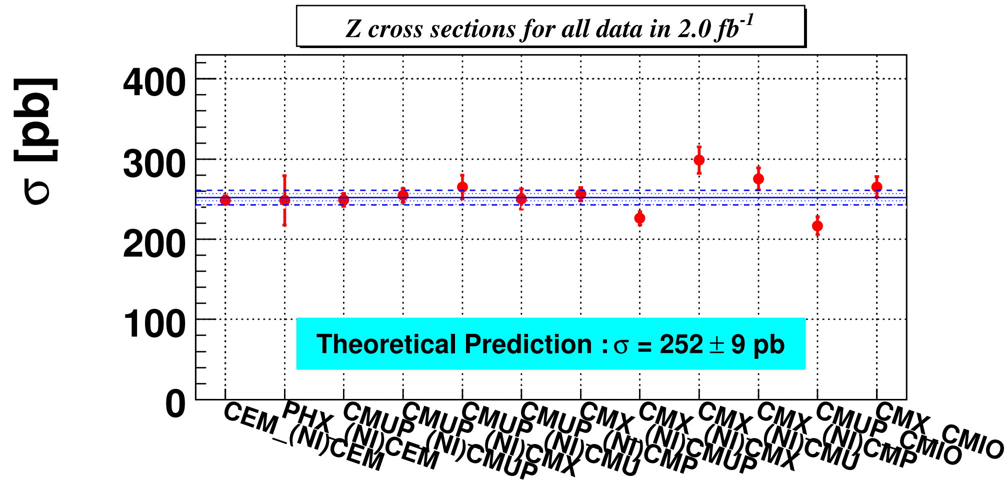


Figure 4.1: A summary of Z cross section of inclusive dilepton category in 2.0 fb$^{-1}$. "(NI)" means inclusive, i.e. both isolated and non-isolated leptons are included.

tion cuts in the data and the total background contamination expected from known Standard Model sources and fakes.

The background contamination is estimated following the methods. We can divide the backgrounds in two broad categories: MC-based and data-based. In the first category we include backgrounds coming from Standard Model processes with low cross sections, such as diboson decays, or with final state signatures for which it is hard to define an independent data control sample, as it is the case for $Z \to \tau\tau$ events. For these sources of Standard Model events, we use the MC samples described in Section 4.1. The number of events passing the DIL selection is corrected by the factors $C_{\ell_1\ell_2} \times \mathcal{L}_i$ listed in Table 4.3, and normalized to the NLO cross sections of Table 4.1.

In the second category we include background contamination coming from hard to model detector effects, like lepton contamination from jets and fake $\not\!\!E_T$ . These two effects, although small in magnitude, generate background events with two leptons in the final state because they tap onto large cross section processes like $W$+jets with a real lepton+$\not\!\!E_T$ from the $W$ decay and a fake lepton from a jet, and $Z$+jets with two real leptons and $\not\!\!E_T$ from mis-measured jet activity.

Our strategy for validating the background estimation is to compare data and background estimates in the so-called 0-jet and 1-jet bins. These control data samples come from events with two identified leptons passing all of the

Table 4.5: Jet fraction correction factors for the 0, 1 and $\geq$ 2-jet bins for $Z \rightarrow ee$ and $Z \rightarrow \mu\mu$ events. The last column is the weighted average of the two dilepton $Z$ samples and it is used for e$\mu$ reconstructed events.

| | $N_{jet}$ Scale Factor | | |
|---|---|---|---|
| | $ee$ | $\mu\mu$ | All |
| $C_{0j}$ | 1.017 $\pm$ 0.010 | 0.999 $\pm$ 0.011 | 1.010 $\pm$ 0.010 |
| $C_{1j}$ | 0.918 $\pm$ 0.012 | 0.991 $\pm$ 0.012 | 0.948 $\pm$ 0.008 |
| $C_{2j}$ | 1.056 $\pm$ 0.020 | 1.123 $\pm$ 0.020 | 1.082 $\pm$ 0.014 |

cuts applied to the top DIL candidate sample, except for the requirement of at least 2 tight jets and $H_T > 200$ GeV. The low number of jets greatly limit the $t\bar{t}$ contribution and so they naturally provide a control sample of events sharing most of the DIL candidates kinematic signatures and very little signal contamination.

New for this version of the DIL selection is the inclusion of two new diboson processes besides the $WW$ and $WZ$ processes already considered in the past. We considered possible contaminations from $ZZ$ events, with one $Z$ decaying leptonically and the other hadronically, and from $W\gamma$ events, with the $W$ decaying leptonically and the photon conversion providing the second lepton. Both are found to contribute very little to the $\geq$ 2jet sample but non negligible amounts to the 0-jet and 1-jet control bins.

Finally, the estimate of $Z \rightarrow ee$ and $\mu\mu$ events has been improved with respect to the method used in past analysis both by relying less on MC estimates and by using control regions less affected by the $t\bar{t}$ contribution. More details on the new calculation are in Section 4.4.3.

### 4.4.1 $N_{jet}$ scale factor

Since PYTHIA MC does not model properly the jet multiplicity spectrum of events with jets from ISR and FSR radiation, we correct the fraction of Monte Carlo events with no prompt jets (i.e WW, W$\gamma$ and $Z \rightarrow \tau\tau$) reconstructed in the 0, 1 and $\geq$ 2-jet bins by the correction factors $C_{0j}$, $C_{1j}$ and $C_{2j}$, also called $N_{jet}$ scale factors. These factors are calculated by comparing data and MC predictions for the jet multiplicity of $ee$ and $\mu\mu$ events in the $Z$-window region. Table 4.5 reported the $N_{jet}$ scale factors used for the 2 fb$^{-1}$top DIL analysis.

### 4.4.2 Diboson and $Z \to \tau\tau$ backgrounds

The number of diboson and $Z \to \tau\tau$ events selected at different steps of the analysis for the different categories, their final contamination to the candidate is corrected by trigger efficiency, lepton ID and $N_{jet}$ scale factor and luminosity.

For the $W\gamma$ background, given that the second lepton comes from photon conversion misidentification, we applied a conversion inefficiency scale factor equal $SF_{conv} = 1.2 \pm 0.12$. The final correction factor has to be convoluted with the numbers of electrons from photon with $E_T < 40$ GeV and found equal to 1.147 for $W\gamma \to e\nu\gamma$ events and 1.161 for $W\gamma \to \mu\nu\gamma$ events.

The systematic uncertainties on these backgrounds come from different sources as discussed in detail in section 4.5.

### 4.4.3 Drell-Yan background

The background from $Z \to ee$ and $\mu\mu$ is based on the number of data events observed in the $Z$ region with high missing transverse energy, after correcting for the presence of non $Z$ events. This remaining $Z$ contamination to the candidate region is calculated as two separate contributions: events outside the $Z$-peak region($N_{\mathrm{OUT}}$) and events inside the $Z$-peak region passing the $Z$-veto ($N_{\mathrm{IN}}$). We calculated $N_{\mathrm{IN}}$ and $N_{\mathrm{OUT}}$ from separate data estimates in the 0-jet, 1-jet and 2-jet data bins. We still use the $Z \to ee$ and $Z \to \mu\mu$ Monte Carlo to predict the ratio of events in different kinematic regions, as explained below.

The background for each $j$-th jet multiplicity bin is extracted from the following equations:

$$
\begin{aligned}
&N^{j}_{\mathrm{DY}} = N^{j}_{\mathrm{OUT}} + N^{j}_{\mathrm{IN}} \\
&N^{j}_{\mathrm{OUT}} = R^{\mathrm{out/in},\,j}_{\not{E}_T}(N^{\mathrm{DT},\,j}_{\not{E}_T} - N^{\mathrm{BKG},\,j}_{\not{E}_T}) \\
&N^{j}_{\mathrm{IN}} = R^{\mathrm{high/low},\,j}_{\mathrm{Zveto}}(N^{\mathrm{DT},\,j}_{\mathrm{Zveto}} - N^{\mathrm{BKG},\,j}_{\mathrm{Zveto}})
\end{aligned}
\tag{4.5}
$$

where the subscript "$\not{E}_T$" refers to dilepton events in the 76-106 GeV invariant mass region after the $\not{E}_T$ and L-cut but before the $Z$-veto cut; and the subscript "Zveto" refers to the subsample of these same events failing the $Z$-veto cut (i.e. with MetSig $< 4\sqrt{\mathrm{GeV}}$). $N^{\mathrm{DT},\,j}$ is the number of events observed in data in each jet bin and $N^{\mathrm{BKG},\,j}$ is the non-DY background coming from the $Z \to \tau\tau$, top, diboson and fake lepton sources. $R^{\mathrm{out/in}}$ is the ratio of events with dilepton invariant mass outside over inside the 76-106 GeV peak region. Finally $R^{\mathrm{high/low}}$ is the Monte Carlo ratio of events within the $Z$ peak region with high over low Met significance. These ratios are measured using Alpgen all $Z$ MC events per each jet multiplicity bin.

Table 4.6: Inputs to equation 4.5 used to calculate $\mathrm{N}^j_{\mathrm{OUT}}$, the $Z \to ee$ and $\mu\mu$ background contamination outside the Z peak region. The last row is the final $\mathrm{N}^j_{\mathrm{OUT}}$ for each dilepton flavor and jet multiplicity.

| Input | After $\not\!\!E_T$ and L-cut | | | | | |
|---|---|---|---|---|---|---|
| | 0-jet | | 1-jet | | ≥2-jet | |
| | $ee$ | $\mu\mu$ | $ee$ | $\mu\mu$ | $ee$ | $\mu\mu$ |
| $N^{\mathrm{DT}}_{\not E_T}$ | 50 | 33 | 47 | 38 | 43 | 33 |
| $N^{\mathrm{BKG}}_{\not E_T}$ | 20.6±0.9 | 15.0±0.7 | 12.2±1.1 | 8.9±1.0 | 11.6±0.8 | 12.6±0.8 |
| $R^{\mathrm{out/in}}$ | 0.41±0.05 | 1.01±0.14 | 0.32±0.04 | 0.42±0.05 | 0.33±0.02 | 0.35±0.02 |
| $\mathrm{N}_{\mathrm{OUT}}$ | 11.97±2.96 | 18.18±6.33 | 11.04±2.25 | 12.16±2.69 | 10.33±2.18 | 7.08±2.02 |

Table 4.7: Inputs to equation 4.5 used to calculate $\mathrm{N}^j_{\mathrm{IN}}$, the $Z \to ee$ and $\mu\mu$ background contamination inside the $Z$ peak region. The last row is the final $\mathrm{N}^j_{\mathrm{IN}}$ for each dilepton flavor and jet multiplicity.

| Input | After $\not\!\!E_T$ , L-cut and Z-veto | | | | | |
|---|---|---|---|---|---|---|
| | 0-jet | | 1-jet | | ≥2-jet | |
| | $ee$ | $\mu\mu$ | $ee$ | $\mu\mu$ | $ee$ | $\mu\mu$ |
| $N^{\mathrm{DT}}_{Zveto}$ | 40 | 25 | 42 | 34 | 38 | 29 |
| $N^{\mathrm{BKG}}_{Zveto}$ | 11.6±1.0 | 7.4±0.8 | 7.7±1.2 | 4.8±1.0 | 6.6±0.9 | 7.6 ±0.9 |
| $R^{\mathrm{low/high}}$ | 0.025±0.008 | 0.010±0.004 | 0.048±0.005 | 0.049±0.009 | 0.039±0.003 | 0.040±0.003 |
| $\mathrm{N}_{\mathrm{IN}}$ | 0.72±0.16 | 0.18±0.05 | 1.67±0.32 | 1.43±0.29 | 1.24±0.24 | 0.87±0.22 |

Tables 4.6 and 4.7 summarize the value of each term used to calculate the the $N^j_{\mathrm{OUT}}$ and $N^j_{\mathrm{IN}}$ fake contributions in equations 4.5.

The $Z$ contamination to the final top DIL candidate region is extracted from the $N^2_{\mathrm{OUT}}$ and $N^2_{\mathrm{IN}}$ estimates in the $\geq 2$ jet bin after multiplying by the efficiency of the $\mathrm{H}_T$ plus opposite sign cut, $\epsilon_{HT}$. The $\epsilon_{HT}$ efficiencies, shown in Table 4.8, are calculated using the Alpgen all $Z$ samples.

We also estimate the contamination of $Z \to \mu\mu$ events to the $e\mu$ category. Monte Carlo studies have shown that this contamination comes from events where one of the final state muon events had a very energetic photon from final state radiation. The photon, almost collinear to the muon, deposits its energy in the EM calorimeter. This EM cluster is then associated to the original muon track to fake the electron signature. As no data based control sample is available for this contamination, we estimate it using the Monte

Table 4.8: $H_T$ and opposite sign cut efficiency for the $Z \to ee$ and $\mu\mu$ background contamination in $\geq 2$ jet region. The efficiency is calculated separately for the outside $Z$ peak region, after applying only the $\not\!\!E_T$ and L-cut, and the inside $Z$ peak region, after applying also the $Z$-veto.

| $\epsilon_{HT}$ | $ee$ | $\mu\mu$ |
|---|---|---|
| After $\not\!\!E_T$ and L-cut | 0.54±0.03 | 0.61±0.03 |
| After $\not\!\!E_T$ , L-cut and $Z$-veto | 0.95±0.01 | 0.99±0.01 |

Carlo prediction.

Let's note how in the calculation of the $N^j$(BKG) terms in equation 4.5, we used the Standard Model prediction of 6.7 pb for the $t\bar{t}$ cross section for $M_{top}$ = 175 GeV. This is exactly what we are trying to measure, so we estimate final DY background using observed top cross section iteratively to remove this effect.

### 4.4.4 Fake Lepton background

Jets with large energy deposit in the electromagnetic calorimeter and a single high $p_T$ track can fake electrons. They can fake a muon if their hadron activity produce single pions or kaons with a later shower. Heavy flavor production can also results in real high $p_T$ lepton from semileptonic b and c-hadron decays.

These jets faking a lepton can produce a final state with two leptons and possibly other jets when they accompany the lepton plus $\not\!\!E_T$ signature generated by $W$+jets events. We measure the fake lepton background by weighting fakeable jets in $W$+jets events with a fake rate probability estimated from the QCD data. Sample that triggered by jet is used as QCD data. We use four different QCD samples which are jet20, jet50, jet70 and jet100 that triggered by 20, 50, 70 and 100 GeV jets, respectively.

The fake rate is a lepton type dependent probability that a fakeable object, that is an object which shares some of the jets and some of the high $p_T$ lepton characteristics, can be reconstructed as a good lepton. A fakeable object is narrowly defined as more than 20 GeV any EM cluster with HAD/EM energy deposition < 0.125 or a more than 20 GeV any track with E/p< 1. To remove real lepton contamination in $W$+jet events from $Z$ and Diboson, fakeable object is required to have at least one failure of the ID cut, shown in Table 4.9, as a anti-cut. In order to increase the statistics of fakeable objects we allow both stub and stubless muons i.e. we have CMUP fiducial CMUP

Table 4.9: Anti-cut variables. Fakeable events require at least one of these ID cuts. Detail of lepton ID is shown Section 3.

| | List of anti-cut variables |
|---|---|
| TCEM, NCEM | $E_{\text{had}}/E_{\text{em}}$, $\chi^2_{\text{strip}}$, $L_{\text{shr}}$, $\lvert\Delta x\rvert$, $\lvert\Delta z\rvert$ |
| TPHX | $E_{\text{had}}/E_{\text{em}}$, $\chi^2_{3\times3}$, $U_{5\times9}$, $V_{5\times9}$ |
| TCMUP, TCMUX, LMUO, NMUO | Stubb, $E_{\text{had}}$, $E_{\text{em}}$, stub deltaX |
| LMIO | $E_{\text{had}}$, $E_{\text{em}}$, $E_{\text{total}}$ |

Table 4.10: Some parameter of QCD jet sample, and jet Et threshold cut value to ensure 90% trigger efficiency.

| | jet20 | jet50 | jet70 | jet100 |
|---|---|---|---|---|
| luminosity | 2009.9 $\text{pb}^{-1}$ | 2010.2 $\text{pb}^{-1}$ | 2010.1 $\text{pb}^{-1}$ | 2010.3 $\text{pb}^{-1}$ |
| Effective pre-scale | 988 | 48.7 | 8 | 1 |
| jet Et threshold cut | 35 GeV | 55 GeV | 75 GeV | 105 GeV |

Stubless muon in fakeable object.

We are assuming fake lepton from jet, so numerator of fake rate should not include any real lepton from $W$, DY, and Diboson. So we need to remove the real lepton contamination in the QCD jet sample. We used MC prediction for (DY$\rightarrow ee$(Alpgen), DY$\rightarrow \mu\mu$(Alpgen), DY$\rightarrow \tau\tau$(ALPGEN), $WW$(PYTHIA), $WZ$(PYTHIA), $ZZ$(PYTHIA)) to estimate this real lepton contamination. For the MC events we have increased the jet Et threshold to correspond to a 90% trigger efficiency. We are able to mimic the trigger turn on curve by using Et's of 35, 55, 75 and 105 GeV corresponding to the jet20, jet50, jet70 and jet 100 triggers.

Real lepton is calculated using the following equation:

$$\text{RealLepton}_{MC} = \frac{\text{Acc}_{MC}\times\sigma_{MC}\times\text{lum}_{jet}}{\text{EffectivePS}_{jet}} \tag{4.6}$$

"Acc" is each MC's one lepton and more than one threshold Et jet acceptance. "lum" is luminosity of each QCD jet sample. "Effective $\text{PS}_{jet}$" is sum of each run's weighted pre-scale by each run's luminosity. QCD jet sample's detail parameter is Table 4.10.

We subtract this real lepton contamination from jet sample's good lepton and fakeable object. Fake Rate is calculated using the following equation:

$$\text{FakeRate} = \frac{\text{GoodLepton}_{jet}-\text{RealLepton}_{MC}}{\text{Fakeable}_{jet}-\text{RealFakeable}_{MC}} \tag{4.7}$$

Table 4.11: JET50 fake rates vs lepton $p_T$ range for different fakeable objects.

| Fake lepton | JET50 Fake rate | | | | | |
|---|---|---|---|---|---|---|
| | [20–30] GeV | [30–40] GeV | [40–60] GeV | [60–100] GeV | [100–200] GeV | $p_T \geq 200$ GeV |
| TCEM | $0.0413 \pm 0.0010$ | $0.0345 \pm 0.0009$ | $0.0240 \pm 0.0001$ | $0.0285 \pm 0.0002$ | $0.0327 \pm 0.0013$ | $0.0342 \pm 0.0198$ |
| NCEM | $0.0074 \pm 0.0000$ | $0.0052 \pm 0.0000$ | $0.0057 \pm 0.0000$ | $0.0050 \pm 0.0000$ | $0.0085 \pm 0.0008$ | $0.0000 \pm 0.0000$ |
| TPHX | $0.1419 \pm 0.0011$ | $0.1515 \pm 0.0015$ | $0.1240 \pm 0.0002$ | $0.2041 \pm 0.0002$ | $0.2606 \pm 0.0026$ | $0.0985 \pm 0.0580$ |
| TCMUP | $0.0116 \pm 0.0005$ | $0.0266 \pm 0.0013$ | $0.0385 \pm 0.0016$ | $0.0729 \pm 0.0034$ | $0.0546 \pm 0.0068$ | $0.0000 \pm 0.0000$ |
| TCMUX | $0.0098 \pm 0.0008$ | $0.0249 \pm 0.0020$ | $0.0446 \pm 0.0029$ | $0.0654 \pm 0.0073$ | $0.0035 \pm 0.0744$ | $0.0031 \pm 0.0040$ |
| LMUO | $0.0276 \pm 0.0006$ | $0.0341 \pm 0.0017$ | $0.0428 \pm 0.0026$ | $0.0494 \pm 0.0070$ | $0.0867 \pm 0.0098$ | $0.0062 \pm 0.0038$ |
| NMUO | $0.0052 \pm 0.0000$ | $0.0037 \pm 0.0000$ | $0.0022 \pm 0.0000$ | $0.0023 \pm 0.0001$ | $0.0027 \pm 0.0005$ | $0.0024 \pm 0.0024$ |
| LMIO | $0.2018 \pm 0.0011$ | $0.2246 \pm 0.0031$ | $0.2462 \pm 0.0040$ | $0.3563 \pm 0.0086$ | $0.2936 \pm 0.0176$ | $1.0298 \pm 0.0203$ |

Where the subscript "jet" refers to number estimated from the QCD jet sample; and the subscript "MC" refers to number from the MC prediction. "GoodLepton" is number of reconstructed lepton in QCD jet sample. "RealLepton" is the number of fakeable in QCD jet sample. "RealLepton" and "RealFakeable" are number of good lepton and fakeable predicted by MC, i.e. the real lepton contamination.

Depending on the geometrical region where the fakeable points to, we define separate fakeable categories for CEM and PHX electrons (TCEM and TPHX), and for CMUP, CMX, CMU/CMP and CMIO muons (TMUO, TCMX, LMUO and LMIO). For non isolated leptons (NCEM and NMUO), we require that the fakeable object is also non isolated.

Using the JET50 QCD data sample, we calculated the fake rates reported in Table 4.11 and shown in Figure 4.2. The six variable-width $p_T$ bins ([20–30] GeV, [30–40] GeV, [40–60] GeV, [60–100] GeV,[100–200] GeV and $\geq$ 200 GeV) are chosen so to have a reasonable statistics in each bin.

Figure 4.3 shows a comparison between the $E_T$ distribution of each QCD jet sample and lepton + fakeable events. Specially, isolated electron category have a big difference due to the residual trigger biases. This difference make difference in the low $E_T$ region's fake rate, but our assessed systematics uncertainty of fake bkg include this difference.

Figure 4.4 shows a comparison between the number of fake lepton events observed in the JET20, JET70 and JET100 data sample, integrated over the full $p_T$ spectrum, and what is predicted by the JET50 fake rate matrix. Based on this plot, we assess a 30% systematic uncertainty for the JET50-based electron and muon fake rate estimate.

The fake lepton contamination to the control bins and to the top DIL candidate sample are calculated by weighting each "lepton+fakeable" event by the appropriate fake rate in Table 4.11 and summing all of the fake contributions together.

We define as "lepton+fakeable" any event in the central high $p_T$ lepton datasets with one and only one good high $p_t$ lepton, $\not\!\!E_T$ >25 GeV and a second fakeable object, and passing the anti-cut. The fakeable object, which can be from any of the fake categories defined above, is paired to the good lepton and treated as the second lepton in the event when calculating any of the kinematic variables used in the top DIL selection (dilepton invariant mass, corrected $\not\!\!E_T$ , $\mathrm{H}_T$..). Tight jets found in a cone of $\Delta R < 0.4$ around the fakeable lepton are dropped from the tight jet counting of that event. The fakeable object is allowed to be the trigger lepton if it belongs to TCEM, TCMUP or TCMX category. If more than one fakeable object is found in the event, we pair each of them to the good lepton.

The fake lepton uncertainty contains a statistical component, which is the sum of the fake rate uncertainty itself and the statistics of the "lepton+fakeable" sample, and a systematic component coming from the 30% fake rate systematic uncertainty derived from Figure 4.4. When summing together the fake rate from different "lepton+fakeable" dilepton categories, the 30% uncertainties in fake $ee$ and in fake $\mu\mu$ pairs (i.e. good electron plus fakeable electron and good muon plus fakeable muon pairs) are assumed to be uncorrelated and summed in quadrature while the 30% uncertainty of fake $e\mu$ pairs (i.e. good electron paired to a fakeable muon or good muon paired to a fakeable electron) is considered fully correlated and added linearly.

We compare our same sign fake background estimation and same sign dilepton candidate in the signal region. We are using fakeable lepton's charge as fake lepton's charge. Same sign dilepton candidate after subtraction of Standard Model same sign events are fake lepton. Therefore comparison of our same sign fake background and data's same sign candidate is good check of our fake background estimation method. Check results are given in Table 4.12. We remove Drell-Yan and Diboson MC's same sign events from data same sign dilepton candidate as Standard Model same sign events. Results is very consistent.

## 4.5 Systematics Studies

In this section we briefly review the systematics studies performed for the signal and backgrounds MC estimates.

A common systematics to signal and background MC estimates comes from the uncertainty on the lepton ID scale factors. These factors are measured in Z events, which have a limited jet activity. limit possible systematic variations in the lepton scale factor due to extra-jet activity to 1.1%. We assign a conservative systematic of 2% to the lepton ID scale factors of table 4.2 and assumed that it is 100% correlated among the different MC samples.

Table 4.12: Comparison between our same sing fake background and data same sign dilepton candidate after subtraction of Standard Model same sign events.

| | $ee$ | $\mu\mu$ | $e\mu$ | all |
|---|---|---|---|---|
| SS data in 0jet | 6.99 ± 3.74 | 9.02 ± 3.32 | 10.68 ± 4.24 | 29.36 ± 6.56 |
| Our same sign fake in 0jet | 6.02 ± 0.71 | 5.16 ± 1.10 | 13.07 ± 1.27 | 24.24 ± 1.84 |
| SS data in 1jet | 5.95 ± 3.00 | 0.06 ± 1.00 | 17.60 ± 4.69 | 23.50 ± 5.66 |
| Our same sign fake in 1jet | 3.15 ± 0.44 | 4.43 ± 0.67 | 16.37 ± 1.26 | 23.95 ± 1.51 |
| SS data in 2 more jet | 4.59 ± 2.45 | 0.76 ± 1.00 | 17.33 ± 4.36 | 22.70 ± 5.10 |
| Our same sign fake in 2 more jet | 2.00 ± 0.32 | 4.82 ± 0.61 | 13.92 ± 1.27 | 20.73 ± 1.44 |

Table 4.13: Systematics uncertainties, as percentage of the raw Monte Carlo acceptance, due to JES systematic variation for the different Standard Model processes.

| Source | 0j(%) | 1j(%) | $\geq$ 2j(%) | $H_T$, OS(%) |
|---|---|---|---|---|
| $t\bar{t}$ (PYTHIA) | 26.6 | 12.9 | 2.6 | 3.2 |
| $Z \rightarrow \tau\tau$(Alpgen) | 6.8 | 12.9 | 31.3 | 23.7 |
| WW (PYTHIA) | 3.3 | 7.7 | 13.4 | 14.3 |
| WZ (PYTHIA) | 5.4 | 1.4 | 13.3 | 15.9 |
| ZZ (PYTHIA) | 3.8 | 219 | 11.3 | 12.3 |
| W$\gamma$ (Baur) | 2.6 | 5.6 | 9.1 | 10.0 |

Another common systematics comes from jet energy scale uncertainties. This is measured using the change in the default acceptance obtained from shifting the jet corrections up and down by $1\sigma$ of their systematic uncertainty. Although the central value for this systematic source is calculated separately for each MC background sample and, within each sample, for each jet multiplicity bin (see Table 4.13), a 100% correlation is assumed when propagating this systematic uncertainty to final cross section.

A final source of correlated systematic, this time affecting only MC-based backgrounds, is the uncertainty on the $N_{jet}$ scale factor.

Uncorrelated sources of systematic uncertainties are the jet fake systematics, the cross section uncertainties and a 30% systematic uncertainty on the conversion rejection scale factor. For the signal acceptance, we estimated systematic uncertainties due to multiple effects: MC generator, ISR/FSR

Table 4.14: Systematics uncertainties, as percentage of the raw $t\bar{t}$ acceptance, for the different sources. considered in this analysis. The total error is the sum in quadrature of each contribution.

| Source | Systematic Error (%) |
|---|---|
| MC Generator | 1.5 |
| ISR | 1.7 |
| FSR | 1.1 |
| PDF's | 0.8 |
| Jet corrections | 3.2 |
| Total | 4.2 |

variations and PDF's uncertainty. The first two components are calculated by comparing the raw MC acceptance of the default $t\bar{t}$ sample (`PYTHIA`) to specialized MC samples. Details on the PDF's uncertainty calculation are contained in the next section. A summary tables of the systematic uncertainties affecting the $t\bar{t}$ acceptance is shown in Table 4.14.

### 4.5.1 Systematics due to PDF uncertainties

The CTEQ5L parton distribution function (PDF) are used in the default $t\bar{t}$ PYTHIA sample. To evaluate the systematics due to PDF uncertainties, we calculate the acceptance variation from the default acceptance when we use different PDF sets, namely MRST72, MRST75, CTEQ6L, CTEQ6L1 and CTEQ6M. To calculate the dependence of the acceptance on the different PDF sets, we adopt the weighted MC method. In this method, we reweigh each event of a MC sample we already have, instead of generating a different set of MC events for each different PDF sets. We first obtain the parton momentum fractions $x_1$ and $x_2$ and $Q^2$ for each $t\bar{t}$ MC event, next we calculate the relative probability of the event for the PDF set we are considering by dividing it by the probability of the same event for the default PDF set (CTEQ5L). We use the relative probability as a weight for each event, and the sum of these weights for accepted events over the sum of the weights for the whole generated sample gives a rough estimate of the acceptance with each different PDF set. Table 4.15 summarizes the resulting acceptances and variations from the default acceptance using CTEQ5L.

We estimate the effect of different PDF set to be $\pm 0.374\%$ by comparing the acceptance of MRST72 with CTEQ5L which gives the largest effect on

Table 4.15: Signal acceptance for different PDF sets evaluated using the weighted MC method. Differences from the default $t\bar{t}$ acceptance using CTEQ5L are also listed.

| PDF | Acceptance( % ) | Difference( % ) | Description |
|---|---|---|---|
| CTEQ5L | 0.8084 | — | default PDF set |
| MRST72 | 0.8114 | 0.374 | default MRST |
| MRST75 | 0.8106 | 0.277 | MRST lower $\alpha_s$ |
| CTEQ6L | 0.8092 | 0.103 | different $\alpha_s$ |
| CTEQ6L1 | 0.8088 | 0.044 | different $\alpha_s$ |
| CTEQ6M | 0.8097 | 0.157 | |

the acceptance in the table. Likewise, we estimate the effect of $\alpha_s$ uncertainty to be $\pm 0.097\%$ by comparing MRST72 with MRST75.

In the next step, we estimate the effect due to the variation of 20 independent parameters of the CTEQ6M PDF fit. We evaluate the acceptance, calculated using the weighted MC method as well, by shifting up and down by $1\sigma$ the uncertainties of 20 eigenvector directions within CTEQ6M. Table 4.16 summarizes the central value for the acceptances using the weighted MC method and its percentage difference with respect to the default CTEQ6M acceptance for each of the 20 eigenvector shifts.

The sum in quadrature of the all of the positive and negative variations gives us a value of $+0.324\%$ and $-0.716\%$, respectively, for the systematic uncertainty due to uncertainties in 20 parameters of PDF.

The sum in quadrature of the systematics from the uncertainty of MRST, $\alpha_s$, and 20 parameters is $+0.504\%$ to the positive side and $-0.814\%$ to the negative side. We quote 0.814% which is larger one as the systematic due to PDF uncertainties.

## 4.6 Background and Signal Tables

The first step in validating the top DIL selection for the 2 fb$^{-1}$analysis is to produce the background tables for the 0-jet and 1-jet control bins, using a cut on MetSig cut as a Z-veto rejection tool. The results are shown in Tables 4.17. In general we see excellent agreement between data and predictions which give us confidence in the predictability of the methods used to calculate the backgrounds for high $\not\!\!E_T$ events dilepton events. Figures 4.6 show the $t\bar{t}$ and background prediction, overlaid to the data, for some kinematic distributions of events in the 0-jet and 1-jet bin, respectively.

Secondly, Tables 4.18 give number of 2 jet bin before the $\mathrm{H}_T$ and the opposite lepton charge requirement. Figures 4.7 show the $t\bar{t}$ and gackgorund prediction of this region.

Finally, Tables 4.19 give the observed number of DIL candidate events versus the background and $t\bar{t}$ signal expectations for the full 2 $\mathrm{fb}^{-1}$samples. The total SM expectation is well in agreement with the observed 145 events for the 2 $\mathrm{fb}^{-1}$respectively. Figures 4.8 show the $t\bar{t}$ and background prediction, overlaid to the data, for some candidate events kinematic distributions.

## 4.7 Results of Measured Top Pair Production Cross Section

Figure 4.9 shows the jet multiplicity distribution of signal and background after the Z-veto, $\not{E}_T$ and L-cut.

Using the numbers in Table 4.19 for the numerator, and the denominator quoted in Section 4.3, we measure:

$$\begin{aligned} \sigma(p\bar{p} \to t\bar{t}X) &= 6.8 \ \pm 1.0 \text{ (stat.)} \ \pm 0.4 \text{ (syst.)} \ \pm 0.4 \text{ (lum.)} \ \text{ pb} \\ &= 6.8 \ \pm 1.1 \text{ pb} \end{aligned} \tag{4.8}$$

for the 2 $\mathrm{fb}^{-1}$ data sample, after propagating the acceptance and background systematics uncertainties. The last error is 6% uncertainty coming from luminosity measurement.

Figure 4.10 shown $\sigma(p\bar{p} \to t\bar{t}X)$ as a function of top quark mass with our results.

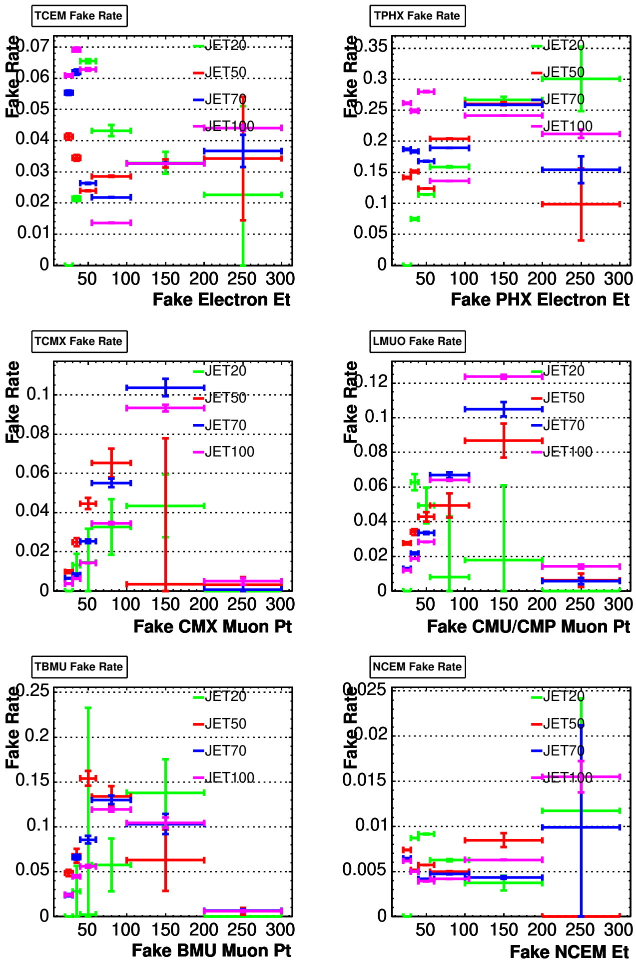


Figure 4.2: Fake rate estimates versus lepton $p_T$ for each fakeable category. The JET50 fake rates, shown in red, are compared to the JET20 , JET70 and JET100 fake rates. TBMU fakeable objects are not used in this analysis.

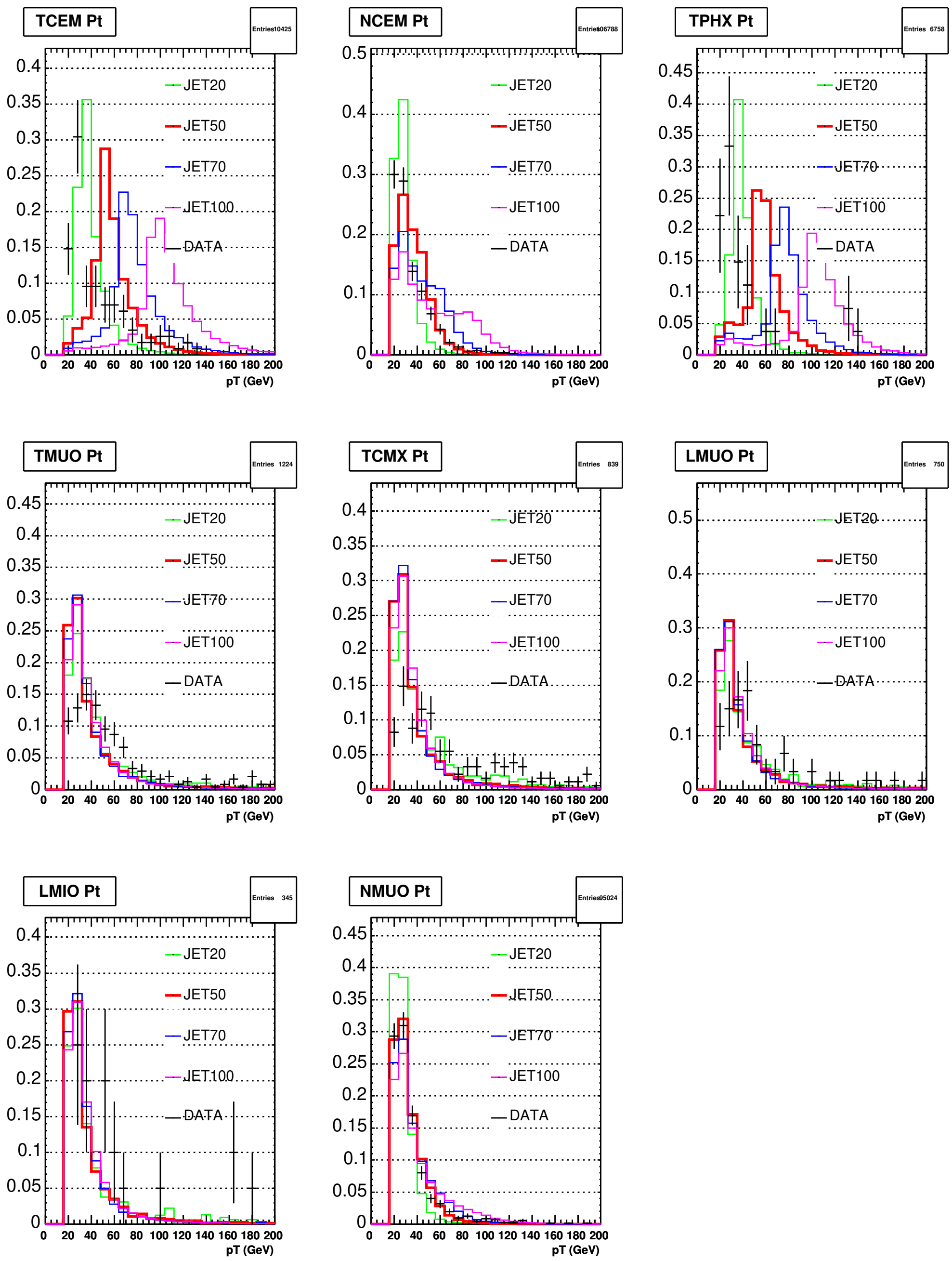


Figure 4.3: Fakeable $E_T$ distribution of each QCD jet sample and lepton + fakeable events

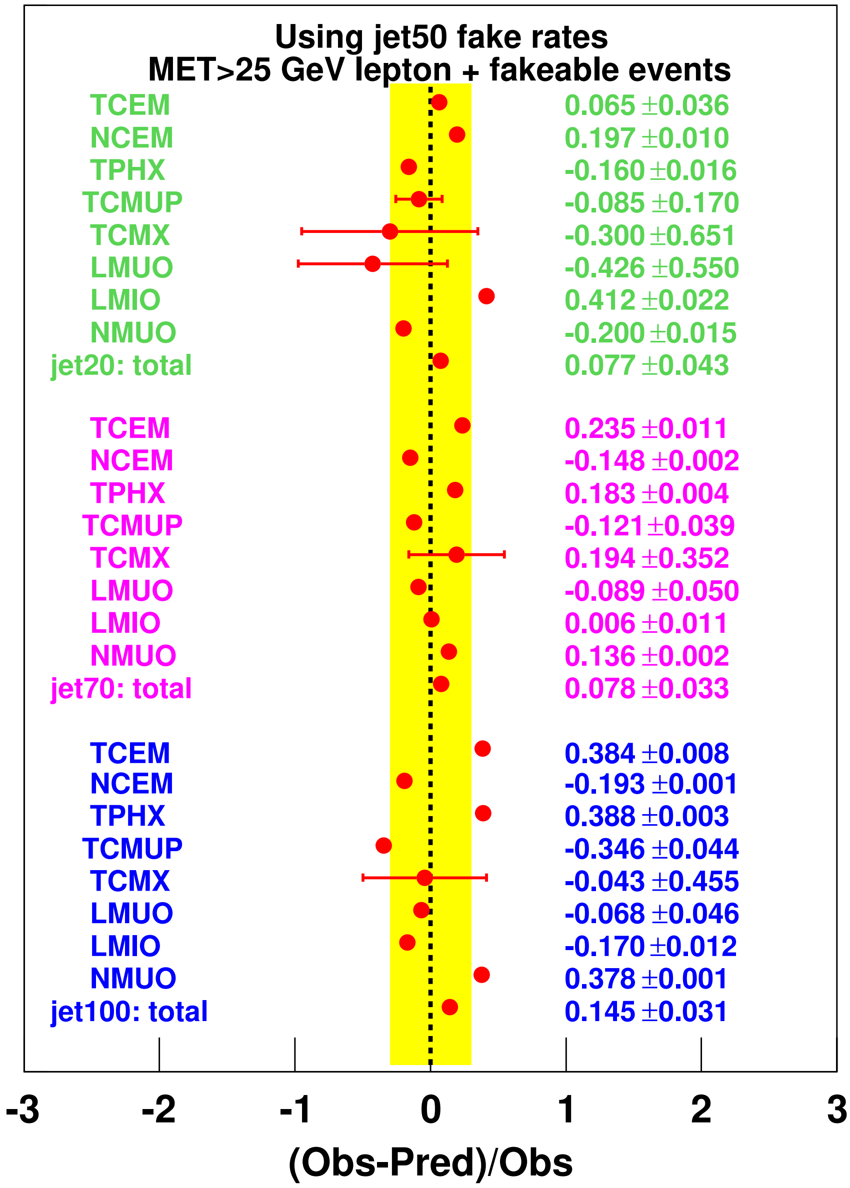


Figure 4.4: Ratio of observed total number of fake lepton for each fakeable category vs the JET50-based prediction. With the exclusion of the isolated electron yields in the JET20 sample, the predictability of the JET50 $p_T$ dependent fake rate is good at the 30% level, as shown by the yellow band in the plot.

Table 4.16: Signal acceptance using the the CTEQ6M PDF's shifted up and down by $1\sigma$ along 20 eigenvector directions. Each acceptance is evaluated using the weighted MC method. The percentage difference with respect to the CTEQ6M central value acceptance of 0.8097% is also listed.

| Eigenvector index | Acceptance( % ) $+1\sigma$ up | Diff.( % ) | Acceptance( % ) $-1\sigma$ down | Diff.( % ) |
|---|---|---|---|---|
| # 1 | 0.8100 | 0.0380 | 0.8094 | $-0.0380$ |
| # 2 | 0.8096 | $-0.0053$ | 0.8097 | 0.0057 |
| # 3 | 0.8098 | 0.0209 | 0.8095 | $-0.0190$ |
| # 4 | 0.8097 | $-0.0009$ | 0.8097 | 0.0019 |
| # 5 | 0.8095 | $-0.0166$ | 0.8098 | 0.0149 |
| # 6 | 0.8105 | 0.1029 | 0.8088 | $-0.1024$ |
| # 7 | 0.8086 | $-0.1280$ | 0.8106 | 0.1161 |
| # 8 | 0.8110 | 0.1609 | 0.8085 | $-0.1429$ |
| # 9 | 0.8103 | 0.0784 | 0.8091 | $-0.0729$ |
| # 10 | 0.8102 | 0.0642 | 0.8091 | $-0.0656$ |
| # 11 | 0.8096 | $-0.0082$ | 0.8096 | $-0.0106$ |
| # 12 | 0.8092 | $-0.0541$ | 0.8096 | $-0.0036$ |
| # 13 | 0.8104 | 0.0837 | 0.8088 | $-0.1031$ |
| # 14 | 0.8101 | 0.0496 | 0.8096 | $-0.0086$ |
| # 15 | 0.8110 | 0.1688 | 0.8046 | $-0.6233$ |
| # 16 | 0.8093 | $-0.0499$ | 0.8094 | $-0.0298$ |
| # 17 | 0.8097 | 0.0000 | 0.8090 | $-0.0842$ |
| # 18 | 0.8098 | 0.0193 | 0.8099 | 0.0230 |
| # 19 | 0.8081 | $-0.1930$ | 0.8100 | 0.0377 |
| # 20 | 0.8092 | $-0.0585$ | 0.8100 | 0.0466 |

Table 4.17: Summary tables for the 2 fb$^{-1}$ Inclusive DIL sample. The top/bottom table shows the total number of background, SM expectation and data candidate events, divided by lepton flavor contribution, for 0 and 1 jet bins. The quoted uncertainties is the sum of the statistical and systematics uncertainty.

| Events per 2000 pb$^{-1}$ with N$jet = 0$ before $H_T$ and opposite lepton charge requirement | | | | |
|---|---|---|---|---|
| Source | ee | $\mu\mu$ | e$\mu$ | $\ell\ell$ |
| WW | 26.06±2.80 | 20.38±2.20 | 53.75±5.73 | 100.19±10.63 |
| WZ | 2.05±0.19 | 3.04±0.27 | 2.97±0.27 | 8.06±0.70 |
| ZZ | 2.94±2.28 | 2.84±2.20 | 0.29±0.22 | 6.07±4.70 |
| W$\gamma$ | 10.24±3.57 | 0.00±0.00 | 8.89±1.79 | 19.13±5.09 |
| DY$\rightarrow \tau\tau$ | 0.68±0.19 | 0.52±0.16 | 1.49±0.29 | 2.69±0.43 |
| DY$\rightarrow ee + \mu\mu$ | 11.80±3.08 | 18.22±6.45 | 5.85±0.95 | 35.87±7.47 |
| Fakes | 14.29±4.41 | 9.77±3.21 | 27.53±8.42 | 51.59±13.87 |
| Total background | 68.07±10.93 | 54.77±9.26 | 100.77±11.85 | 223.60±28.32 |
| $t\bar{t}$ ($\sigma = 6.7$ pb) | 0.11±0.02 | 0.12±0.02 | 0.24±0.03 | 0.47±0.05 |
| Total SM expectation | 68.17±10.94 | 54.89±9.27 | 101.01±11.86 | 224.07±28.35 |
| DATA | 76 | 54 | 109 | 239 |

| Events per 2000 pb$^{-1}$ with N$jet = 1$ before $H_T$ and opposite lepton charge requirement | | | | |
|---|---|---|---|---|
| Source | ee | $\mu\mu$ | e$\mu$ | $\ell\ell$ |
| WW | 6.70±0.84 | 6.34±0.80 | 15.38±1.89 | 28.43±3.45 |
| WZ | 3.52±0.27 | 1.93±0.16 | 2.96±0.23 | 8.41±0.62 |
| ZZ | 1.13±0.88 | 1.15±0.89 | 0.65±0.51 | 2.93±2.27 |
| W$\gamma$ | 2.44±0.98 | 0.00±0.00 | 3.09±0.81 | 5.53±1.57 |
| DY$\rightarrow \tau\tau$ | 3.31±0.62 | 3.21±0.60 | 6.35±1.15 | 12.87±2.28 |
| DY$\rightarrow ee + \mu\mu$ | 12.28±2.93 | 13.58±3.38 | 2.38±0.65 | 28.24±5.55 |
| Fakes | 7.94±2.48 | 9.34±2.91 | 44.05±13.42 | 61.32±17.25 |
| Total background | 37.32±6.19 | 35.55±5.93 | 74.86±14.21 | 147.73±22.59 |
| $t\bar{t}$ ($\sigma = 6.7$ pb) | 2.81±0.23 | 2.92±0.24 | 6.83±0.54 | 12.56±0.97 |
| Total SM expectation | 40.13±6.37 | 38.48±6.09 | 81.69±14.38 | 160.30±23.19 |
| DATA | 43 | 40 | 69 | 152 |

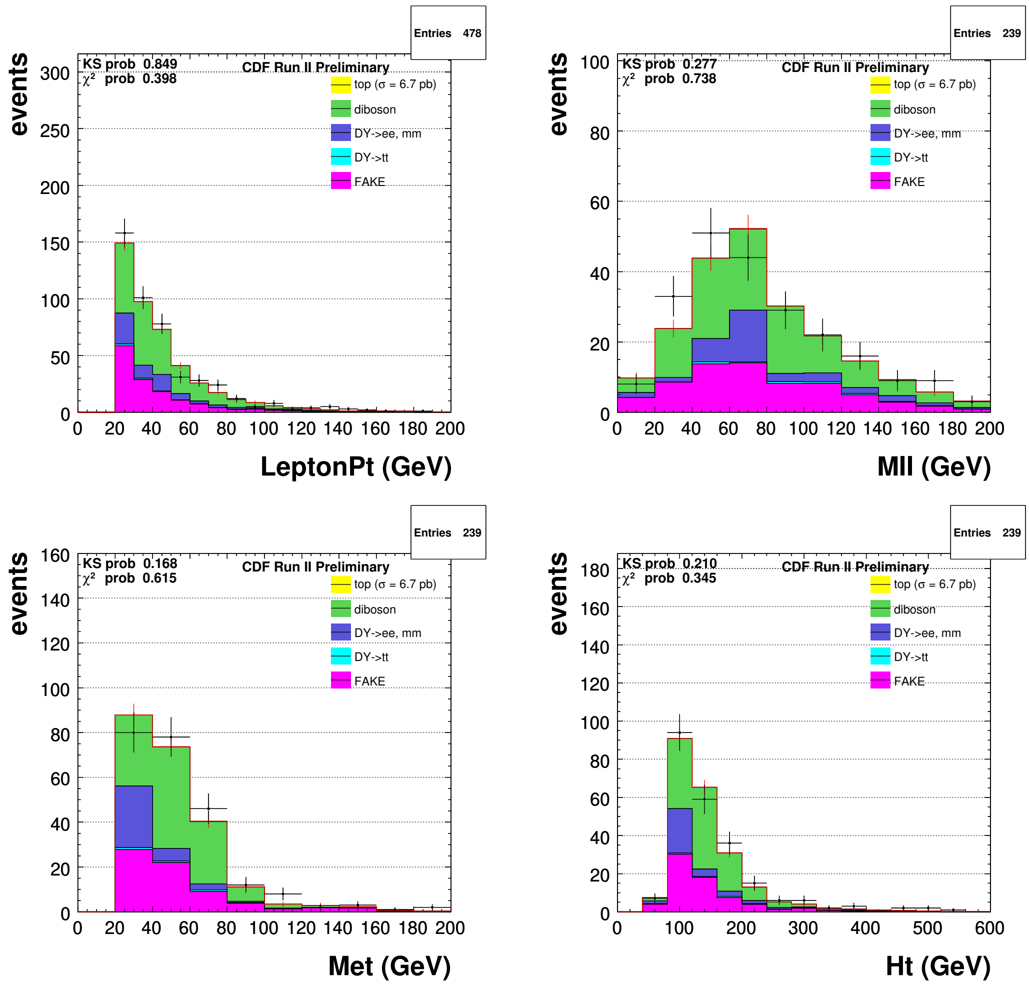


Figure 4.5: From top left to bottom right: background and top signal predictions, overlaid to data, for the lepton transverse energy spectrum, the dilepton invariant mass, $\not{E}_T$ and $H_T$ in 2 fb$^{-1}$0-jet events.

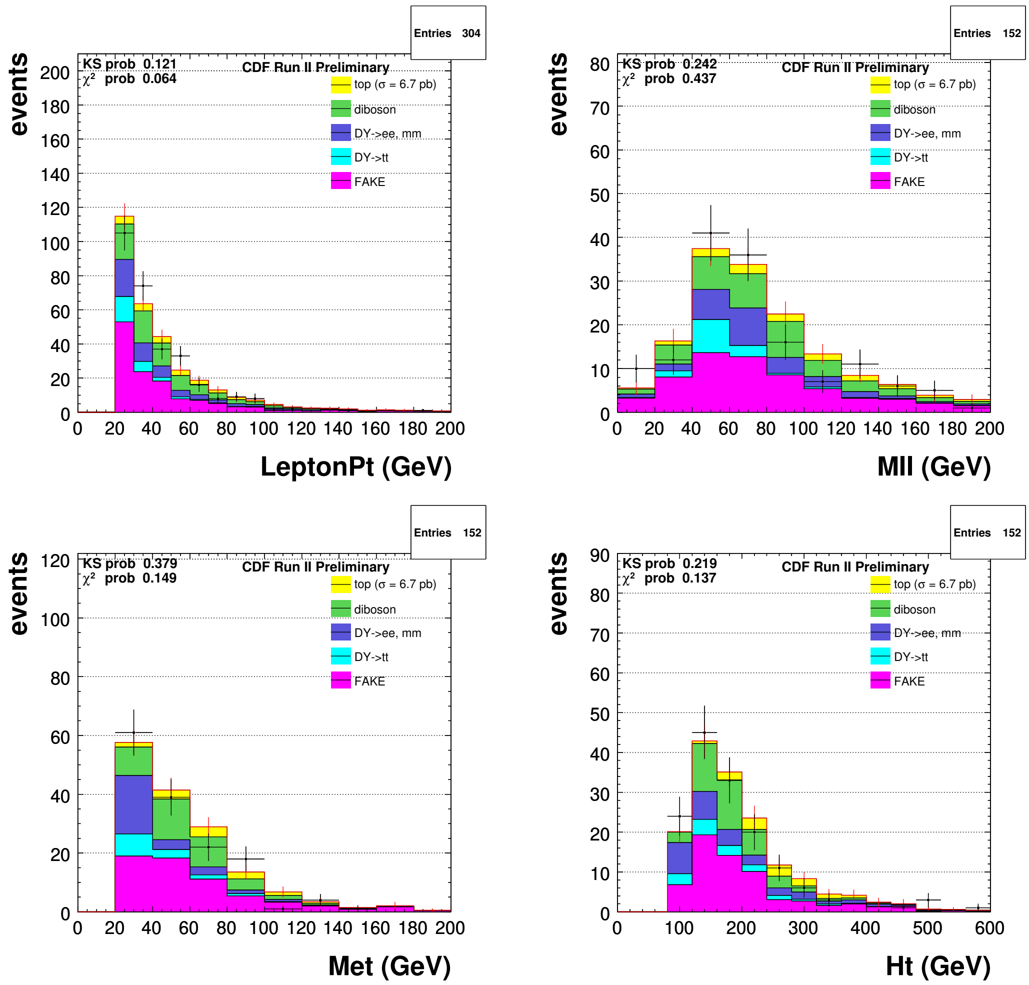


Figure 4.6: From top left to bottom right: background and top signal predictions, overlaid to data, for the lepton transverse energy spectrum, the dilepton invariant mass, $\not\!\!E_T$ and $H_T$ in 2 fb$^{-1}$1-jet events.

Table 4.18: Summary tables for the 2 fb$^{-1}$ Inclusive DIL sample. The top/bottom table shows the total number of background, SM expectation and data candidate events, divided by lepton flavor contribution, 2 jet bins before the H$_T$ and the opposite lepton charge requirement events. The quoted uncertainties is the sum of the statistical and systematics uncertainty.

| Events per 2000 pb$^{-1}$ with N$jet$ => 2 before $H_T$ and opposite lepton charge requirement | | | | |
|---|---|---|---|---|
| Source | ee | $\mu\mu$ | e$\mu$ | $\ell\ell$ |
| WW | 2.58±0.48 | 2.66±0.50 | 5.46±0.99 | 10.70±1.90 |
| WZ | 1.24±0.18 | 0.74±0.11 | 1.21±0.18 | 3.19±0.45 |
| ZZ | 0.59±0.46 | 0.54±0.42 | 0.34±0.27 | 1.47±1.15 |
| W$\gamma$ | 0.46±0.31 | 0.00±0.00 | 1.08±0.43 | 1.54±0.59 |
| DY→ $\tau\tau$ | 2.12±0.55 | 2.38±0.62 | 4.82±1.24 | 9.32±2.39 |
| DY→ $ee + \mu\mu$ | 11.46±3.70 | 7.95±2.90 | 1.27±0.53 | 20.68±6.17 |
| Fakes | 6.35±2.01 | 12.58±3.96 | 32.27±9.86 | 51.20±14.29 |
| Total background | 24.80±5.62 | 26.85±5.77 | 46.45±10.37 | 98.10±18.65 |
| $t\bar{t}$ ($\sigma$ = 6.7 pb) | 22.28±1.71 | 23.76±1.82 | 53.83±4.10 | 99.86±7.60 |
| Total SM expectation | 47.07±7.12 | 50.61±7.06 | 100.28±12.25 | 197.96±24.10 |
| DATA | 43 | 50 | 107 | 200 |

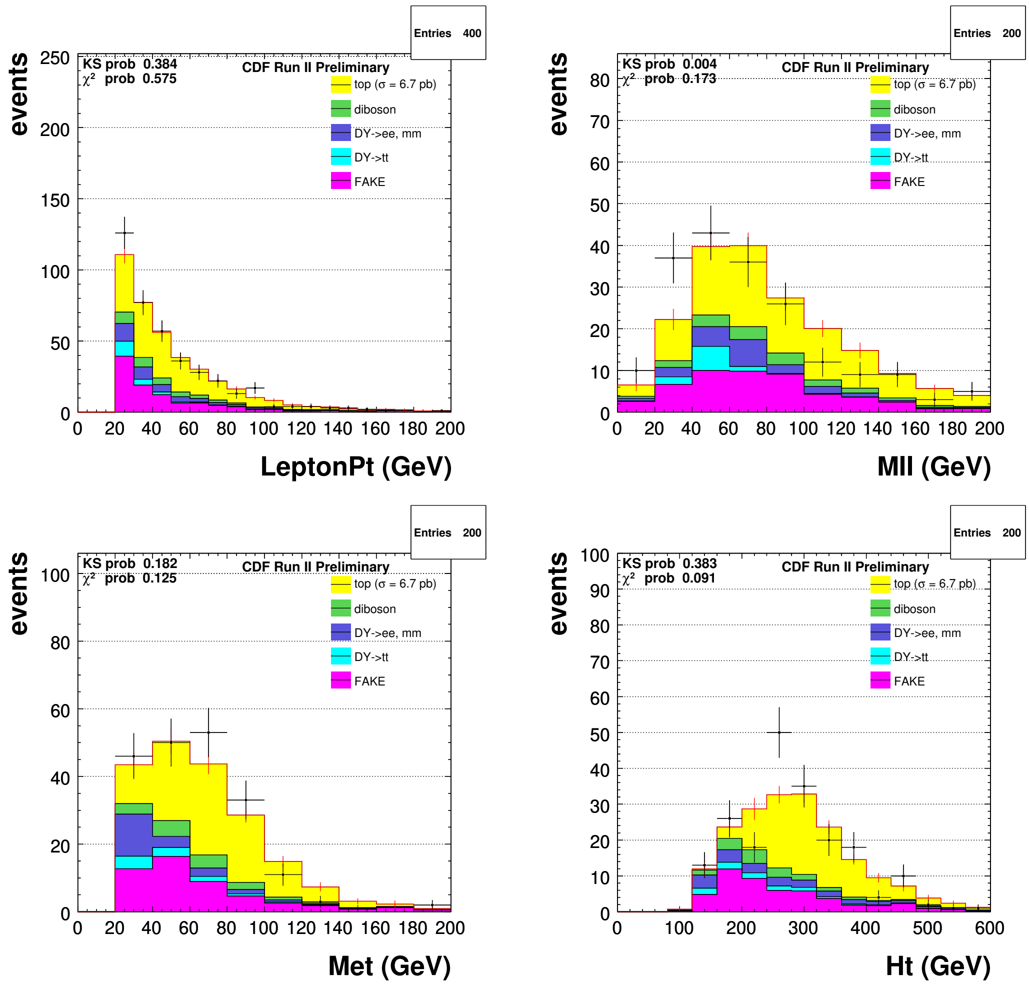


Figure 4.7: From top left to bottom right: background and top signal predictions, overlaid to data, for the lepton transverse energy spectrum, the dilepton invariant mass, $\not\!\!E_T$ and $H_T$ in 2 fb$^{-1}$2-jet before the $H_T$ and the opposite lepton charge requirement events.

Table 4.19: Summary tables for the 2 fb$^{-1}$ Inclusive DIL sample in the signal region. The top table shows the total number of background, SM expectation and data candidate events, divided by lepton flavor contribution. The bottom table shows the same contributions in the 0, 1, 2 jet bins and 2 jet bins after the H$_T$ and the opposite lepton charge requirement. The quoted uncertainties is the sum of the statistical and systematics uncertainty.

| Events per 2000 pb$^{-1}$ after all cuts | | | | |
|---|---|---|---|---|
| Source | ee | $\mu\mu$ | e$\mu$ | $\ell\ell$ |
| WW | 1.56±0.29 | 1.76±0.33 | 3.48±0.61 | 6.81±1.17 |
| WZ | 0.67±0.11 | 0.49±0.09 | 0.43±0.08 | 1.59±0.26 |
| ZZ | 0.46±0.36 | 0.46±0.36 | 0.16±0.13 | 1.09±0.85 |
| W$\gamma$ | 0.17±0.18 | 0.00±0.00 | 0.00±0.00 | 0.17±0.18 |
| DY$\rightarrow\tau\tau$ | 1.19±0.24 | 1.28±0.26 | 2.79±0.55 | 5.26±1.02 |
| DY$\rightarrow ee+\mu\mu$ | 6.63±1.47 | 5.17±1.38 | 0.98±0.44 | 12.78±2.17 |
| Fakes | 2.79±0.95 | 6.54±2.22 | 12.42±3.91 | 21.75±6.33 |
| Total background | 13.48±2.19 | 15.70±2.89 | 20.27±4.23 | 49.45±7.83 |
| $t\bar{t}$ ($\sigma=6.7$ pb) | 20.54±1.58 | 22.70±1.74 | 50.62±3.86 | 93.86±7.14 |
| Total SM expectation | 34.02±3.39 | 38.41±3.96 | 70.89±6.69 | 143.31±13.09 |
| DATA | 30 | 42 | 73 | 145 |

| Events per 2000 pb$^{-1}$ vs Njet bins | | | | | |
|---|---|---|---|---|---|
| Source | 0j | 1j | $\geq$ 2j | H$_T$ | H$_T$, OS |
| WW | 100.19±10.63 | 28.43±3.45 | 10.70±1.90 | 7.09±1.22 | 6.81±1.17 |
| WZ | 8.06±0.70 | 8.41±0.62 | 3.19±0.45 | 2.42±0.39 | 1.59±0.26 |
| ZZ | 6.07±4.70 | 2.93±2.27 | 1.47±1.15 | 1.28±1.00 | 1.09±0.85 |
| W$\gamma$ | 19.13±5.09 | 5.53±1.57 | 1.54±0.59 | 0.17±0.18 | 0.17±0.18 |
| DY$\rightarrow\tau\tau$ | 2.69±0.43 | 12.87±2.28 | 9.32±2.39 | 5.51±1.07 | 5.26±1.02 |
| DY$\rightarrow ee+\mu\mu$ | 35.87±7.47 | 28.24±5.55 | 20.68±6.17 | 12.78±2.17 | 12.78±2.17 |
| Fakes | 51.59±13.87 | 61.32±17.25 | 51.20±14.29 | 35.66±10.11 | 21.75±6.33 |
| Total background | 223.60±28.32 | 147.73±22.59 | 98.10±18.65 | 64.91±11.26 | 49.45±7.83 |
| $t\bar{t}$ ($\sigma=6.7$ pb) | 0.47±0.05 | 12.56±0.97 | 99.86±7.60 | 96.31±7.33 | 93.86±7.14 |
| Total SM expectation | 224.07±28.35 | 160.30±23.19 | 197.96±24.10 | 161.22±15.70 | 143.31±13.09 |
| DATA | 239 | 152 | 200 | 161 | 145 |

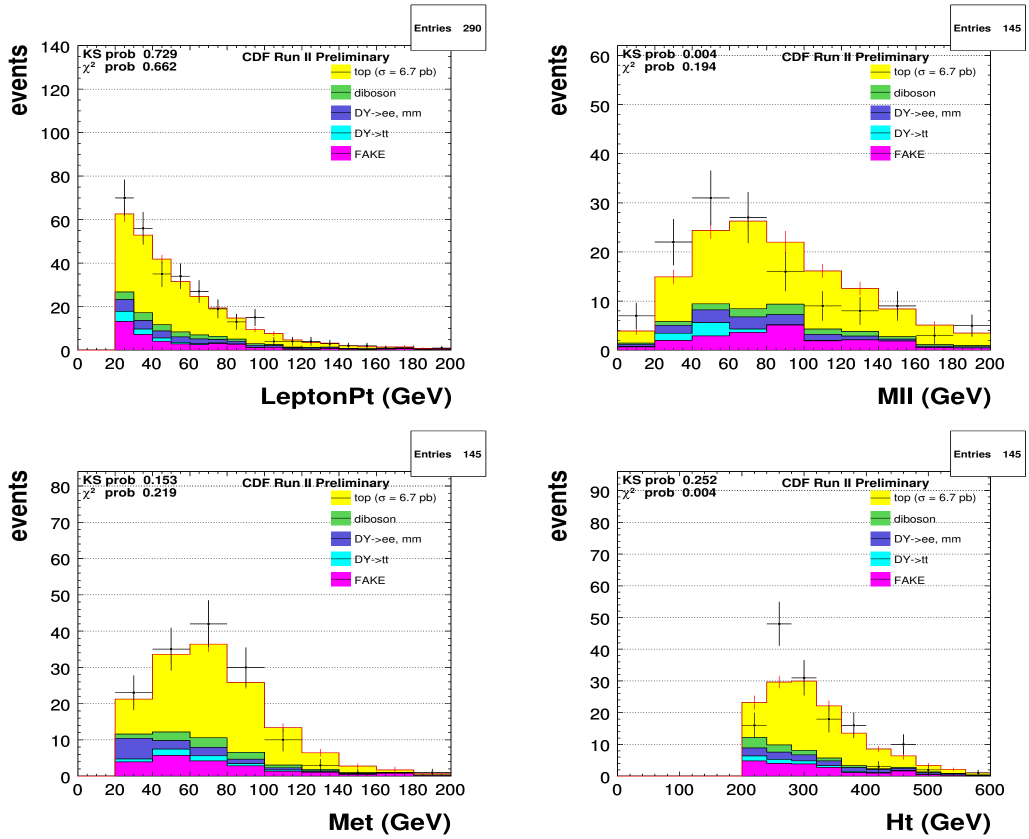


Figure 4.8: From top left to bottom right: background and top signal predictions, overlaid to data, for the lepton transverse energy spectrum, the dilepton invariant mass, $\not\!\!E_T$ and $H_T$ distributions in 2 fb$^{-1}$top DIL candidate events.

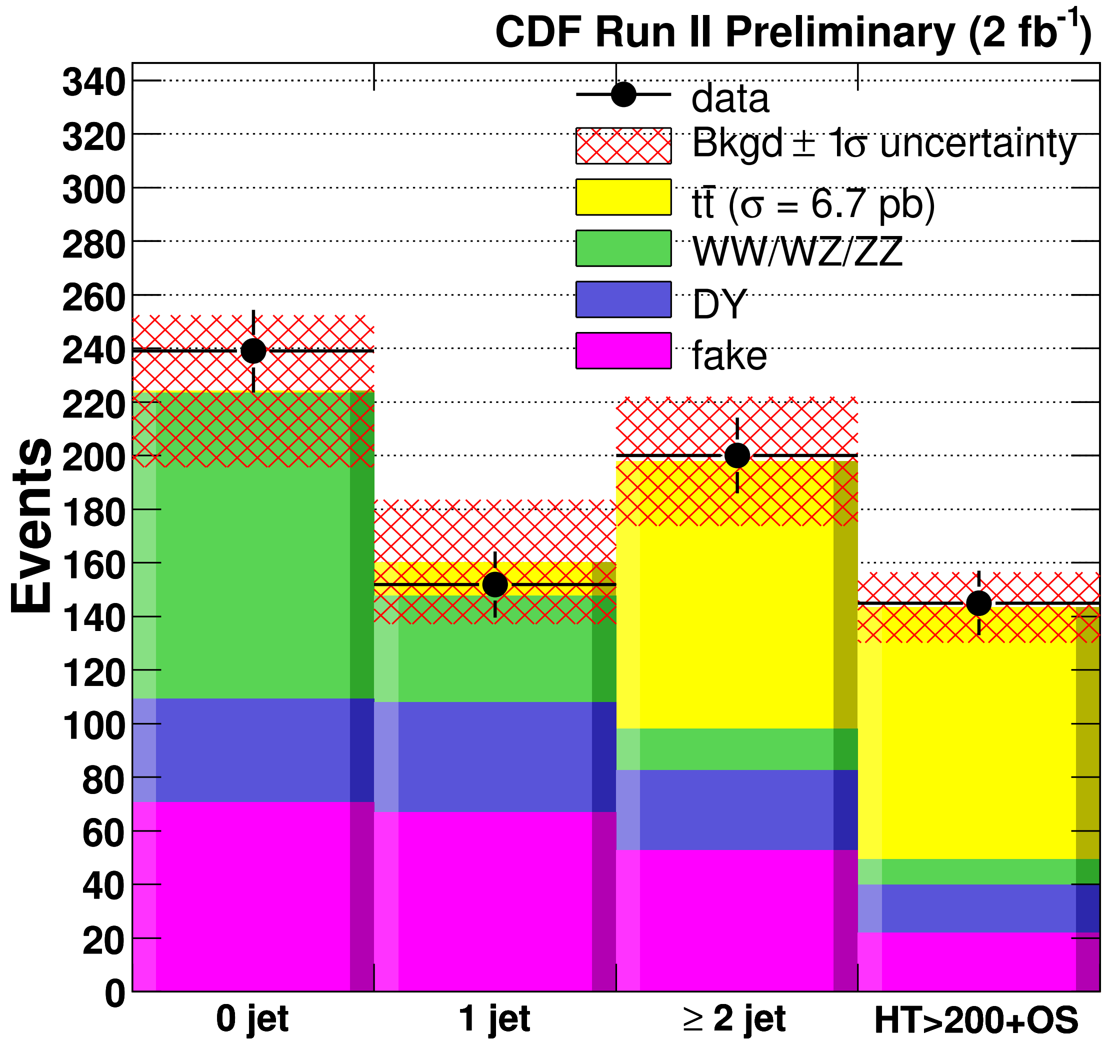


Figure 4.9: Background and signal composition of the Inclusive 2 fb$^{-1}$ DIL events vs jet multiplicity after the Z-veto, $\not\!\!E_T$ and L-cut have been applied.

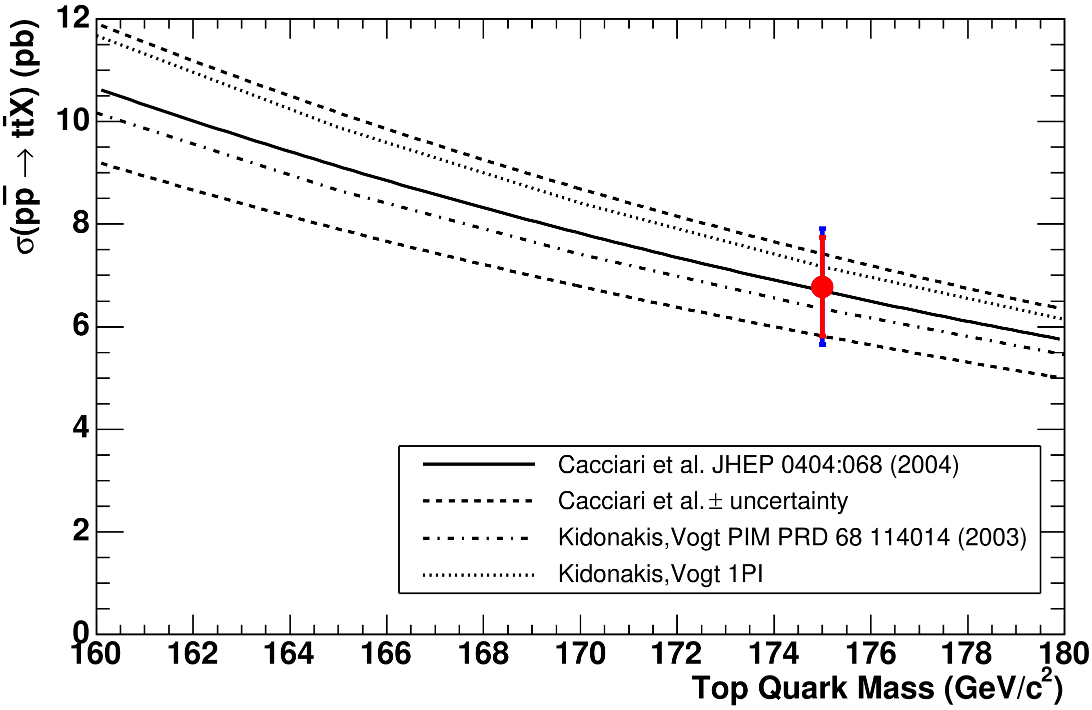


Figure 4.10: NLO calculations of $\sigma(p\bar{p} \to t\bar{t}X)$ [17] for $p\bar{p}$ collisions at $\sqrt{s}$=1.96 TeV as a function of top quark mass. The Point shows the measurement of this analysis.

# Chapter 5

# Identification of the Initial State of the Subprocesses

In $p\bar{p}$ collisions at $\sqrt{s} = 1.96$ TeV, $t\bar{t}$ pairs are produced dominantly through $q\bar{q}$ annihilation, while about 15% of $t\bar{t}$ pairs are predicted to be produced via gluon-fusion [14]. Because of uncertainties in the large-$x$ gluon luminosity, the prediction of this fraction has a large ambiguity and will change by up to a factor of 2 (from 10% to 20%). Hence, measurement of the gluon fusion fraction will give the knowledge of the gluon content of the proton at large values of $x$ as well as test for the perturbative QCD calculation of gluon fusion.

$t\bar{t}$ pair produced via gluon fusion has a different spin state from one via $q\bar{q}$ annihilation. This difference manifests itself efficiently as an azimuthal correlation of charged leptons in the $t\bar{t}$ dilepton channel [15]. If we assume $t\bar{t}$ pair production close to threshold, $t\bar{t}$ pair produced via gluon fusion and $q\bar{q}g$ annihilation is in the following spin state [16]:

$$\begin{aligned} gg &: J = 0, J_z = 0 \\ q\bar{q} &: J = 1, J_z = \pm 1 \ , \end{aligned}$$

where $z$ denotes the initial parton direction (i.e. nearly the beam direction).

Therefore, in the case of gluon fusion, the top quark and the anti-top quark tend to have the opposite spin on any quantize axis, while the aligned spin on the beam axis in the case of $q\bar{q}$ annihilation.

We utilize the difference in azimuthal correlation of charged leptons in the $t\bar{t}$ dilepton channel to distinguish $t\bar{t}$ pair produced via gluon fusion from $q\bar{q}$ annihilation.

The principle of $gg/q\bar{q}$ separation is described in Section 5.1.

In Section 5.2, we show expected $\Delta\phi$ distributions of signal and background, which we adopt in this analysis as discriminant of $gg$ from $q\bar{q}$, and in Section 5.3, we explain how we can extract the fraction of gluon fusion, and show the expected sensitivity for the measurement. In Section 5.4, we discuss possible systematics on the measurement. Finally, in Section 5.5, we display the result by applying our analysis method on 2.0 fb$^{-1}$ data, and we conclude in the last section.

## 5.1 Method to distinguish gluon fusion from $q\bar{q}$ annihilation

We define the azimuthal plane perpendicular to the the beam axis, and choose an axis on the azimuthal plane as the axis of quantization of the top and the anti-top quark spins. In this case, the spins of them tend to have the opposite direction for $t\bar{t}$ pair through $q\bar{q}$-fusion, while have no correlation for $q\bar{q}$ annihilation. (See Appendix A)

The top quark decays via $P$-violating weak interaction. Hence, the flight directions of decay products in $t \to Wb \to \ell\nu b$ are correlated with the top quark spin polarization [51]. In $t \to \ell^+\nu b$ decay, if we choose the flight direction of the charged lepton in the top rest frame as the axis of quantization of the top quark spin, the top quark spin is found to be aligned to the direction. (See Appendix B). Likewise, the anti-top quark spin is found to be aligned to the opposite direction of the charged lepton flight direction in the anti-top rest frame.

From the reason mentioned above, we choose the correlation between the charged lepton flight directions projected onto the azimuthal plane from the top quark and the anti-top quark to look at the difference of the spin correlation in $gg$ from one in $q\bar{q}$ in the $t\bar{t}$ dilepton channel.

For simplicity, we just look the flight direction of the charged leptons projected onto the azimuthal plane in the laboratory frame. The advantage of using the flight direction on the azimuthal plane is that the variable is invariant by boost of the beam direction. Since the top (anti-top) spins can be found to be the direction of the charged lepton flight direction in their rest frame, it is expected that better sensitivity can be achievable if we use the charged lepton flight direction in the top (anti-top) rest frame. However, in the dilepton channel, it is difficult to reconstruct the full kinematic variables in an event include missing two neutrinos.

The flight directions of the charged leptons on the azimuthal plane are affected by boost of the top (anti-top) $p_T$, but never by boost of the top (anti-top) $p_z$.

The variable we adapt is $\Delta\phi$, the angle between the charged leptons

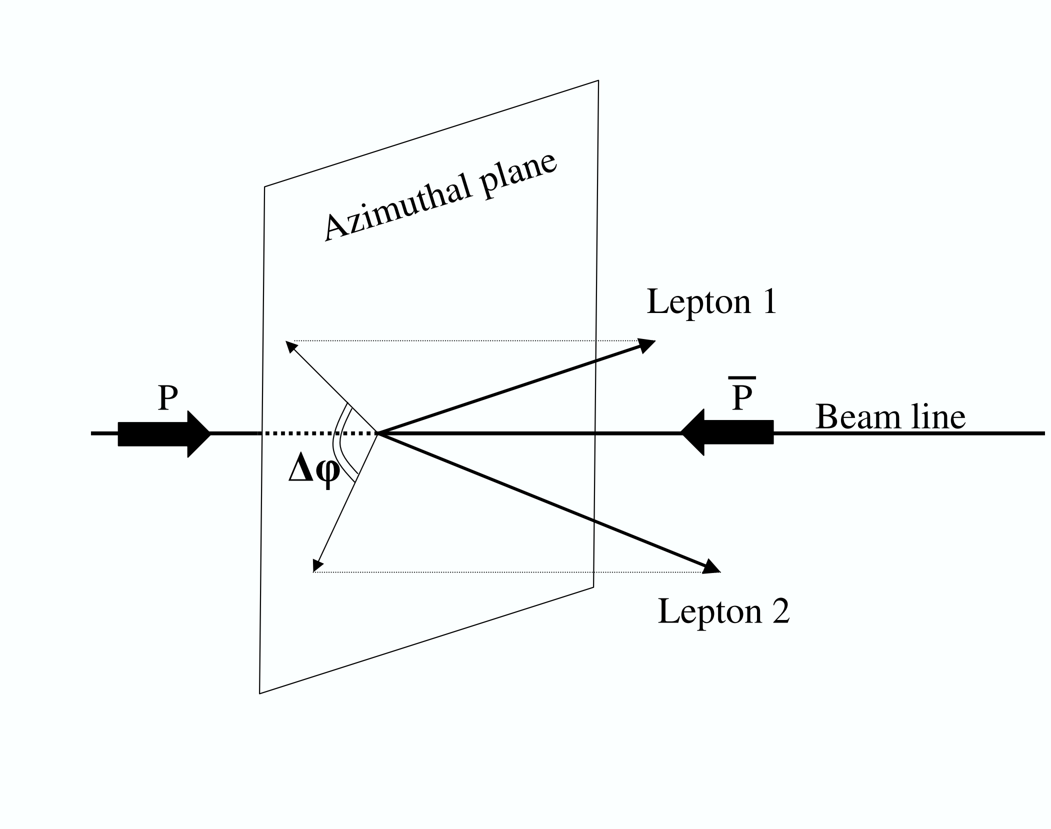


Figure 5.1: Schematic drawing of the definition of $\Delta\phi$. $\Delta\phi$ is defined as the angle between the charged leptons in the plane perpendicular to the beam axis.

projected on to the azimuthal plane perpendicular to the beam axis, which is illustrated in Fig.5.1. $\Delta\phi$ is defined within $0 \leq \Delta\phi \leq \pi$.

The dilepton events of $t\bar{t}$ using HERWIG event generator in which the spin correlations are taken into account are used. We separate gluon fusion events from $q\bar{q}$ annihilation events based on the initial parton information. As mentioned above, in gluon fusion, $t\bar{t}$ spins tend to be aligned to the opposite direction. This means the charged lepton tend to point to the same direction in the top (anti-top) rest frame. So we expect more events near $\Delta\phi = 0$ and less events near $\Delta\phi = \pi$. Including the consideration that the charged lepton flight directions in the laboratory frame are affected by the top (anti-top) boost and $t$ and $\bar{t}$ fly to the almost oppositely direction on the azimuthal plane, the actual $\Delta\phi$ we observe is shifted toward $\Delta\phi = \pi$. Consequently the distribution of $\Delta\phi$ in the gluon fusion event rather comes to nearly flat.

On the other hand, in $q\bar{q}$ annihilation, $t$ and $\bar{t}$ spins are not correlated on the azimuthal plane, and we expected the charged lepton flight directions on the azimuthal plane are random in the top (anti-top) rest frame. If we neglect $p_T$ of the top and anti-top quark, we expect the flat $\Delta\phi$ distribution. After the consideration of $t$ and $\bar{t}$ boosts, we obtain a lopsided $\Delta\phi$ distribution toward $\Delta\phi = \pi$.

The variable $\Delta\phi$ become more sensitive for the $gg/q\bar{q}$ separation with the charged lepton in the central region than one in the plug region, since we look at the direction projected on the azimuthal plane. Therefore, the geometrical acceptance on the charged lepton requiring at least one charged lepton in the central region, enhances the separation power.

Figure 5.2 shows the distributions of $\Delta\phi$ in gluon fusion (left) and $q\bar{q}$ annihilation (right) after several selections on the kinematic variables. The following selections are applied on events generated by HERWIG :

- Dilepton e-e, $\mu$-$\mu$, or e-$\mu$ channel
- Pseudorapidity of leptons: $|\eta_\ell| < 1.0$
- Transverse energy of leptons: $E_T > 20$ GeV
- Pseudorapidity of $b$-quarks: $|\eta_b| < 2.0$
- Transverse energy of $b$-quarks: $E_T > 15$ GeV

The distributions poorly depend on the selections on $b$-quark. On the other hand, the selections on $\eta_\ell$ and $p_T(\ell)$ of leptons enhance the discrepancies between $gg$ and $q\bar{q}$ distributions, since these selections prefer the leptons

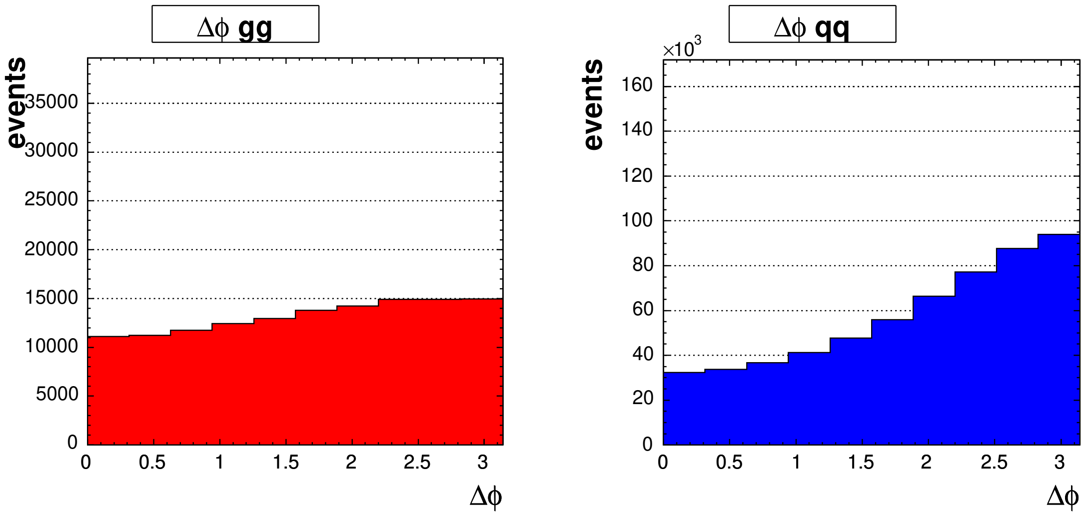


Figure 5.2: The distributions of $\Delta\phi$ in gluon fusion (left) and $q\bar{q}$ annihilation (right) after several selections on the kinematic variables. See the text on the detail of selections.

flying perpendicular to the beam axis, which have better analyzing power to the top spin on the azimuthal plane.

We also studied other variables as a candidate of discriminant for $gg/q\bar{q}$ separation. One candidate is the angle between the flight direction of $\ell^+$ in the $t$ rest frame and the flight direction of $\ell^-$ in the $\bar{t}$ rest frame. In the case of gluon fusion at threshold, this is the best variable because the spin state of $t\bar{t}$ is in ${}^1S_0$. We compared the separation power by this variable with $\Delta\phi$, and found gives slightly better separation power. However, the full kinematical reconstruction is required to obtain the flight direction of the leptons in the top rest frame. Therefore this variable practically gives poorer separation power than $\Delta\phi$.

The merits of $\Delta\phi$ are summarized below:

- $\Delta\phi$ is invariant on the beam direction.
- $\Delta\phi$ is hardly affected by reconstruction smearing, since only the lepton flight directions in the laboratory frame are used.
- $\Delta\phi$ is free from jet energy scale uncertainty.

We conclude $\Delta\phi$ is reliable as well as suitable for the separation of $gg$ from $q\bar{q}$.

## 5.2 Signal and Background templates

Events selection and using data region is exact same as cross section measurements. The strategy of the gluon fusion measurement is that we fit composition of expected $\Delta\phi$ distribution of $gg$, $q\bar{q}$, and background with one of data supposing $gg$ fraction as a free fit parameter. Therefore, we introduce the expected $\Delta\phi$ distributions (templates) of $gg$, $q\bar{q}$, and each background process in this section.

### 5.2.1 Gluon fusion and $q\bar{q}$ annihilation

To obtain $\Delta\phi$ in the gluon fusion and $q\bar{q}$ annihilation, we use $t\bar{t}$ pair production Monte Carlo simulation sample which is generated by HERWIG event generator and CDF detector simulator with top quark mass $M_t = 175$ GeV. In this simulation sample, CTEQ5L set is used as the parton distribution function of proton and anti-proton, and we find about 5% of the sample comes from gluon fusion and the rest comes from $q\bar{q}$ annihilation according to initial state partons.

We separate $t\bar{t}$ events via gluon fusion from $q\bar{q}$ annihilation, and obtain $\Delta\phi$ distributions of $gg$ and $q\bar{q}$ events after DIL selection, separately. Figure 5.3 shows the distributions of $gg$ (right) and $q\bar{q}$ (left). The histograms are fitted with the following function:

$$f_i = (3 - P_i^0 \cos(\Delta\phi) + P_i^1 \cos(2\Delta\phi) + P_i^2 \cos(3\Delta\phi))/3\pi, \qquad (5.1)$$

where $P_i^{(n)}$s indicate fitting parameters and the suffix $i$ represent the process, i.e. $i = gg, q\bar{q}$ here. We adopt the function composed with cosine since $\Delta\phi$ distribution should be periodic. The solid curve in the figure indicate the best fit results.

### 5.2.2 Background

We make $\Delta\phi$ distribution of each background process separately.

For diboson ($WW$, $WZ$, and $ZZ$) events and $Z \to \tau\tau$ events, we rely on MC simulation samples which are generated with PYTHIA [48] event generator.

For Drell-Yan ($Z \to ee, \mu\mu$) events, we also rely on MC simulation samples, but which are generated with Alpgen event generator.

For $W\gamma$ events, we ignore the background from this process, since the contribution from $W\gamma$ to background are negligibly small.

For fake events, i.e. one lepton with jets events where one of jets is misidentified as another lepton, we use a real event which contains a lepton

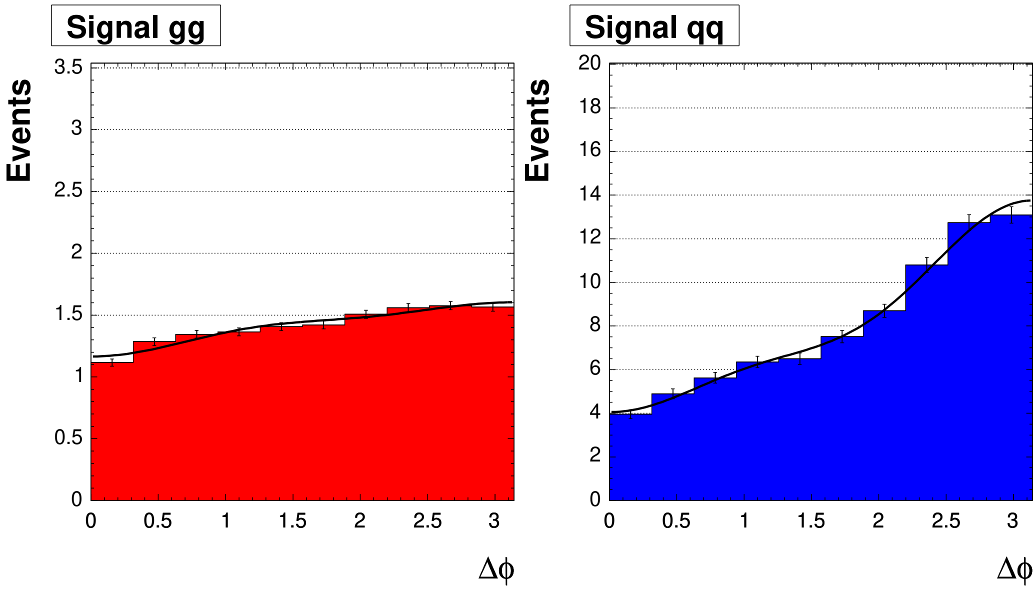


Figure 5.3: The distributions of $\Delta\phi$ of gluon fusion (left) and $q\bar{q}$ annihilation (right). The total number in each histogram is normalized to expectation assuming 6.7 pb $t\bar{t}$ cross section. The error bars originate from Monte Carlo statistics. The solid curves in the figure indicate the fit results with the function in the text.

Table 5.1: The fit result of parameters, together with $\chi^2$/ndf.

| Source | $P^0$ | $P^1$ | $P^2$ | $\chi^2$/ndf |
|---|---|---|---|---|
| $gg$ | $0.39 \pm 0.03$ | $0.06 \pm 0.06$ | $0.07 \pm 0.07$ | 13.7/7 |
| $q\bar{q}$ | $1.57 \pm 0.05$ | $-0.33 \pm 0.05$ | $0.25 \pm 0.05$ | 6.7/7 |
| background | $0.85 \pm 0.11$ | $-0.14 \pm 0.11$ | $-0.07 \pm 0.11$ | 11.6/7 |

and at least one "fakeable" jet and make one of the jets in an events forcibly to be mis-reconstructed as an electron or a muon. In this case, the event weight is not unit, but is adopted to be their fake rate.

$\Delta\phi$ histograms of background above are summed up with weights according to their expected number of events in Table 4.19. Then we fit the distribution to Eq. (5.1).

We summarize the fit result of parameters in Table 5.2. $\chi^2$/ndf of the fits are in the table as well.

### 5.2.3 Control region as a cross check

As a cross check of $\Delta\phi$ distributions of background, we use events in a control region. The selection for the control region is defined as same as DIL selection but requirement of zero or one jet, no requirement for $H_T$, and no requirement for opposite charge in lepton pair.

Figure 5.5 shows $\Delta\phi$ distribution of the event in the control region with $N_{\text{jets}} = 0$ (left) and $N_{\text{jets}} = 1$ (right). We can see a good agreement between observed distribution and the prediction.

## 5.3 Determination of $gg$ Fraction

We define an unbinned likelihood as follows:

$$\begin{aligned} \mathcal{L}(\mathcal{F}_{gg}, n_{\text{s}}) &\equiv \prod_i \frac{n_{\text{s}} f_{t\bar{t}}(\Delta\phi_i; \mathcal{F}_{gg}) + n_{\text{b}} f_{\text{b}}(\Delta\phi_i)}{n_{\text{s}} + n_{\text{b}}} \\ f_{t\bar{t}}(\Delta\phi_i; \mathcal{F}_{gg}) &\equiv \frac{\mathcal{F}_{gg} f_{gg}(\Delta\phi_i) + (1 - \mathcal{F}_{gg}) f_{q\bar{q}}(\Delta\phi_i)}{\mathcal{F}_{gg} + (1 - \mathcal{F}_{gg})}\ , \end{aligned} \tag{5.2}$$

where $\mathcal{F}_{gg}$ and $n_{\text{s}}$ are assumed $gg$ fraction and number of $t\bar{t}$ events, respectively. $\Delta\phi_i$ denotes $\Delta\phi$ observed in the $i$-th candidate event. $N$ is the total number of candidate events, and $n_{\text{b}}$ indicates the expected number of

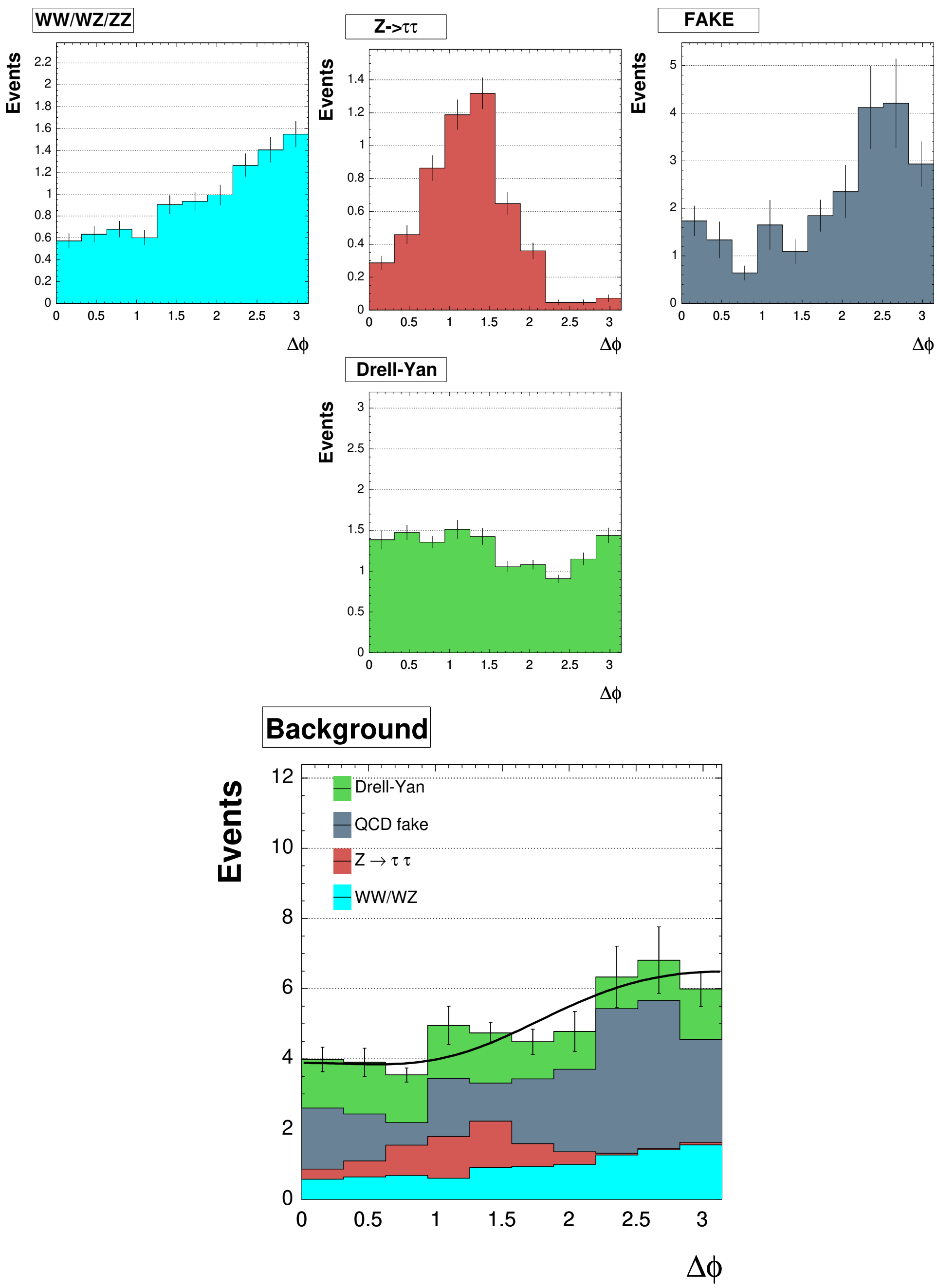


Figure 5.4: The distributions of $\Delta\phi$ of (a) diboson ($WW$, $WZ$, and $ZZ$) processes, (b) $Z \to \tau\tau$, (c) Drell-Yan ($Z \to ee, \mu\mu$), (d) fake events, and (e) all background events from above four components. The total number in each histogram is normalized to each expected number at 2.0 fb$^{-1}$ data. The error bars originate from statistics. The solid curve in the figure (e) indicates the fit results to the function in the text.

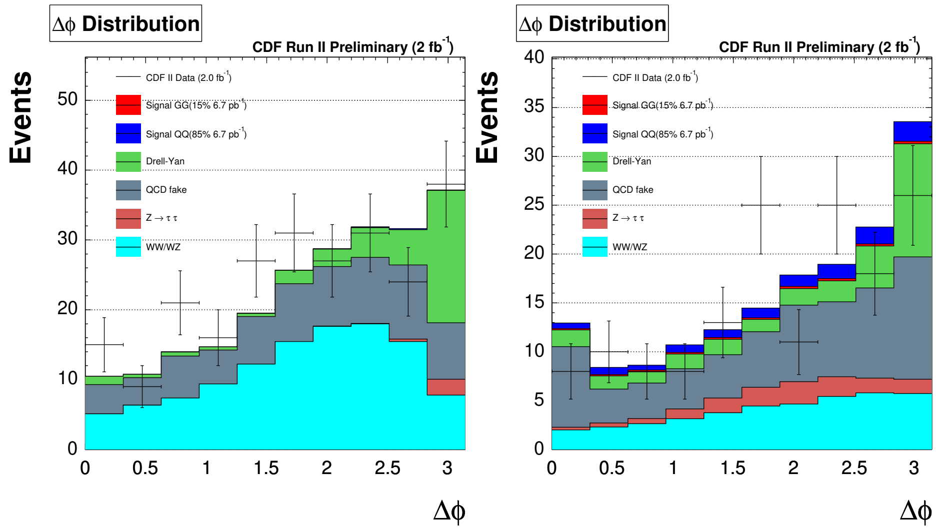


Figure 5.5: $\Delta\phi$ distribution of the event in the control region with $N_{\text{jets}} = 0$ (left) and $N_{\text{jets}} = 1$ (right)

background events. The functions $f_{gg}$, $f_{q\bar{q}}$, and $f_{\mathrm{b}}$ are probability density of $\Delta\phi$ for $gg$, $q\bar{q}$, and background events, which are obtained in Section 5.2, respectively.

We take $\mathcal{F}_{gg}$ which maximizes this likelihood as the observed $gg$ fraction, and describe this as $\mathcal{F}_{gg}^{\text{measured}}$ hereafter.

### 5.3.1 Sensitivity study with pseudo-experiments

Next, we perform pseudo-experiments to look how an observed $\mathcal{F}_{gg}$ distributes for the assumption of true $\mathcal{F}_{gg}$.

In each pseudo-experiment, we generate $N$ random numbers distribute the probability density function $n_{\mathrm{s}}\left\{\mathcal{F}_{gg}f_{gg} + (1-\mathcal{F}_{gg})\, f_{q\bar{q}}\right\} + n_{\mathrm{b}} f_{\mathrm{b}}$, where we assume $n_{\mathrm{b}}$ is the center value of estimated number of background events, and $n_{\mathrm{s}}$ is $N - n_{\mathrm{b}}$. The uncertainty in $n_{\mathrm{b}}$ is considered later as a systematic error.

We perform 10,000 pesudo-experiments for each assumption of $\mathcal{F}_{gg}$, and obtain the observed $\Delta\phi$ as the best fit of the likelihood function Eq. (5.2) from each pesudo-experiment. Figure 5.6 shows an example of the resultant distribution of the observed $\mathcal{F}_{gg}$ for $\mathcal{F}_{gg} = 0.15$ and $N = 145$. The solid curve in the figure indicates Gaussian fitting of the histogram. We extract the mean value and sigma of the distribution from Gaussian fitting for each assumed $\mathcal{F}_{gg}$. Figure 5.7 shows the mean value of the observed $\Delta\phi$ distribution (left) and residual (right), and its sigma(bottom), as a function of the

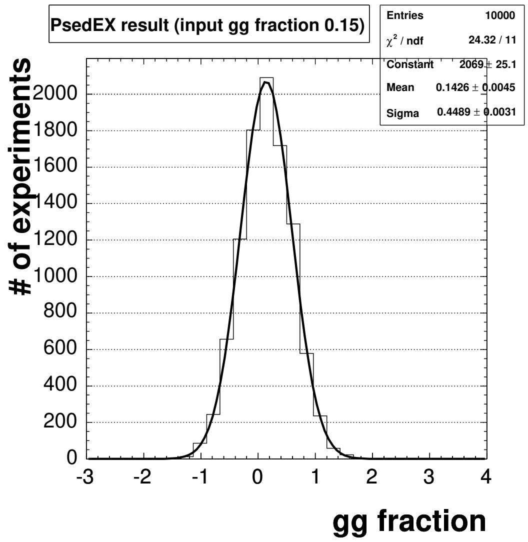


Figure 5.6: The distributions of the observed $\mathcal{F}_{gg}$ by the fitting pseudo-experiment distributions. The input value for the pseudo-experiment is $\mathcal{F}_{gg} = 0.15$ and the number of candidate events is $N = 145$. The solid curve shows the results of a Gaussian fit of the histogram.

input $\mathcal{F}_{gg}$ of the pseudo-experiments. The figure indicates that the measurement has a good linearity of response for the input $\mathcal{F}_{gg}$ and sensitivity of the measurement is about 44.8% almost independent of input $\mathcal{F}_{gg}$.

### 5.3.2 Feldman-Cousins confidence interval

To set confidence interval on $\mathcal{F}_{gg}$ considering physical region of $0 \leq \mathcal{F}_{gg} \leq 1$, we adopt Feldman-Cousins' construction of confidence belt [53].

As a result of pseudo-experiments, we found that distributions of $\mathcal{F}_{gg}^{\mathrm{measured}}$ for each input true $\mathcal{F}_{gg}$ can be approximated by Gaussian distribution, and obtained mean and sigma of the distributions as a function of input $\mathcal{F}_{gg}$ as Fig. 5.7 shows. Suppose these distribution as probability density $P(\mathcal{F}_{gg}^{\mathrm{measured}}|\mathcal{F}_{gg}^{\mathrm{true}})$, then we can find $x_1$ and $x_2$ for each $\mathcal{F}_{gg}^{\mathrm{true}}$ as:

$$\begin{aligned} \int_{x_1}^{x_2} P(x|\mathcal{F}_{gg}^{\mathrm{true}})dx &= \mathrm{CL} \\ R(x_1) &= R(x_2) \\ R(x) &\equiv \frac{P(x|\mathcal{F}_{gg}^{\mathrm{true}})}{P(x|\mathcal{F}_{gg}^{\mathrm{best}})} . \end{aligned} \tag{5.3}$$

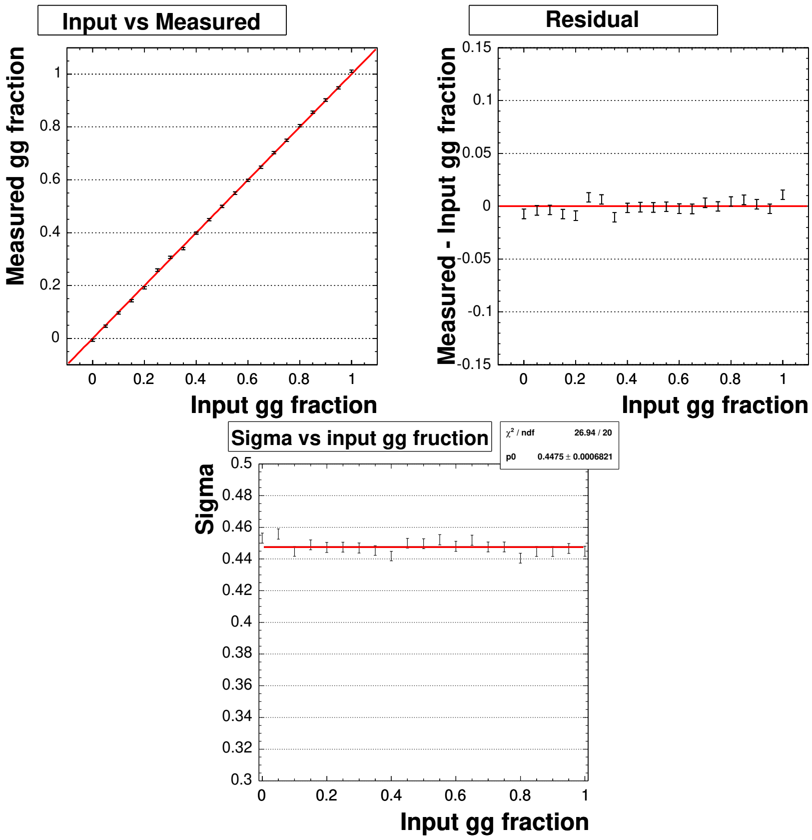


Figure 5.7: The mean value of the observed $\Delta\phi$ distribution (left) and its sigma (right) as a function of the input $\mathcal{F}_{gg}$ of the pseudo-experiments with $N = 145$.

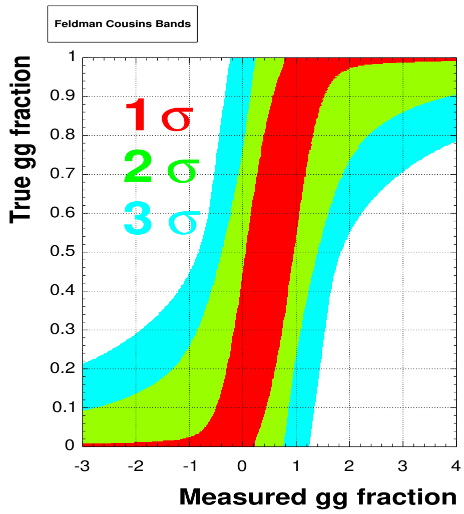


Figure 5.8: Confidence belt based on Feldman-Cousins' ordering principle. The region surrounded by the broken curves corresponds $1\sigma$, $2\sigma$, $3\sigma$ intervals. No systematic error is considered on these intervals.

Here $\mathcal{F}_{gg}^{\text{best}}$ is the physically allowed value of $\mathcal{F}_{gg}$ for which $P(x|\mathcal{F}_{gg})$ is maximum. CL in the equation means the confidence level we consider.

The region $x_1 \leq \mathcal{F}_{gg}^{\text{measured}} \leq x_2$ as a function of $\mathcal{F}_{gg}^{\text{true}}$ constructs the confidence belt shown in Fig. 5.8.

## 5.4 Systematic uncertainties

We discuss here about possible systematic uncertainties and integrate them into F-C confidence belt. We consider the following systematics source:

- Shapes of $\Delta\phi$ templates and Expected number of background.
- Acceptance ratio of $gg$ to $q\bar{q}$.
- Estimation method of systematic uncertainty.
- Theoretical calculation of $t\bar{t}$ pair production matrix element.
- Initial/Final state radiation.
- Parton distribution function.
- Jet energy scale.

- Other systematics

### 5.4.1 $\Delta\phi$ templates and expected number of background

The $\Delta\phi$ distributions of $gg$, $q\bar{q}$, and background are obtained by fitting the histograms to the function Eq. (5.1) in Section 5.2.

And the expected number of background is used in the likelihood function defined in Eq. (5.2). Consequently uncertainty in expected number of background is one of systematics sources.

In order to look the effect by uncertainties of the $\Delta\phi$ template of $gg$, $q\bar{q}$ and background, we generate 10,000 sets of pseudo-data with each for $\mathcal{F}_{gg}^{\text{true}}$, where each bin's uncertainty of statistics for the shape systematics due to MC statistics, and each background number. Generally we use function that fitted results of each $\Delta\phi$ template to make pseudo data, but in this systematic estimation we use $gg$ fusion, $q\bar{q}$ annihilation and each background histogram.

Then, we perform the measurement of $\mathcal{F}_{gg}^{\text{measured}}$ on the assumption of center values for expected number of background, and look how much shift in sigma of $\mathcal{F}_{gg}^{\text{measured}}$ is observed. We take a quadratic increment of sigma as a systematic uncertainty. We didn't see any obvious dependence on $\mathcal{F}_{gg}^{\text{true}}$, so quote 5.0% due to $\Delta\phi$ templates and Expected number of background.

### 5.4.2 Acceptance ratio of $gg$ to $q\bar{q}$

Acceptance ratio of $gg$ to $q\bar{q}$, $\mathcal{R} = A_{gg}/A_{q\bar{q}}$, is a direct function to the $\mathcal{F}_{gg}^{\text{measured}}$. Consequently uncertainty in $\mathcal{R}$ is one of systematics sources. We used $t\bar{t}$ Monte Carlo data which is generated by HERWIG event generator and CDF detector simulation to obtain the acceptance ratio, $\mathcal{R}$, and found $\mathcal{R} = 1.013 \pm 0.014$. We didn't see any obvious difference between $gg$ and $q\bar{q}$, so just quote the 1.4% systematic uncertainty due to uncertainties in $\mathcal{R}$.

Because we estimate $gg$ fusion fraction, we don't need worry about total acceptance shift due to systematic sample. But if acceptance ratio $gg$ to $q\bar{q}$ have a shift in systematic sample, we should add that difference to systematic uncertainty. And we add this effect to shape systematic estimation.

We can't find any systematic difference on $\mathcal{R} = A_{gg}/A_{q\bar{q}}$, but statistic uncertainty from MC sample is big. Our$t\bar{t}$dilepton channel's signal acceptance is about 1% with branching ratio and $gg$ fusion's fraction of CTEQ5L is only 5%, so we have only 500 events in 1M events MC sample.

Table 5.2: $\mathcal{R} = A_{gg}/A_{q\bar{q}}$ difference on ISR,FSR, and top mass systematic sample

| Source | Acceptance ratio($\mathcal{R} = A_{gg}/A_{q\bar{q}}$) |
|---|---|
| Default HERWIG | $\mathcal{R} = 1.01 \pm 0.01$ |
| NLO vs LO | $\mathcal{R} = 0.97$ |
| ISR more | $\mathcal{R} = 1.07 \pm 0.05$ |
| ISR less | $\mathcal{R} = 0.99 \pm 0.05$ |
| FSR more | $\mathcal{R} = 1.02 \pm 0.05$ |
| FSR less | $\mathcal{R} = 1.03 \pm 0.05$ |
| ISRFSR more | $\mathcal{R} = 1.05 \pm 0.04$ |
| ISRFSR less | $\mathcal{R} = 0.98 \pm 0.03$ |
| top mass 170GeV | $\mathcal{R} = 1.03 \pm 0.05$ |
| top mass 180GeV | $\mathcal{R} = 1.08 \pm 0.05$ |

### 5.4.3 Estimation Method of Systematic Uncertainty

We use generator level information, i.e. hepg information, for the $\Delta\phi$ distribution of systematic sample to get high statistics. And also, we use below the equation for the $\Delta\phi$ distribution of systematic sample.

$$f_i^{\text{Systematic}}(\Delta\phi) \equiv \frac{f_i^{\text{Systematic,hepg}}(\Delta\phi)}{f_i^{\text{Default,hepg}}(\Delta\phi)} f_i^{\text{Default,FullSim}}(\Delta\phi)$$

Basically difference between hepg and full simulation get cancel out. But if this difference is change between $gg$ fusion and $q\bar{q}$ annihilation by systematic source, we should consider about that difference. But we don't have enough statistics on systematics sample to look this difference. Therefore we add difference between hepg and full simulation as a systematic uncertainty due to estimation method of systematic uncertainty. Figure 5.9 shows $\Delta\phi$ distribution using hepg information(sold) and full simulation(dotted). We generate 10,000 sets of pseudo-data in each $\mathcal{F}_{gg}^{\text{true}}$, where $\Delta\phi$ templates of $q\bar{q}$ and $q\bar{q}$ are changed to the templates obtained by the weighted MC method on the difference between hepg and full simulation, and look how much shift in $\mathcal{F}_{gg}^{\text{measured}}$ is observed. Figure 5.10 shows resulting shifts. Systematics uncertainty due to the difference between hepg and full simulation is

$$\text{SYST}_{\text{method}} = \pm 0.02$$

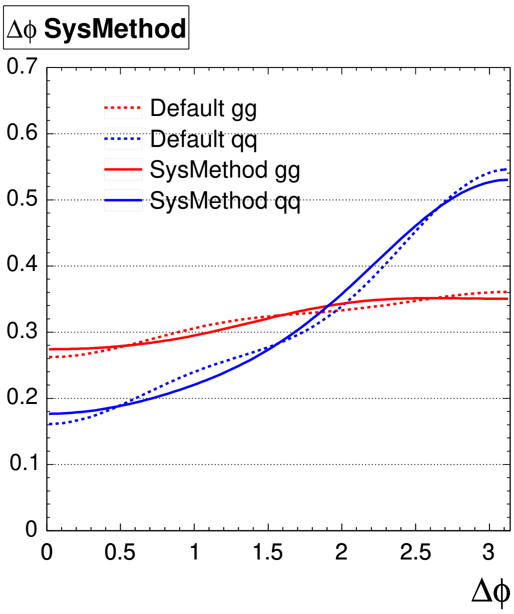


Figure 5.9: $\Delta\phi$ distributions of hepg information (solid) with full simulation of default HERWIG (dotted).

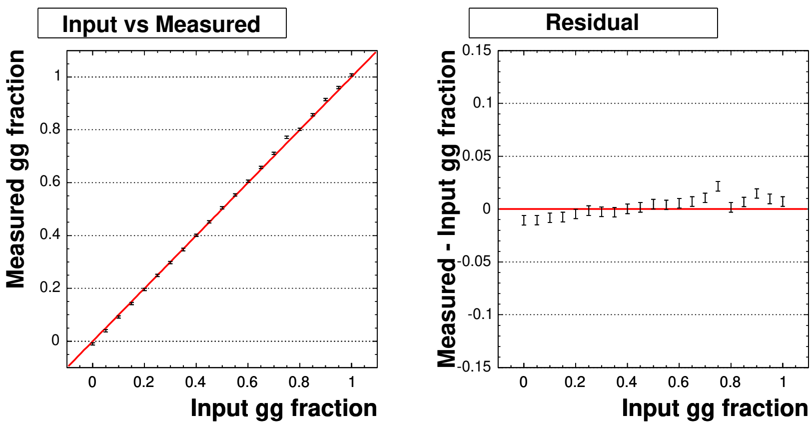


Figure 5.10: Linearity and residual plot of input $gg$ vs measured $gg$ fraction for systematic uncertainty for estimation method.

### 5.4.4 Theoretical calculation of $t\bar{t}$ pair production matrix element

In this analysis, we rely on the matrix elements of $gg \to t\bar{t}$ and $q\bar{q} \to t\bar{t}$ in HERWIG event generator where LO $t\bar{t}$ matrix element with the spin correlations are taken into account. One could find the effect of NLO calculation of the matrix elements in Ref [54].

We examine the effect of NLO matrix elements for $\Delta\phi$ templates of $gg$ and $q\bar{q}$ using MC@NLO version 3.3 event generator [55]. MC@NLO takes the spin correlation in $t\bar{t}$ into account correctly since this version.

Because leptons are well reconstructed, especially in their direction, $\Delta\phi$ is hardly affected by smearing in the reconstruction. In addition, $\Delta\phi$ distributions in Fig. 5.2, which are obtained from our toy Monte Carlo events (just event generator + several simple selections on the final state partons described in Section 5.1), well reproduce the distributions from full detector simulated events, which are shown in Fig. 5.3. Therefore, we postulate that the ratio of $\Delta\phi$ distributions of our toy MC events is applicable to distributions of the full detector simulated events, i.e. to obtain $\Delta\phi$ templates, we don't need full detector simulation, but generator level events are enough.

Here we obtain the ratio of $\Delta\phi$ probability density function by MC@NLO ($f_i^{\mathrm{NLO,hepg}}(\Delta\phi)$, $i = gg, q\bar{q}$) to by HERWIG ($f_i^{\mathrm{LO,hepg}}(\Delta\phi)$), and apply the ratio to the default templates $f_i(\Delta\phi)$ to infer templates by MC@NLO ($f_i^{\mathrm{NLO}}(\Delta\phi)$), i.e.

$$f_i^{\mathrm{NLO}}(\Delta\phi) \equiv \frac{f_i^{\mathrm{NLO,hepg}}(\Delta\phi)}{f_i^{\mathrm{LO,hepg}}(\Delta\phi)} f_i(\Delta\phi)$$

Figure 5.11 shows distribution of $f_i^{\mathrm{NLO}}(\Delta\phi)$(solid), with HERWIG distribution(dotted). We generate 10,000 sets of pseudo-data in each $\mathcal{F}_{gg}^{\mathrm{true}}$, where $\Delta\phi$ templates of $q\bar{q}$ and $q\bar{q}$ are changed to $f_i^{\mathrm{NLO}}(\Delta\phi)$, respectively. Then, we perform the measurement of $\mathcal{F}_{gg}^{\mathrm{measured}}$ on the assumption of the default $\Delta\phi$ templates, and look how much shift in $\mathcal{F}_{gg}^{\mathrm{measured}}$ is observed. Figure 5.12 shows resulting shifts. We see obvious dependence on $\mathcal{F}_{gg}^{\mathrm{true}}$, so we quote the asymmetric systematics uncertainty of linear function. Systematics function due to NLO effect of the $t\bar{t}$ production matrix elements is

$$\mathrm{SYST}_{\mathrm{MC@NLO}} = 0.032 \times \mathcal{F}_{\mathrm{gg}}^2 + 0.080 \times \mathcal{F}_{\mathrm{gg}} + 0.008$$

### 5.4.5 ISR/FSR

Differences due to QCD initial and final state radiations (ISR and FSR) are estimated using specially generated PYTHIA samples in which the QCD

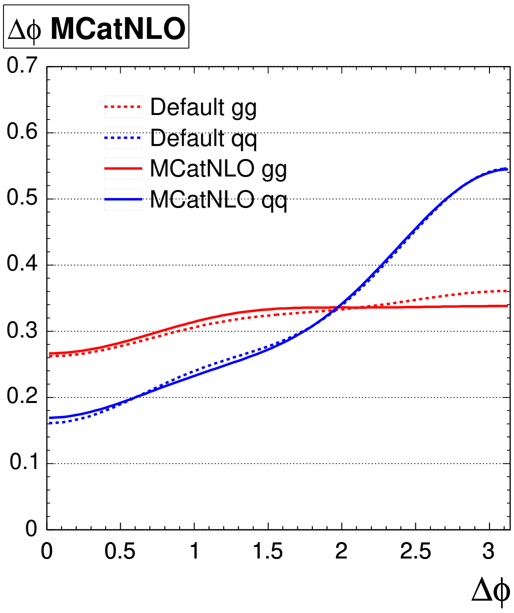


Figure 5.11: $\Delta\phi$ distributions of the toy MC events of $gg$ and $q\bar{q}$ generated by MC@NLO 3.3 event generator. The solid curves indicate the best fit results of the histograms. The broken curves indicate the fit results corresponding to $\Delta\phi$ distributions by HERWIG event generator.

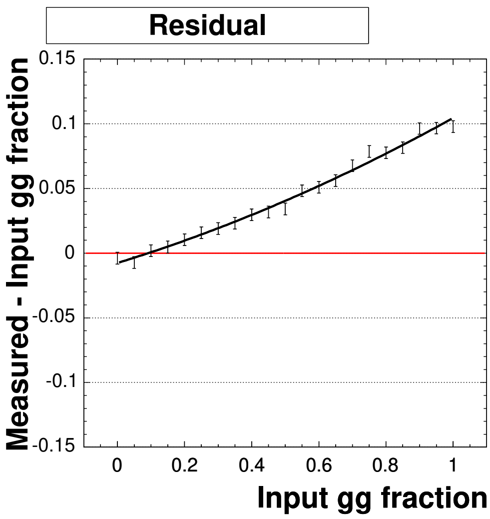


Figure 5.12: Residual plot of input $gg$ vs measured $gg$ fraction for systematic uncertainty of Theoretical calculation of $t\bar{t}$ pair production matrix element.

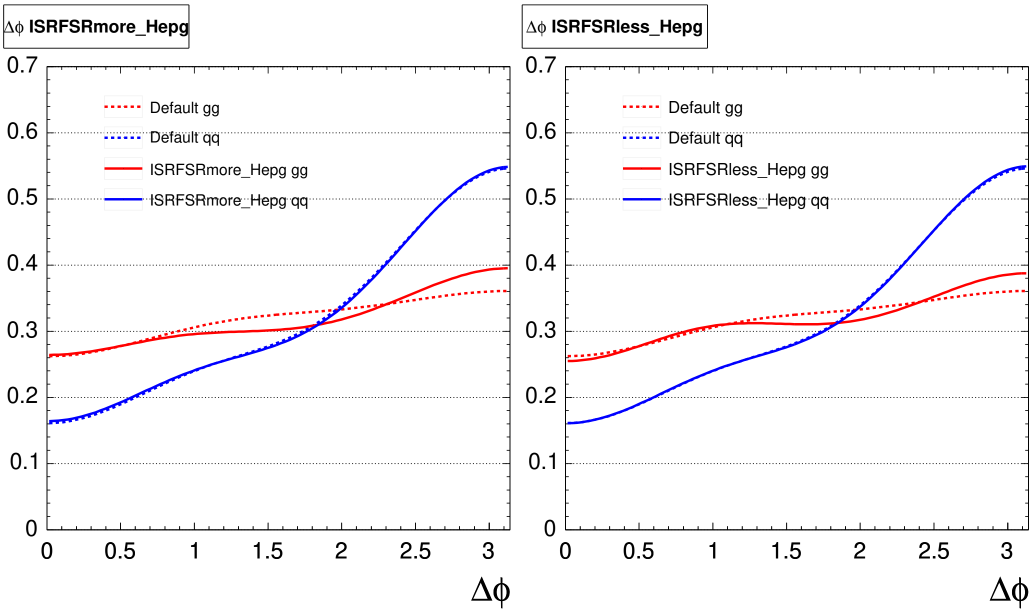


Figure 5.13: $\Delta\phi$ distributions of $f_i^{\rm more}(\Delta\phi)$(left solid) and $f_i^{\rm less}(\Delta\phi)$(right solid). with default HERWIG(dotted).

parameters for the parton shower evolution are varied based on the studies of the CDF Drell-Yan dataand recommendations from the authors of PYTHIA. Only difference of acceptance ratio of $gg$ to $q\bar{q}$ is considered in Section 5.4.2.

For ISR/FSR uncertainty, if a gluon is emitted in initial state of $t\bar{t}$ state, the $t\bar{t}$ system will have extra $p_T$, and $\Delta\phi$ is distorted. Therefore, ISR uncertainty may affect $gg/q\bar{q}$ templates. We used hepg information of itoprk and itoprl of more and less ISR/FSR sample. A $t\bar{t}$ event generated by PYTHIA doesn't have the correct spin correlation, but we are interested only in the distortion on a $\Delta\phi$ distribution caused by ISR/FSR uncertainty. Therefore we obtain the ratio of $\Delta\phi$ from more or less ISR/FSR sample to one from the sample with default parameters, and apply the ratio to the default $gg/q\bar{q}$ templates to infer templates with more or less ISR/FSR.

Here we obtain the ratio of $\Delta\phi$ probability density function with more or less ISR/FSR settings to default settings and apply the ratio to the default templates to get new templates for more or less ISR/FSR settings ($f_i^{\rm more}(\Delta\phi)$ and $f_i^{\rm less}(\Delta\phi)$). Figure 5.13 shows $f_i^{\rm more}(\Delta\phi)$(left solid) and $f_i^{\rm less}(\Delta\phi)$(right solid) and default HERWIG distribution(dotted).

Then, we generate 10,000 sets of pseudo-data in each $\mathcal{F}_{gg}^{\rm true}$, where $\Delta\phi$ templates of $q\bar{q}$ and $q\bar{q}$ are changed to $f_i^{\rm more}(\Delta\phi)$ and $f_i^{\rm less}(\Delta\phi)$, respectively. Next, we perform the measurement of $\mathcal{F}_{gg}^{\rm measured}$ on the assumption of the

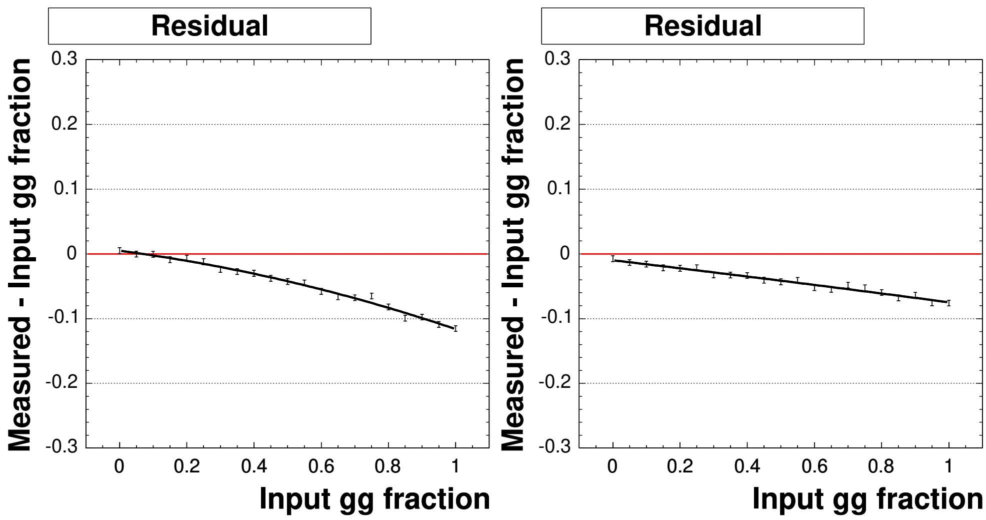


Figure 5.14: Residual plot of input $gg$ vs measured $gg$ fraction for systematic uncertainty of ISR/FSR more(left), and ISR/FSR less(right).

default $\Delta\phi$ templates, and look how much shift in $\mathcal{F}_{gg}^{\mathrm{measured}}$ is observed.

Figure 5.14 shows resulting shifts. In most of $gg$ fraction both ISR/FSR less and more systematic uncertainty is negative, we quote the half of the largest difference from default value in each input $gg$ fraction.

Systematics function due to ISR/FSR more and less is

$$\mathrm{SYST}_{\mathrm{ISRmore}} = -0.054 \times \mathcal{F}_{\mathrm{gg}}^2 - 0.067 \times \mathcal{F}_{\mathrm{gg}} + 0.049$$

$$\mathrm{SYST}_{\mathrm{ISRless}} = -0.004 \times \mathcal{F}_{\mathrm{gg}}^2 - 0.061 \times \mathcal{F}_{\mathrm{gg}} + 0.098$$

, respectively.

### 5.4.6 Parton Distribution Function

The CTEQ5L parton distribution function (PDF) is used in this analysis. To evaluate the systematics due to PDF uncertainties, we calculate variation in $\Delta\phi$ templates of $gg$ and $q\bar{q}$ when we choose different PDF sets, such as MRST72, MRST75, CTEQ6L, CTEQ6L1 and CTEQ6M. To calculate $\Delta\phi$ templates with different PDF sets, we adopt the weighted MC method. In this method, we reweigh each event of a MC sample we already have, instead of generating a different set of MC events with each different PDF set. We calculate the relative probability of the event on the assumption of a different PDF set, based on the parton momentum fractions $x_1$, $x_2$, and $Q^2$ in the event, and obtain new templates by re-weighting $\Delta\phi$ distributions.

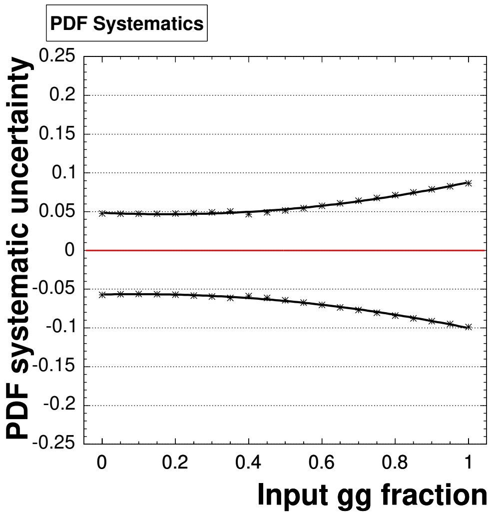


Figure 5.15: Residual plot of input $gg$ vs measured $gg$ fraction for systematic uncertainty of PDF.

We generate 10,000 sets of pseudo-data in each $\mathcal{F}_{gg}^{\text{true}}$, where $\Delta\phi$ templates of $gg$ and $q\bar{q}$ are changed to the templates obtained by the weighted MC method on the assumption of various PDF sets, respectively. Then, we perform the measurement of $\mathcal{F}_{gg}^{\text{measured}}$ on the assumption of the default $\Delta\phi$ templates, and look how much shift in $\mathcal{F}_{gg}^{\text{measured}}$ is observed.

Figure 5.15 shows resulting shift by PDF uncertainty. The sum in quadrature of the systematics from the uncertainties of MRST, $\alpha_s$, and 20 parameters is

$$\mathrm{SYST}_{\mathrm{PDFpositive}} = 0.061 \times \mathcal{F}_{\mathrm{gg}}^2 - 0.021 \times \mathcal{F}_{\mathrm{gg}} + 0.049$$

$$\mathrm{SYST}_{\mathrm{PDFnegative}} = -0.053 \times \mathcal{F}_{\mathrm{gg}}^2 + 0.010 \times \mathcal{F}_{\mathrm{gg}} - 0.057$$

### 5.4.7 Jet energy scale

In this analysis, we don't use jets except for $t\bar{t}$ event selection. The uncertainty in jet energy scale (JES) affect our measurement only through uncertainties in the $gg/q\bar{q}$ acceptance ratio, $\mathcal{R}$ and the expected number of background, $n_{\mathrm{b}}$.

JES uncertainty is already incorporated in the uncertainty in $n_{\mathrm{b}}$, and an effect to the acceptance ratio due to JES uncertainty is expected to be negligible. Therefore we suppose there is no systematic uncertainty due to JES uncertainty.

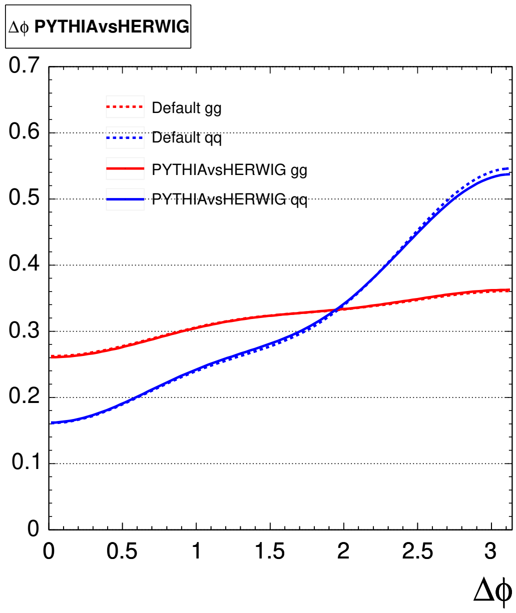


Figure 5.16: $\Delta\phi$ distributions of $f_i^{\text{more}}(\Delta\phi)$(left solid) and $f_i^{\text{less}}(\Delta\phi)$(right solid). with default HERWIG(dotted).

### 5.4.8 Other Systematics

We add the systematic uncertainty due to the Top $p_T$ difference between PYTHIA and HERWIG. Top quark $p_T$ difference make difference of leptons $\Delta\phi$. Figure 5.16 shows $\Delta\phi$ distribution that re-weighted by difference $p_T$ distribution between HERWIG and PYTHIA. We generate 10,000 sets of pseudo-data in each $\mathcal{F}_{gg}^{\text{true}}$, where $\Delta\phi$ templates of $gg$ and $q\bar{q}$ are changed to the templates obtained by the weighted MC method on the difference between PYTHIA and HERWIG, and look how much shift in $\mathcal{F}_{gg}^{\text{measured}}$ is observed.

Figure 5.17 shows resulting shifts. Systematics uncertainty due to the Top $p_T$ difference between HERWIG and PYTHIA is

$$\text{SYST}_{\text{Other}} = \pm 0.03$$

### 5.4.9 Summary of Uncertainty

Table 5.3 shows summary of systematic uncertainty, and Figure 5.18 shows Feldman-Cousins confidence belt with systematic uncertainty.

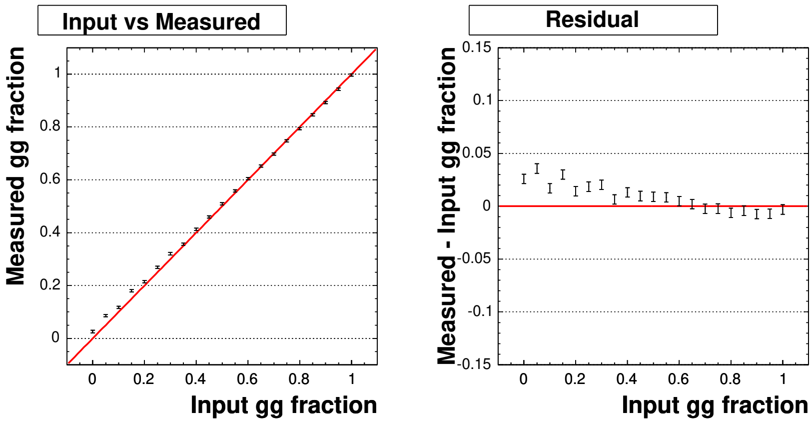


Figure 5.17: Linearity and residual plot of input $gg$ vs measured $gg$ fraction for systematic uncertainty of Top $p_T$ difference between HERWIG and PYTHIA.

Table 5.3: The summary table of systematic uncertainty.

| Source | Positive Uncertainty in $\mathcal{F}_{gg}^{\text{measured}}$ | Negative Uncertainty in $\mathcal{F}_{gg}^{\text{measured}}$ |
|---|---|---|
| Statistics | 0.448 | 0.448 |
| $\Delta\phi$ template and Expected number of bkg | 0.049 | 0.049 |
| $A_{gg}/A_{q\bar{q}}$ | 0.014 | 0.014 |
| Estimation method of Systematic | 0.020 | 0.020 |
| Other (top $p_T$ PYTHIA vs HERWIG) | 0.03 | 0.03 |
| | if Positive value | if Negative value |
| NLO matrix element | $0.032 \times \mathcal{F}_{gg}^2 + 0.080 \times \mathcal{F}_{gg} - 0.008$ | $0.032 \times \mathcal{F}_{gg}^2 + 0.080 \times \mathcal{F}_{gg} - 0.008$ |
| PDF | $0.068 \times \mathcal{F}_{gg}^2 - 0.009 \times \mathcal{F}_{gg} + 0.027$ | $-0.046 \times \mathcal{F}_{gg}^2 + 0.009 \times \mathcal{F}_{gg} - 0.040$ |
| | $\pm$ half of the largest | |
| ISRFSR more | $-0.054 \times \mathcal{F}_{gg}^2 - 0.067 \times \mathcal{F}_{gg} + 0.049$ | $-0.054 \times \mathcal{F}_{gg}^2 - 0.067 \times \mathcal{F}_{gg} + 0.049$ |
| ISRFSR less | $-0.004 \times \mathcal{F}_{gg}^2 - 0.061 \times \mathcal{F}_{gg} + 0.098$ | $-0.004 \times \mathcal{F}_{gg}^2 - 0.061 \times \mathcal{F}_{gg} + 0.098$ |

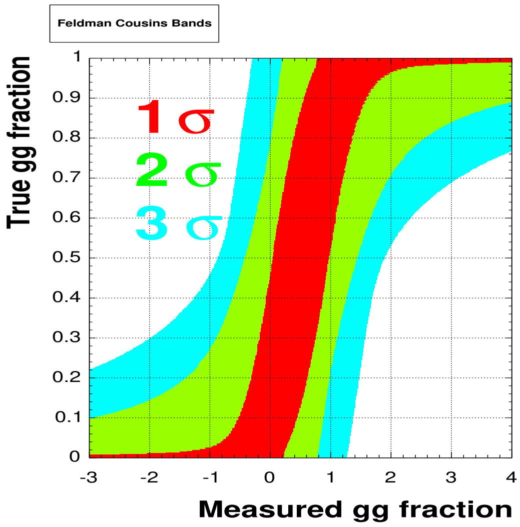


Figure 5.18: Confidence belt based on Feldman-Cousins' ordering principle including systematic uncertainties. The region surrounded by the broken curves corresponds $1\sigma$, $2\sigma$, $3\sigma$ intervals.

## 5.5 Result of gluon fusion fraction

Finally, we reveal $\Delta\phi$ distribution of the data sample after we fixed the analysis method and studies of systematic uncertainties.

Figure 5.20 indicates the distribution of $\Delta\phi$ in 2.0 fb$^{-1}$ data (left). The solid curve on the histogram means the best fit. The solid line on the confidence belt (right) indicates $\mathcal{F}_{gg}^{\text{measured}}$ and its cross section with the confidence belt corresponds to the confidence interval on $\mathcal{F}_{gg}^{\text{true}}$. From this, we retrieve the following results:

$$
\begin{aligned}
\mathcal{F}_{gg} &= 0.53 \ ^{+0.35}_{-0.37}\ (\text{stat.})\ ^{+0.07}_{-0.08}\ (\text{syst.}) \\
&= 0.53 \ ^{+0.36}_{-0.38} \qquad (5.4)
\end{aligned}
$$

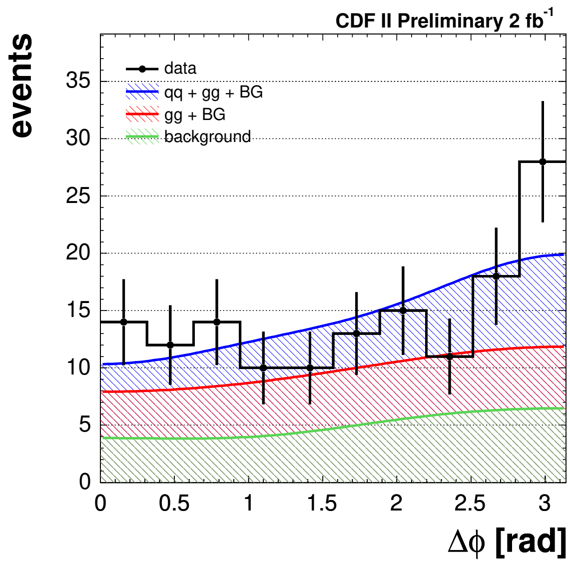


Figure 5.19: The distribution of $\Delta\phi$ in 2.0 fb$^{-1}$ data. The solid curve on the histogram means the best fit.

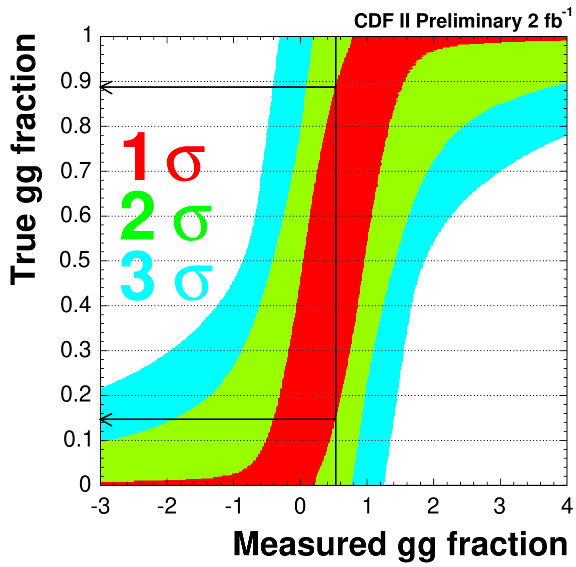


Figure 5.20: The solid line on the confidence belt indicates $\mathcal{F}_{gg}^{\rm measured}$ and its cross section with the confidence belt corresponds to the confidence interval on $\mathcal{F}_{gg}^{\rm true}$.

# Chapter 6

# Conclusion

We have measured the production cross section of top-antitop quark pairs and the relative fraction of the subprocess where the initial states are gluon fusion or $q\bar{q}$ annihilation in proton-antiproton collisions at a center-of-mass energy of 1.96 TeV. We observe 145 $t\bar{t}$ candidate events with an expected background of 49.5 events.

The results are

$$\sigma(p\bar{p} \to t\bar{t}X) = 6.8\ \pm 1.1\ \ (\pm 1.0\ (\mathrm{stat.}) \pm 0.6\ (\mathrm{syst.}))\ \ \mathrm{pb}$$

$$\mathcal{F}_{gg} \ \ = \ \ 0.53\ ^{+0.36}_{-0.38}\ \ (^{+0.35}_{-0.37}\ (\mathrm{stat.})\ ^{+0.07}_{-0.08}\ (\mathrm{syst.}))$$

The Standard Model expectations are $\sigma(p\bar{p} \to t\bar{t}X) = 6.7\ ^{+0.7}_{-0.9}$ pb and $\mathcal{F}_{gg} = 0.15\ \pm 0.05$.

The observed cross section is consistent with Standard Model prediction, and that is the best measurement at the time in dilepton channel. Comparison with other $\sigma(p\bar{p} \to t\bar{t}X)$ measurement is shown Figure 6.1.

The observed gluon fusion fraction is also consistent with Standard Model prediction. However currently we can not evaluate the phenomena not described by the Standard Model due to big statistical uncertainty. That is the first measurement of gluon fusion fraction using dilepton channel, and uncertainty is dominated by statistics. Thus there will be some improvement for this analysis still more.

Dilepton channel is called clean channel in the $t\bar{t}$ decay due to the characteristic signal events(two lepton, two jet and large missing $E_T$), but branching ratio is only 5 % in $t\bar{t}$ decay(Section 1.4). To keep good events statistics, this analysis didn't apply so tight cut. As a results, background fraction increase to about 35 %, that is almost same as lepton+jets channel. These residual background that passing the events selection are very difficult to describe by Monte Carlo, especially fake and Drell-Yan. But kinematic features of the signal and control region's data are qualitatively consistent with the expectations for signal and background due to the more advanced data driven background study (Section 4.6). These deep comprehension without the tight selection cut is important validation of our background modeling and also that will be good advantage for analysis using multivariate method such as Neural Network method. Because these method generate more efficient results using kinematic distribution. Therefore that will make more good signal significance for cross section measurement and that will make more good separation of gluon fusion and $q\bar{q}$ annihilation. Tevatron continue to take the data. Thus measure will be enhanced by these improvement.

As described above, the top quark property measurements will remain crucial to our understanding of the fundamental particles and their interactions, and discovering what, if anything, will supersede the Standard Model.

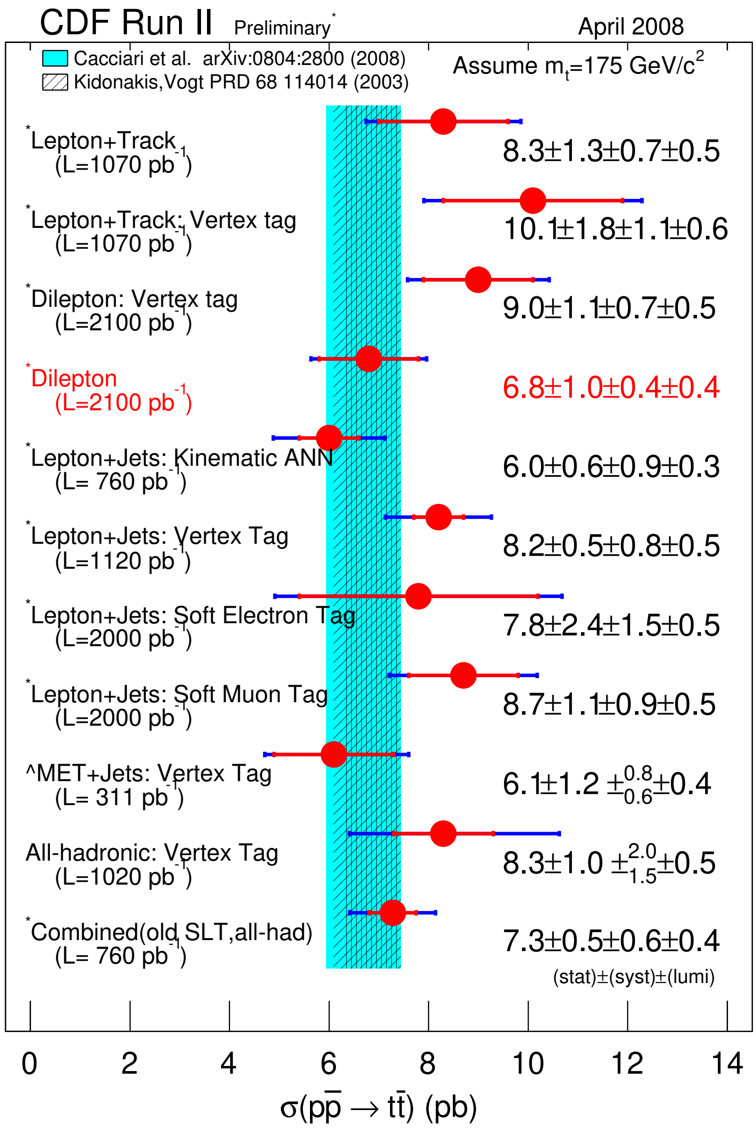


Figure 6.1: Comparison of $\sigma(p\bar{p} \to t\bar{t}X)$ with other analysis.

# Appendix A

# Spin state of the $t\bar{t}$ system

The top quark has spin 1/2, so there are two eigen-states of spin on any axis of quantization: $|+\rangle_a$, $|-\rangle_a$ , where $a$ denote the axis of quantization. If we define the proton direction as $z$-axis, the two spin eigen-states on $x$-axis $|+\rangle_x$, $|-\rangle_x$ can be respectively described using the spin eigen-states on $z$-axis $|+\rangle_z$, $|-\rangle_z$ as follows:

$$
\begin{aligned}
|+\rangle_x &= \frac{1}{\sqrt{2}}|+\rangle_z + \frac{1}{\sqrt{2}}|-\rangle_z \\
|-\rangle_x &= -\frac{1}{\sqrt{2}}|+\rangle_z + \frac{1}{\sqrt{2}}|-\rangle_z \ ,
\end{aligned}
$$

respectively. Using these relations, the spin states of $t\bar{t}$ pair at threshold production through $gg$-fusion and $q\bar{q}$ annihilation can be written as:

$$
\begin{aligned}
gg \ &: \ J = 0,\ J_z = 0 \\
&\quad |+\rangle_z |-\rangle_z - |-\rangle_z |+\rangle_z = |+\rangle_x |-\rangle_x - |-\rangle_x |+\rangle_x \\
q\bar{q} \ &: \ J = 1,\ J_z = 1 \\
&\quad |+\rangle_z |+\rangle_z = \frac{1}{2}\left(|+\rangle_x |-\rangle_x - |+\rangle_x |-\rangle_x - |-\rangle_x |+\rangle_x + |-\rangle_x |-\rangle_x\right) \\
q\bar{q} \ &: \ J = 1,\ J_z = -1 \\
&\quad |-\rangle_z |-\rangle_z = \frac{1}{2}\left(|+\rangle_x |-\rangle_x + |+\rangle_x |-\rangle_x + |-\rangle_x |+\rangle_x + |-\rangle_x |-\rangle_x\right)
\end{aligned}
$$

These indicate that if we choose an axis in the azimuthal plane perpendicular to the beam axis, as the axis of quantization, the spin states of the top quark and the anti-top quark are fully anti-correlated in the $gg$-fusion case, and have no correlation in the $q\bar{q}$ annihilation.

# Appendix B

# $V-A$ decay of the top quark

In $t \to W^+ b \to \ell^+ \nu b$ decay, the matrix element of the decay is proportional to

$$\left\{\bar{u}_b \gamma_\mu \left(1-\gamma^5\right) u_t\right\}\left\{\bar{u}_\nu \gamma^\mu \left(1-\gamma^5\right) v_{\ell^+}\right\}.$$

Using the Fierz transformation, the equation can be rewritten to be

$$2\left\{\bar{u}_b \left(1+\gamma^5\right) u_\nu^C\right\}\left\{\bar{v}_{\ell^+}^C \left(1-\gamma^5\right) u_t\right\},$$

where $C$ means charge conjugation, i.e. $\psi^C = C\bar{\psi}^T = i\gamma^2\psi^*$.

The spinors of $\ell^+$ and $t$ in the top rest frame can be written as follows:

$$\begin{aligned} v_{\ell^+} &= N_{\ell^+}\begin{pmatrix} \boldsymbol{\sigma}\cdot\hat{\boldsymbol{\ell}}\phi_{\bar{\ell}} \\ \phi_{\bar{\ell}} \end{pmatrix} \\ u_t &= N_t \begin{pmatrix} \phi_t \\ 0 \end{pmatrix}, \end{aligned}$$

where $\boldsymbol{\sigma}$ denotes the Pauli matrics, and $\hat{\boldsymbol{\ell}}$ is the unit vector parallel to the flight direction of the charged lepton in the top rest frame, and $\phi_{\bar{\ell}}$ and $\phi_t$ represent two component spinor of the charged lepton and the top quark, respectively. Then, we find

$$\bar{v}_{\ell^+}^C \left(1-\gamma^5\right) u_t = -iN_{\ell^+}N_t\phi_{\ell^+}^T\sigma_2\left(1+\boldsymbol{\sigma}\cdot\hat{\boldsymbol{\ell}}\right)\phi_t.$$

If we choose $\hat{\boldsymbol{\ell}}$ as the axis of quantization of the top quark,

$$1+\boldsymbol{\sigma}\cdot\hat{\boldsymbol{\ell}} = \begin{pmatrix} 2 & 0 \\ 0 & 0 \end{pmatrix}.$$

This means that we always observe the top quark to be in the spin state $\phi_t = \begin{pmatrix} 1 \\ 0 \end{pmatrix}$.

# Bibliography


[1] F. Abe *et al.*, "Observation of top quark production in $p\bar{p}$ collisions with the Collider Detector at Fermilab", Phys. Rev. Lett. **74**, 2626 (1995).

[2] S. Abachi *et al.*, "Observation of the top quark", Phys. Rev. Lett. **74**, 2632 (1995).

[3] DONUT, K. Kodama *et al*, Phys. Rev. Lett. 74, 2632 (1995).

[4] D. J. Gross and F. Wilczek, "Asymptotically free gauge theories", Phys. Rev. D **8**, 3633 (1973).

[5] H. D. Politzer, "Asymptotic freedom: An approach to strong interactions", Phys. Rept., **14**, 129 (1974).

[6] S. L. Glashow, "Partial symmetries of weak interactions", Nucl. Phys., **22**, 579 (1961).

[7] A. Salam and J. C. Ward, "Electromagnetic and weak interactions", Phys. Lett., **13**, 168 (1964).

[8] S. Weinberg, "A model of leptons", Phys. Rev. Lett., **19**, 1264 (1967).

[9] P. W. Higgs, "Broken symmetries and the masses of gauge bosons", Phys. Rev. Lett. **13**, 508 (1964).

[10] R. Barate *et al.*, "Search for the standard model Higgs boson at LEP", Phys. Lett. B **565**, 61 (2003).

[11] The LEP Collaboration, The LEP Electroweak Working Group, "Precision Electroweak Measurements and Constraints on the Standard Model", Tech. Report CERN-PH-EP/2007-039, CERN, 2007.

[12] E. Rice *et al.*, "Search for structure in $\sigma(e^+e^- \rightarrow hadrons)$ between $\sqrt{s} = 10.34$ and 11.6 GeV", Phys. Rev. Lett. **48**, 906 (1982).

[13] The CDF Collaboration, the DØ Collaboration, the Tevatron Electroweak Working Group, "Combination of CDF and Ø Results on the Top-Quark Mass", hep-ex/0404010.

[14] N. Kidonakis *et al.*, Phys. Rev. Lett. D **68**, 114014 (2003); M. Cacciari *et al.*, J. High Energy Phys. **0404** 068 (2004).

[15] T. Arens *et al.*, Phys. Lett. B **302**, 501-506 (1993).

[16] Y. Hara, Prog. Theor. Phys. **86**, 779 (1991).

[17] M. Cacciari *et al.*, "The $t\bar{t}$ cross-section at 1.8 and 1.96 TeV: A study of the systematics due to parton densities and scale dependence", J. High Energy Phys. **0404**, 068 (2004).

[18] The CDF Collaboration, "Combination of CDF top quark pair production cross section measurements with 2.8 fb$^{-1}$", CDF public note, 9448 (2008).

[19] M. Kobayashi and T. Masukawa, "CP violation in the renormalizable theory of weak interaction", Prog. Theor. Phys. **49**, 652 (1973).

[20] Joey Thompson, "Introduction to Colliding Beams at Fermilab", FERMILAB-TM-1909
The detailed information is available at the web pages.

[21] D. Patterson, "The FNAL 200-MeV Linac", FERMILAB-MISC-1986-01.

[22] E.L. Hubbard, "Booster Synchrotron", FERMILAB-TM-0405.

[23] S. D. Holmes, " Status of the Fermilab Main Injector and Recycler", FERMILAB-CONF-97-298.

[24] M. D. Church and J. P. Marriner, "The Antiproton Sources: Design and Operation", *Annu. Rev. Nucl. Part. Sci.*, **43**, 253 (1993).

[25] G. Jackson, "The Fermilab recycler ring technical design report. Rev. 1.2", FERMILAB-TM-1991.

[26] "Design report Tevatron 1 Project", FERMILAB-DESIGN-1982-01.

[27] C.W. Schmidt, "Review of Negative Hydrogen Ion Sources", FERMILAB-LU-166.

[28] Cockcroft, J.D. and Walton, E.T.S., "Experiments with High Velocity Positive Ions. II. The Disintegration of Elements by High Velocity Protons", Proc. R. Soc. London A **137**, 229 (1932).

[29] C. Hojvat *et al.*, "The Multiturn Charge Exchange Injection System for the Fermilab Booster Accelerator", *IEEE Transactions on Nuclear Science*, NS- **26**, 3149 (1979).

[30] L. W. Alvarez *et al.*, "Berkeley Proton Linear Accelerator", Rev. Sci. Instr. **26**, 111 (1955).

[31] D. M. Mohl, G. Petrucci, L. Thorndahl and S. van der Meer, "Physics and technique of stochastic cooling", Phys. Rep. **58**, 73 (1980).

[32] S. Nagaitsev *et al.*, " Experimental Demonstration of Relativistic Electron Cooling", Phys. Rev. Lett. **96**, 044801 (2006).

[33] F. Abe *et al.*, "The CDF II detector: Technical design report", Tech. Report FERMILAB-Pub-96/390-E (1996).

[34] J. Elias *et al.*, Nucl. Instrum. Methods, A **441**, 366 (200).

[35] G. Gruppen, Particle Detectors, Gambridge University Press, 196 (1996).

[36] R. Barnett *et al.*, Phys. Rev. D **54**, 1 (1996).

[37] C. S. Hill *et al.*, "L00: Operational experience and performance of the CDF II silicon detector", Nucl. Instrum. Methods, A **530**, 1 (2004).

[38] A. Sill *et al.*, "SVX-II: CDF Run II silicon tracking projects", Nucl. Instrum. Method, A **447**, 1 (2000).

[39] A. Affolder *et al.*, "ISL: Intermediate silicon layers detector for the CDF experiment", Nucl. Instrum. Method A **543**, 84 (2000).

[40] T. Zimmerman *et al.*, Nucl. Instrum. Methods, A **409**, 369 (1998).

[41] T. Affolder *et al.*, "COT central outer tracker", Nucl. Instrum. Methods, A **526**, 249 (2004).

[42] L. Balka *et al.*, "The CDF central electromagnetic calorimeter", Nucl. Instrum. Methods, A **267**, 272 (1988).

[43] S. Bertolucci *et al.*, "The CDF central and endwall hadronic calorimeters", Nucl. Instrum. Methods, A **267**, 301 (1988).

[44] M. Albrow *et al.*, "The CDF plug upgrade electromagnetic calorimeter: Test beam result", Nucl. Instrum. Methods, A **480**, 524 (2002).

[45] "Shower Maximum Detector for the CDF Plug Upgrade Calorimeter", Nucl. Instrum. Meth. A **412**, 515 (1998).

[46] G. Ascoli *et al.*, "The CDF central muon detector", Nucl. Instrum. Methods, A **268**, 33 (1988).

[47] A. Bhatti *et al.*, "Determination of the jet energy scale at the Collider Detector at Fermilab", NIM A **556**, 375 (2006).

[48] T. Sjostrand *et al.*, "High-Energy-Physics Event Generation with PYTHIA 6.1", Comput. Phys. Commun. **135**, 238 (2001).

[49] M.L. Mangano, M. Moretti, F. Piccinini, R. Pittau, A. Polosa, "ALPGEN, a generator for hard multiparton processes in hadronic collisions", JHEP **0307**, 001 (2003), hep-ph/0206293.

[50] U. Baur *et al.*, Phys. Rev.D **50**, 1917 (1994).

[51] M. Jezabek and J.H. Kühn, Phys. Lett. B **329**, 317 (1994).

[52] G. Corcella *et al.*, J. High Energy Phys. **0101**, 010 (2001).

[53] G. Feldman and R. Cousins, Phys. Rev D **57**, 3873-3889 (1998).

[54] W. Bernreuther *et al.*, Nucl. Phys. B **690**, 81-137 (2004).

[55] S. Frixione and B.R. Webber, J. High Energy Phys. **0206**, 029 (2002); S. Frixione *et al.*, J. High Energy Phys. **0308**, 007 (2003).